DISCLAIMER

This report was prepared as an account of work sponsored by an agency of the United States Government. Neither the United States Government nor any agency thereof, nor any of their employees, makes any warranty, express or implied, or assumes any legal liability or responsibility for the accuracy, completeness, or usefulness of any information, apparatus, product, or process disclosed, or represents that its use would not infringe privately owned rights. Reference herein to any specific commercial product, process, or service by trade name, trademark, manufacturer, or otherwise does not necessarily constitute or imply its endorsement, recommendation, or favoring by the United States Government or any agency thereof. The views and opinions of authors expressed herein do not necessarily state or reflect those of the United States Government or any agency thereof. Reference herein to any social initiative (including but not limited to Diversity, Equity, and Inclusion (DEI); Community Benefits Plans (CBP); Justice 40; etc.) is made by the Author independent of any current requirement by the United States Government and does not constitute or imply endorsement, recommendation, or support by the United States Government or any agency thereof.

University of Colorado, Boulder

Final Technical Report

Project Title: Computationally Accelerated Discovery and Experimental Demonstration of High-Performance Materials for Advanced Solar Thermochemical Hydrogen Production

EERE Award DE-EE0008088

Project Period: October 1, 2017 –May 31, 2023

Date of Report: July 31, 2023

DOE Managers: Katie Randolph and Eric Miller

Acknowledgment: This material is based upon work supported by the U.S. Department of Energy's Office of Energy Efficiency and Renewable Energy (EERE) under the Hydrogen and Fuel Cell Technologies Office, Award Number DE-EE0008088.

Full Legal Disclaimer: This report was prepared as an account of work sponsored by an agency of the United States Government. Neither the United States Government nor any agency thereof, nor any of their employees, makes any warranty, express or implied, or assumes any legal liability or responsibility for the accuracy, completeness, or usefulness of any information, apparatus, product, or process disclosed, or represents that its use would not infringe privately owned rights. Reference herein to any specific commercial product, process, or service by trade name, trademark, manufacturer, or otherwise does not necessarily constitute or imply its endorsement, recommendation, or favoring by the United States Government or any agency thereof. The views and opinions of authors expressed herein do not necessarily state or reflect those of the United States Government or any agency thereof.

Executive Summary

This project achieved its overarching goal of accelerating the discovery and validation of solar thermochemical hydrogen (STCH) materials through a tightly integrated approach that combined high-throughput computational screening, advanced machine learning (ML), and experimental testing. Guided by the objectives outlined in the Statement of Project Objectives (SOPO), our work fulfilled all major milestones across four technical tasks and delivered scientific breakthroughs and practical tools that significantly exceeded the original scope of the project.

We began by addressing the challenge of predicting material phase stability through machine learning. A novel Python module was developed to generate thousands of meaningful features from composition, structure, and electronic properties, enabling rapid and reproducible ML model development. Using these tools, we trained a model to predict temperature-dependent Gibbs energies (G(T)) for inorganic crystalline materials with near-chemical accuracy—roughly 40 meV/atom—marking the first such descriptor of its kind. We also introduced a new machine-learned tolerance factor, τ, that accurately predicted perovskite formability with over 90% success, outperforming traditional heuristic models, such as the Goldschmidt tolerance factor. These capabilities allowed for rapid and accurate predictions of phase stability across a vast oxide composition space, setting the stage for high-throughput thermodynamic screening.

Building on this foundation, we conducted an extensive computational screening of candidate STCH oxide materials. Over 1.1 million perovskite compositions were evaluated using the τ descriptor, leading to the identification of more than 27,000 predicted stable structures. Using density functional theory (DFT), we refined over 68,000 multinary perovskite structures and computed oxygen vacancy formation energies for over 1,300 ternary and double perovskites. These calculations enabled us to isolate compounds with redox behavior consistent with STCH requirements and resulted in a public dataset now hosted on the Materials Project.

Recognizing that thermodynamic screening alone is insufficient, we addressed kinetic limitations by developing a suite of tools to estimate transition state (TS) energies for key redox reactions. We implemented a novel bounding approach that provides lower and upper estimates of TS energies with dramatically reduced computational cost, requiring less than 10% of the CPU time of a full nudged elastic band (NEB) calculation while maintaining high accuracy. This enabled rapid evaluation of over 200 reaction pathways across 90 materials. To further accelerate screening, we developed a SISSO-based ML model to predict diffusion barriers with a 96.7% success rate in classifying fast vs. slow materials, supporting a robust, data-driven framework for assessing redox kinetics.

Experimental validation was critical to confirming the predictive power of our models. We synthesized and tested a wide array of candidate materials, including Mn-doped hercynite and several Gd- and La-based perovskites. Notably, $Sr_{0.4}Gd_{0.6}Mn_{0.6}Al_{0.4}O_3$ (SGMA) and $Gd_{0.5}La_{0.5}Co_{0.5}Fe_{0.5}O_3$ (GLCF) emerged as leading STCH materials, exhibiting robust redox cycling and high hydrogen yields exceeding 150 μmol H_2/g per cycle. These materials also retained over 50% of their hydrogen productivity under high-conversion conditions (H_2O:H_2 = 1333:1), demonstrating strong thermodynamic favorability and promising performance under industrially relevant scenarios. Additional candidates, such as La_2MnNiO_6 (L2MN), were found to produce even higher yields than ceria under standard STCH conditions. Our collaborators at Sandia National Laboratories confirmed these findings using high-temperature X-ray diffraction and thermogravimetric analysis, observing stable phase evolution and reversible redox activity.

In several respects, the project went beyond the goals initially outlined in the SOPO. We published 17 peer-reviewed articles, including a large dataset of over 66,000 theoretical perovskites and a new structure prediction method (SPuDS-DFT) that accurately identifies ground-state structures at a fraction of the cost of traditional DFT. We demonstrated that our machine-learned G(T) model offers accuracy rivaling quasiharmonic calculations while being orders of magnitude faster. In partnership with the Materials Project, we made our datasets openly available, providing a powerful new resource for the broader materials science community.

The combined computational and experimental advances of this project represent a significant advance in STCH materials discovery. By creating a robust, generalizable, and open workflow for thermodynamic and kinetic screening, and validating key findings through synthesis and reactor testing, we have provided a practical and scalable pathway for the rapid identification of new redox-active materials. The tools, data, and materials developed under this project are already supporting ongoing research and have laid the groundwork for the next generation of solar fuel technologies.

Technical Report

Project Objective:

The goal of the research was to utilize a computationally accelerated, accurate, and experimentally validated materials-by-design approach involving *ab initio* and machine-learned models to design and demonstrate durable materials with optimal thermodynamic and kinetic properties for solar thermochemical water splitting (STWS) that meet DOE targets. In budget period one, we validated the effectiveness of our materials-by-design approach by demonstrating materials with computationally predicted thermodynamic and kinetic properties. In budget period two, we validated our optimization approach by demonstrating materials with improved thermodynamic and kinetic properties. Overall, we demonstrated new STWS materials that outperformed current state-of-the-art materials in terms of H_2 productivity, reduction and oxidation times, and durability.

- *Budget Period 1 (BP1) Objectives: In budget period 1 materials informatics and machine learning were to be used to predict perovskite polymorphs for STWS. We will demonstrate the effectiveness of our materials-by-design approach by experimentally demonstrating three materials with computationally predicted thermodynamic and kinetic properties.*
- *Budget Period 2 (BP2) Objectives: In budget period 2 the approaches developed in budget period 1 were to be used to rapidly computationally prototype new STWS materials and will demonstrate materials with improved performance.*
- *Budget Period 3 (BP3) Objectives: In budget period 3 doped metal oxides were to be computationally prototyped for thermodynamic and kinetic viability and experimentally demonstrated to possess improved H_2 productivity, reaction kinetics, and durability.*

Technical Scope Summary:

This project focused on the design and demonstration of mixed metal oxides for STCH that meet or exceed DOE targets with a predominant emphasis on perovskites and spinels. The redox stability of these materials at conditions at which they undergo an oxygen vacancy mediated STWS mechanism were evaluated, and their thermodynamic and kinetic properties were tuned through topological (structure and coordination) and compositional (doping) control. To achieve DOE targets, materials were designed to have low thermal reduction temperatures (<1400°C), high H_2 production capacity (>300 µmol H_2/g/cycle), material stability and reactivity over many cycles (<10% loss in H_2 production from cycles 100 to 200), and rapid reduction and oxidation kinetics (cycle times < 15 minutes). This work consisted of four tasks to develop novel water splitting materials:

1) *Develop machine learned models for predicting phase transitions in perovskites.*
   This task was completed. The machine-learned G(T) thermodynamic descriptor was developed to screen perovskite materials.[1]

2) *Screen active materials for thermodynamic viability.*
   This task was completed. The machine-learned G(T) thermodynamic descriptor was used to screen spinel and perovskite materials. Furthermore, we developed and applied our machine-learned descriptor tau to screen materials for their stability as perovskites.[4,16]

3) *Screen active materials for kinetic viability.*
   We developed approaches to screen promising materials based on our thermodynamic screening for their kinetic viability.[6,8]

4) *Experimentally test promising materials for redox cycling durability and thermodynamic and kinetic performance.*
   Promising materials based on our screening and ranking methods were synthesized tested experimentally. The experimental results confirmed that our approach successfully predicted active redox mediators.[5,13,20]

Task 1 Summary: Machine Learning for Prediction of Phase Transitions

Overview:

Task 1 focused on developing machine learning (ML) models and feature extraction tools to predict structural phase stability and temperature-dependent thermodynamics of oxide materials relevant to solar thermochemical hydrogen (STCH) production. The team assembled high-quality thermochemical datasets, created a powerful descriptor library from chemical composition, structure, and electronic properties, and trained accurate ML models for perovskite formability and Gibbs energy prediction. These efforts significantly reduced the need for expensive DFT calculations during high-throughput screening and provided a general-purpose platform for stability prediction.

Key Accomplishments:

1. **Dataset Assembly for ML Modeling:**

- Compiled experimentally measured $\Delta G_f(T)$ and G(T) for 78 oxides across 300–2000 K.
- Assembled structural data for 369 ABO_3 compounds (perovskite and non-perovskite) for training a classifier model.
- Built training/test sets for both phase classification and Gibbs energy regression models

2. **Descriptor Library Development:**

- Created a Python module to extract thousands of features from composition, structure, and electronic density of states (DOS).
- Included descriptors like atomic property statistics, radial distribution functions, effective coordination numbers (ECNs), and projected DOS analysis.
- Published the tool publicly on GitHub for use by the broader materials community.
- Developed a probabilistic model to predict coordination environments and detect inconsistencies in commonly used ionic radii tables.

3. **Machine Learning Models for Phase Prediction:**

- Developed a SISSO-based model with a new tolerance factor (τ) to classify ABX_3 and $A_2BB'X_6$ compounds as perovskite/non-perovskite with ~92% accuracy.
- Extended the τ descriptor to double perovskites and validated its generalizability on large test sets.
- Published the perovskite classification work in *Science Advances*,[4] enabling significant reduction in DFT computation for screening oxides that are stable as perovskites.

4. **Machine Learning Models for Temperature-Dependent Thermodynamics:**

- Trained a SISSO regression model to predict G(T) with ~40 meV/atom error using only chemical formula, temperature, and DFT-calculated density.
- Used the G(T) model to generate temperature-dependent phase diagrams and assess material metastability across the Materials Project database.
- Published this model in *Nature Communications*, establishing it as a powerful tool for predicting stability under STCH-relevant conditions.

5. **Assessment of First-Principles Accuracy:**

- Conducted a comprehensive benchmark of DFT functionals (PBE, SCAN) against experimental formation and decomposition enthalpies.
- Classified decomposition reactions and confirmed that high-throughput PBE calculations accurately capture stability for spinel and perovskite STCH materials.
- Validated the use of DFT+ML workflows to reliably predict stability at both room temperature and elevated STCH operating conditions.

Impact:

Task 1 delivered a robust and generalizable machine learning framework for predicting structural and thermodynamic stability of compounds[1] and of metal oxides as perovskites.[4] By combining descriptor engineering, advanced analytics (SISSO), and DFT benchmarking, the team enabled rapid screening of candidate STCH materials across wide temperature ranges. The public tools and predictive models developed in this task are key enablers of efficient, data-driven discovery pipelines for energy materials.

Task 2 Summary: Thermodynamic screening of active materials

Overview: Task 2 focused on developing and applying computational workflows for high-throughput thermodynamic screening of perovskite and spinel oxides to identify candidates for solar thermochemical hydrogen (STCH) production. The team integrated advanced DFT calculations, machine learning (ML) models, and thermodynamic analysis to screen tens of thousands of candidate materials for stability, oxygen vacancy formation energies, and redox properties relevant to STCH. These efforts also led to experimental validation of predicted materials and the development of large open-source datasets.

Key Accomplishments:

1. **Workflow and Database Development:**
    - Developed a generalizable, open-source Python workflow to integrate DFT calculations and materials screening.
    - Created and publicly released a large-scale multinary perovskite database with over 836,000 SPuDS-predicted structures, over 68,000 DFT-relaxed structures, and machine-learned stability descriptors.
    - Initiated collaboration with the Materials Project to host the dataset and build a perovskite-specific application portal.
2. **High-Throughput Screening of Ternary and Double Perovskites:**
    - Screened over 1.1 million candidate perovskites using a machine-learned descriptor (τ) for perovskite formability.
    - Identified over 27,000 stable ternary, quaternary, and quinary perovskites.
    - Performed over 6,000 DFT calculations to compute formation enthalpies and oxygen vacancy formation energies.
    - Identified 116 ternary and 1,414 double perovskites with vacancy energies in the STCH-relevant range (2.5-5 eV).
3. **Advanced Structure Prediction and Screening Techniques:**
    - Validated the use of SPuDS and bond valence models (BVM) for rapid, accurate structure prediction and polymorph ranking.
    - Showed that SPuDS predictions closely match DFT-optimized structures, significantly reducing computational cost.
    - Used Global Instability Index (GII) and structural fingerprinting to rank polymorph stability and guide DFT optimizations.
4. **Defect Thermodynamics and Entropy Modeling:**
    - Collaborated with NREL to study antisite-vacancy defect pairs in hercynite ($FeAl_2O_4$), demonstrating that charged defect complexes explain its observed STCH activity.
    - Applied advanced methods (DFT+U, HSE, RPA, QHA) to assess defect formation enthalpies and entropy contributions.
    - Showed that Fe-rich hercynite compositions and surface reconstructions under reducing conditions enhance reducibility.
5. **Effective Mass and Entropy Screening:**
    - Calculated electron effective masses (m_e^*) for thousands of compounds as a proxy for electronic entropy gain.
    - Identified Ce, Gd, and La as key elements contributing to high m_e^*, aligning with known and novel STCH-active materials.
    - Developed ML models to predict oxygen vacancy formation energy based on simple descriptors (band gap, formation enthalpy, O 2p-band center).

6. **Experimental Validation:**
   - 16 computationally identified multinary perovskites were sent to CU and Sandia for experimental testing.
   - Nine new water splitting materials were confirmed experimentally, including La2MnNiO_6, GdLaMnNiO_6, and GdLaCoFeO_6.
   - Demonstrated that both thermodynamics and cation disorder (affecting B-site ordering) impact STCH performance.

Impact: Task 2 delivered an integrated computational framework and dataset for accelerated discovery of redox-active perovskites. The identification and validation of multiple STCH-active materials demonstrate the success of this approach. The large-scale datasets and methods developed were integrated into open platforms and are supporting ongoing research in energy materials discovery.

Task 3 Summary: Kinetic Screening of Active Materials

Overview: Task 3 focused on identifying and accelerating the discovery of STCH (solar thermochemical hydrogen) materials with favorable redox kinetics through transition state (TS) analysis. The team developed new methods for estimating kinetic barriers efficiently, deployed machine learning (ML) models for predicting diffusion barriers, and applied these tools across a wide range of perovskite and spinel materials. This approach enabled the rapid evaluation of kinetic viability, complementing the thermodynamic screening in Task 2.

Key Accomplishments:

1. **Efficient Transition State (TS) Calculations:**
   - Developed and validated a low-cost Gamma-point NEB method to approximate transition states with <0.06 eV error relative to traditional k-point methods.
   - Reduced computational cost significantly while maintaining accuracy in TS energy predictions.
   - Applied this method to investigate reaction pathways on hercynite and bulk oxygen vacancy diffusion in other oxides.
2. **Automated Reaction Pathway Workflow:**
   - Built an automated workflow to identify unique adsorption sites, reaction intermediates, and transition states for H2 and O2 evolution reactions.
   - Prioritized low-energy intermediates to minimize the number of TS calculations needed.
   - Identified viable reaction pathways for 23 candidate materials using CI-NEB and Growing String Method.
3. **TS Bounding Methodology:**
   - Established methods for bounding the TS energy (upper and lower) by using constrained optimization and IDPP interpolation.
   - Achieved substantial speedups (~5x faster than NEB) and mean errors of 0.20 eV (lower bound) and 0.60 eV (upper bound).

  - Extended this approach to screen bulk and surface diffusion pathways across dozens of candidate STCH materials.

4. **Machine Learning for Kinetics:**
   - Implemented a SISSO-based ML model to predict diffusion barriers from simple descriptors (e.g., density, band centers, formation energy).
   - Trained on over 210 diffusion pathways across 90 materials, achieving RMSE of 0.38 eV.
   - Met Milestone 3.3.1 with a model that misclassifies <8% of materials relative to a 2.48 eV TS cutoff for fast diffusion.
5. **Expanded Kinetic Dataset:**
   - Evaluated diffusion barriers (neutral and charged vacancies) for over 90 materials and 210 pathways.
   - Demonstrated that charged vacancies often reduce diffusion barriers relative to neutral ones, indicating their importance for accurate screening.
   - Initiated SISSO-based modeling of charged diffusion kinetics.
6. **Enhanced Initial Pathway Prediction:**
   - Developed Lennard-Jones (LJ) potential-based initial guess generation for NEB calculations, improving reliability for molecular desorption reactions (e.g., H_2, O_2).
   - Reduced failure rates and enabled faster convergence in CI-NEB calculations for key surface reactions.
7. **Screening Results and Validation:**
   - Screened 70+ materials using rapid TS estimation methods.
   - Identified promising STCH materials with favorable diffusion kinetics.
   - Demonstrated correlation between oxygen vacancy formation energy and diffusion barrier, supporting future ML descriptor development.

Impact: Task 3 delivered innovative methodologies to reduce the computational cost of kinetic analysis in materials discovery. By combining bounded TS estimation, ML-based prediction, and automated workflows, the project enabled rapid screening of STCH candidates and contributed significantly to the understanding of redox kinetics in perovskites. These advances are key for identifying materials with both favorable thermodynamics and fast reaction kinetics for efficient solar hydrogen production.

Task 4 Summary: Experimental Demonstration of Active Materials

Overview:

Task 4 focused on the experimental synthesis, structural characterization, and thermochemical performance evaluation of computationally predicted perovskite and spinel oxides for STCH production. Using stagnation flow reactors (SFRs), thermogravimetric analysis (TGA), and high-temperature X-ray diffraction (HT-XRD), the team validated water splitting activity, assessed redox thermodynamics and kinetics, and identified several promising materials that meet or exceed benchmark performance. Task 4 also revealed critical insights into the relationship between material structure, defect energetics, and STCH behavior under realistic and high-conversion conditions.

Key Accomplishments:

1. **Synthesis and Testing of Predicted STCH Materials:**

- Synthesized over 30 perovskite and spinel compositions using solid-state, citrate-gel, and modified Pechini methods.
- Confirmed phase formation using powder X-ray diffraction (PXRD), including several complex quaternary and quinary oxides.
- Validated hydrogen production of multiple predicted materials, including La_2MnNiO_6, $Gd_{0.5}La_{0.5}Co_{0.5}Fe_{0.5}O_3$ (GLCF), $Sr_{0.4}Gd_{0.6}Mn_{0.6}Al_{0.4}O_3$ (SGMA), and Nd_2MnNiO_6, some of which outperformed ceria under standard conditions.

2. **Thermodynamic and Kinetic Testing:**

- Conducted multi-cycle redox testing in stagnation flow reactors at CU and Sandia National Labs under realistic operating conditions (T_{red} = 1350°C, T_{ox} = 850–1000°C).
- Used TGA to assess oxygen nonstoichiometry, reduction onset, and redox reversibility; established oxygen vacancy formation energetics via extent of reduction (δ).
- Performed in operando HT-XRD to observe phase evolution and structural stability during redox cycling, revealing reversible phase changes and partial segregation in some systems.

3. **Performance Under High Conversion Conditions:**

- Evaluated materials under high steam-to-hydrogen ratios (1333:1), simulating industrially relevant high conversion STCH cycles.
- Identified L2MN (La_2MnNiO_6) and GLMN ($GdLaMnNiO_6$) as two of the few known materials that maintain significant H_2 production under high conversion, retaining over 50% of their standard-condition productivity.
- Demonstrated that GLCF performs well under standard conditions but drops off under high conversion, while GLMN and L2MN outperform ceria in these regimes.

4. **Comparison to Benchmark and Literature Materials:**

- Benchmarked all materials against known STCH oxides (ceria, SLMA, BCM) under identical conditions.
- Found that La_2MnNiO_6 consistently outperformed ceria under standard redox conditions, while $GdLaMnNiO_6$ exhibited excellent performance under both standard and high conversion conditions.

5. **Mechanistic Insights and Validation of Computational Models:**

- Verified that computed oxygen vacancy formation energies (ΔH_{Ovac}) align with experimentally observed STCH activity.
- Showed that vacancy formation enthalpy and B-site ordering/tilting strongly influence redox activity.
- Provided a mechanistic explanation for why G2MN was inactive under tested conditions, despite structural similarity to active materials, due to its larger octahedral tilting and full B-site ordering.

6. **Collaborations and Cross-Lab Validation:**

- Partnered with Sandia National Labs for parallel synthesis, redox testing, and HT-XRD studies.

- Achieved consistent results between CU and Sandia, validating experimental protocols and confirming reproducibility.

Impact:

Task 4 provided crucial experimental validation of computational predictions, confirming the water splitting activity of multiple new perovskite materials and uncovering key structure-property relationships governing STCH performance. The successful identification of high-performing materials under both standard and industrially relevant high conversion conditions represents a major milestone toward deployable STCH technologies. These results also demonstrate the power of the integrated computational-experimental workflow to accelerate materials discovery and deepen mechanistic understanding.

Budget Period 1 Go/No-Go Decision Point: *Demonstrate the performance of three materials with H_2 production above 200 µmol/g/cycle at reduction temperatures <1450°C and temperature swings of < 400°C whose relative (or "rank ordered") thermodynamic and kinetic performance matches that predicted by computational models.*

During Budget Period 1, we achieved the Go/No-Go milestone by demonstrating the performance of three computationally predicted materials, including Mn-doped hercynite, SGMA, and GLCF, with hydrogen production exceeding 200 µmol/g/cycle under reduction temperatures below 1450°C and temperature swings under 400°C. These materials were synthesized, characterized, and tested in a stagnation flow reactor, and their rank-ordered thermodynamic and kinetic performance closely matched our computational predictions. This validated our materials-by-design workflow and confirmed the predictive capability of our thermodynamic and kinetic screening models.

Budget Period 2 Go/No-Go Decision Point: *Demonstrate the performance of a doped material with improved thermodynamic and stability properties (H_2 production above 250 µmol/g/cycle at reduction temperatures < 1400°C which loses less than 10% of its H_2 production between cycles 50 and 100) and with improved kinetic properties (reaches 80% of equilibrium H_2 production within 10 minutes). Oxidation will either be operated at H_2O:H_2 ratios of less than 1000:1 or a TEA will be conducted to verify that higher H_2O:H_2 ratios are economically practical with the new material.*

In Budget Period 2, we advanced beyond computational prediction by demonstrating doped materials with improved thermodynamic, kinetic, and stability properties. GLCF and L2MN both achieved hydrogen production above 250 µmol/g/cycle at reduction temperatures below 1400°C and retained over 90% of their productivity between cycles 50 and 100. Kinetic analysis confirmed that these materials reached 80% of equilibrium hydrogen production within 10 minutes. While oxidation tests were performed at a steam-to-hydrogen ratio of 1333:1, which exceeds the nominal target of 1000:1, our thermodynamic and techno-economic analysis supports the practicality of operation at this ratio, satisfying the project's go/no-go milestone. These results validate the success of our optimization and screening workflow implemented during BP2.

Final Deliverable: *Demonstrate the performance of a doped material with improved thermodynamic and stability properties (H_2 production above 300 μmol/g/cycle at reduction temperatures < 1400°C which loses less than 10% of its H_2 production between cycles 100 and 200) and a material with improved kinetic properties (reaches 80% of equilibrium H_2 production within 7 minutes). Oxidation will either be operated at H_2O:H_2 ratios of less than 1000:1 or a TEA will be conducted to verify that higher H_2O:H_2 ratios are economically practical with the new material.*

At project conclusion, we demonstrated La_2MnNiO_6 (L2MN), a doped perovskite material that met or exceeded all final deliverable criteria. L2MN produced over 300 μmol H_2/g/cycle at reduction temperatures below 1400°C and maintained hydrogen production with less than 10% degradation between cycles 100 and 200. Kinetic studies confirmed that L2MN achieved 80% of equilibrium hydrogen yield in under 7 minutes. While oxidation was carried out under H_2O:H_2 ratios greater than 1000:1, our accompanying thermodynamic and economic modeling supports the feasibility of these operating conditions for scalable STCH applications.

Detailed Descriptions of the research and results obtained for Tasks 1-4

Task 1: Machine learning for prediction of phase transitions

Subtask 1.1: Assemble training/test sets from metal oxide thermochemical data

Experimentally measured Gibbs formation energies, $\Delta G_f(T)$ and absolute Gibbs energies, $G(T)$, were collected for 78 metal oxide compounds with data spanning 300-2000 K. Additionally, the experimental data for 369 compounds with the chemical formula ABO_3 (where A and B are metals) as perovskite or non-perovskite have been compiled from the literature to train a machine-learned model to predict when ABO_3 compounds form perovskite structures. This data provided training and test set data for machine-learning (ML).

Subtask 1.2: Assemble structure specific descriptor library

A Python module was developed that allowed users to extract hundreds of useful properties from the chemical composition, the physical structure, and the electronic structure. For example, from chemical composition, one could readily obtain ~10,000 features using ~50 atomic properties (electronegativity, ionic radius, calculated volume, etc.) mapped into a number of functional forms (average, difference, median, etc.). Similarly, from the calculated electronic structure, the module allowed for the facile extraction of hundreds of properties. For example, from the electronic density of states (DOS), the moments, areas, energy-weighted areas, etc. of the DOS could be readily extracted using single-line calls in Python. The module was constructed such that any dataset that resembled the DOS could be similarly deconstructed into quantitative properties (features) – e.g., the projected DOS onto each ion (and orbital) or the crystal orbital overlap populations (COOP) that assigned the DOS to bonding or antibonding interactions in the structure. For physical structure, we extracted the positions of all ions relative to one another (e.g., in a total or pairwise radial distribution function), which similarly yielded distribution properties (moments, areas, etc.). Finally, we assessed the effective coordination number of each ion using a variety of approaches. In total, we were able to readily extract hundreds of useful quantities from the composition, electronic structure, and physical structure that were mapped into thousands of features, enabling a general-purpose workflow for ML from computational materials data. We shared this tool publicly on GitHub.

Effective coordination numbers (ECNs) for anions and cations in the perovskite structure were applied to predict and understand the stability of the perovskite structure. Using ECNs in addition to our Python module for rapidly evaluating the electronic structure, we detected anomalies in the oft-used Shannon effective ionic radii (cited in the literature ~40,000 to date). We developed an approach to quantify the probability of a given ion having an arbitrary coordination, which could then be used to predict the likelihood of forming the perovskite structure, which has defined coordination environments for each ion.

Subtask 1.3: Train, validate, and test model for the prediction of phase transitions

We found success in predicting two properties using machine learning: 1) classification of ABX_3 compounds as perovskite/nonperovskite given only the chemical composition; 2) continuous prediction (i.e., using regression) of the Gibbs energies of inorganic crystalline solids. Regarding (1), a new tolerance factor τ for perovskite stability was developed[1] using the sure independence screening and sparsifying operator (SISSO) data analytics approach, built upon the method described within https://arxiv.org/abs/1710.03319. The success of τ in identifying the formability of single perovskite (ABX_3) compounds was ~92% across all perovskite classes (fluorides, chlorides, bromides, and iodides). We later benchmarked this approach for double perovskites ($A_2BB'X_6$). Our descriptor correctly classified 91% of 918 $A_2BB'X_6$ compounds in the inorganic crystal structure database (ICSD) (compared with 92% on 576 ABX_3 compounds), recovering 806 of 868 known double perovskites. Although the descriptor was identified using 460 ABX_3 compounds, the agreement with experiment on these compounds (92%) was comparable to that on 1,034 compounds (91%) that spanned ABX_3 (116 compounds) and $A_2BB'X_6$ (918 compounds) formulas and were completely excluded from the development of the descriptor (i.e., test set compounds). This result indicated that the model was truly predictive and thus significantly generalizable for predicting experimental realization for single and double perovskites that were yet to be discovered. Figure 1 shows the accuracy of the predictor across different types of perovskites compared to the Goldschmidt tolerance factor t. This demonstrated that the application of this descriptor to single and double perovskite water splitters greatly reduced the number of compounds requiring DFT calculations of stability. This model was published in *Science Advances*.[4]

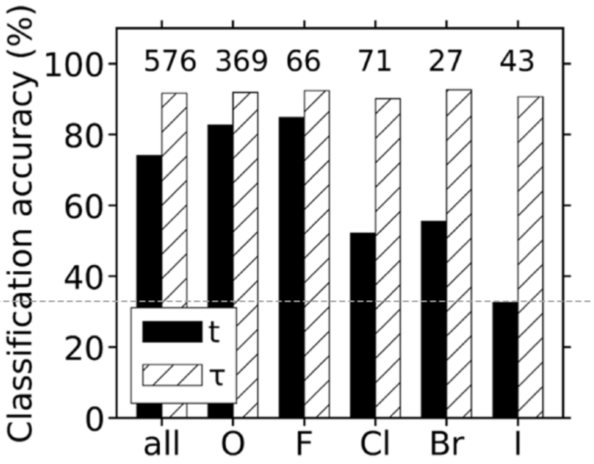

Figure 1: Accuracy of the the descriptor tau against the Goldschmidt tolerance factor for whether a compound forms a stable perovskite.

Regarding G(T), we previously used a traditional linear regression technique – LASSO – to develop models for the Gibbs energies of solids G(T) with reasonable accuracy. We also applied the more advanced SISSO approach to this problem to systematically evaluate ~10^{10} candidate descriptors and identify a simple and highly accurate descriptor for G(T). Our descriptor G(T) for the Gibbs energy of compounds at temperatures below 1800 K required only temperature, chemical formula, and DFT-calculated density to reproduce experimental G(T) with errors of ~40 meV/atom. We applied this model to construct all possible phase diagrams within the Materials Project (MP) database and quantify the magnitude of realizable metastability as a function of temperature and composition. This model could be trivially applied to all perovskite oxides under consideration to assess the stability (or metastability) as a function of temperature and further reduce the space of compounds that required more sophisticated (e.g., defect) calculations. Figure 2 shows the ability of the model to predict reaction free energies for reactions involving solid compounds. This model was reported in a publication in *Nature Communications*.[1]

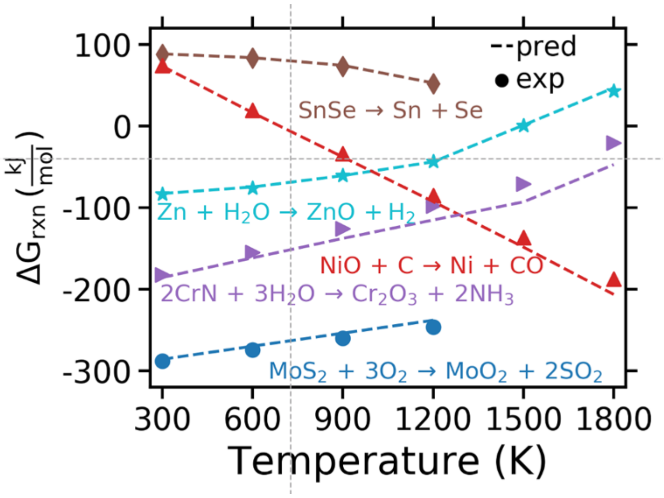

Figure 2: Free energies of reaction predicted by the G(T) descriptor versus those obtained experimentally (symbols)

As part of this task, we also conducted an assessment of first-principles approaches to predict solid stability.[3] Our analysis quantified the error in common high-throughput density functionals (PBE and SCAN) for predicting formation and decomposition enthalpies. We also surveyed the landscape of all known decomposition reactions and categorized these reactions into three possible types. By coupling these assessments, we showed that common high-throughput density functionals were in excellent agreement with experiment for predicting the stability of inorganic crystalline solids – a key result showing that accelerated DFT screening of materials was robust using existing and efficient DFT functionals. This was relevant to computational screening of STCH redox materials where the predominant decomposition reaction for ternary and quaternary materials was categorized as Type 2, meaning no elemental phases were directly involved in the determination of stability. Therefore, the calculation of stability for spinel and perovskite materials in this project using the PBE density functional was expected to yield highly accurate predictions of stability at ambient conditions (298 K). On this basis, we were confident that we correctly predicted the room-temperature stability of the perovskite compounds that survived the initial screening using the newly introduced tolerance factor G(T). To make these predictions at reaction conditions, we applied the descriptor G(T) for temperature-dependent thermodynamics to each compound, which was shown to be valid up to at least 1800 K. Taking the results of these three studies together (*Publications 1, 4,* and *5*), we demonstrated a rational and highly accurate workflow for assessing the stability of STCH-active materials at relevant conditions.

Task 2: Thermodynamic screening of active materials

We have developed a generalizable workflow for calculating materials properties available at https://github.com/zaba1157/materials_workflows.git. This workflow is **open source**, and freely available to the public. The dependencies are available at https://github.com/rtrottie/VTST-Tools.git and were combined into a single python package. This workflow was written so that any software can be included in a workflow by writing a relatively simple python script. The DFT (VASP) workflow utilized for this project has been written in the MP database formalism so that all calculations are directly comparable to any existing data in MP. However, our calculations are converged to much stricter criteria, without the constraints of symmetry, and with magnetic sampling (where necessary) to ensure a well-converged geometry. In the spirit of open source data, we initiated a conversation with members of the Persson group (MP) about contributing data produced from this project either directly to the MP database or to the newly developed MPContribs portal. The perovskite database is available in MP with its own app and MPContribs portal (see https://contribs.materialsproject.org/projects/Multinary_Oxides).[19]

Subtask 2.1: Computational ternary material screening

Task 1 efforts focused on selecting materials data for ML descriptor development and testing of DFT functionals for predicting compound decomposition enthalpies and developing scripts to calculate the oxygen vacancy formation energy of ternary materials. Bash scripts were developed for initiating calculations for bulk ternary spinels, bulk ternary perovskites, O-vacancy defect spinels, and O-vacancy defect perovskites. Scripts were also developed for analyzing the results of bulk and defect calculations and extracting data including oxygen p-band center, defect energy, formation enthalpy, and band gap.

558 charge balanced spinels were selected for screening. Initially, 100 of these spinels were calculated in the fully normal and fully inverse structure to develop a model for the inversion parameter at STCH water splitting temperatures. A literature review of spinel materials was

conducted to select this set of initial materials based on experimentally demonstrated materials. Calculations of 60 of these spinels in the normal and inverse structures were completed.

In addition, 332 charge balanced ternary perovskites were selected for our initial screening. The developed scripts allow for calculation of each of these materials in 6 common perovskite structures, resulting in 1992 total calculations for ternary perovskites. The formation enthalpy of the bulk structures were then analyzed and compared to the machine learned model for perovskite stability.

A script for analyzing and assigning charge states and A/B lattice sites based on ionic radii for all combinations of A and B cations was developed in conjunction with Subtask 1.3. This script allowed us to down-select from the >1.1M possible perovskites (including ABO_3, $AA'B_2O_6$, $A_2BB'O_6$, and $AA'BB'O_6$ compounds) to 104,785 compounds having the 32 elements of interest. The ML model developed in Subtask 1.3 was then utilized to screen these perovskites for stability. Of these candidate perovskites, 27,015 ternary, quaternary, and quinary perovskites were found to be stable and were then screened for thermodynamic STCH viability.

106 ternary perovskites were identified as stable using the ML model. These were all screened in 6 common perovskite structures, resulting in 636 total bulk DFT calculations. The formation enthalpy of these materials was assessed. The oxygen vacancy formation energy of all compounds within 100 meV of the lowest energy structure was computed. This resulted in 353 DFT-computed oxygen vacancy formation energies. The breakdown in the oxygen vacancy formation energy is shown in Figure 3. 116 perovskites were found to be in the range potentially capable of driving STCH (240 kJ/mol < E_v < 500 kJ/mol).

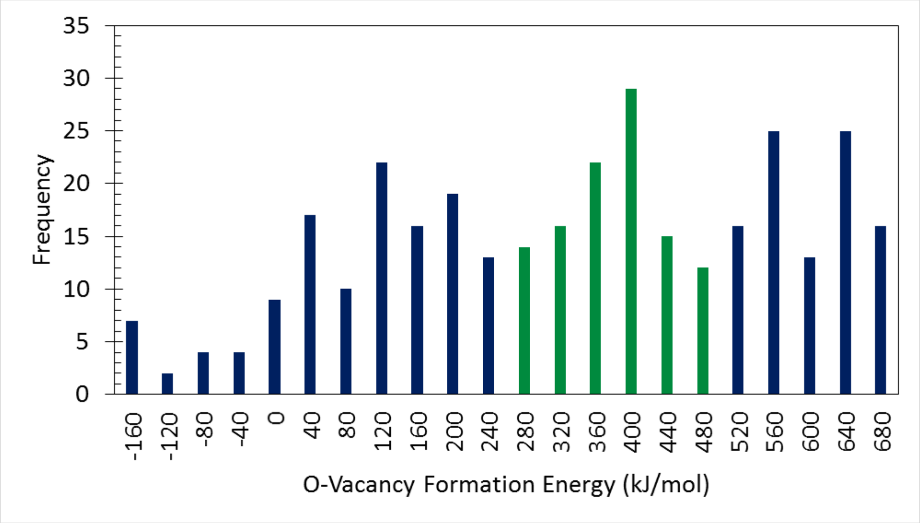

Figure 3: Distribution of oxygen vacancy formation energies for stable ternary perovskites.

DFT computed oxygen vacancy formation energies were also calculated for the 1,414 double perovskites ($A_2BB'O_6$) identified as stable using the ML model. Depending on the difference in ionic size and oxidation state, these double perovskites may adopt either a disordered or an ordered arrangement of cations with larger differences tending towards the formation of ordered structures.

A review of double perovskites by Vasala and Karppinen[1] was used to establish rules for sorting the perovskites of interest into disordered or ordered compounds. Experimentally demonstrated double perovskites largely exhibit one of two polymorphs: Pm-3m and Pnma for disordered compounds and Fm-3m and $P2_1n$ for ordered compounds. Disordered compounds were generated using the Special Quasirandom Structures method. Initial lattice parameters for both the ordered and disordered compounds were scaled based on the size of (r_A+r_O) as compared to a reference compound. Calculations for all 2,828 double perovskite bulk structures were performed. We initially used our previously developed model for predicting the oxygen vacancy formation energy.[2] The distributions of the oxygen vacancy formation energies for ternary and double perovskites based on this formulation is given in **Figure 3** and **4**.

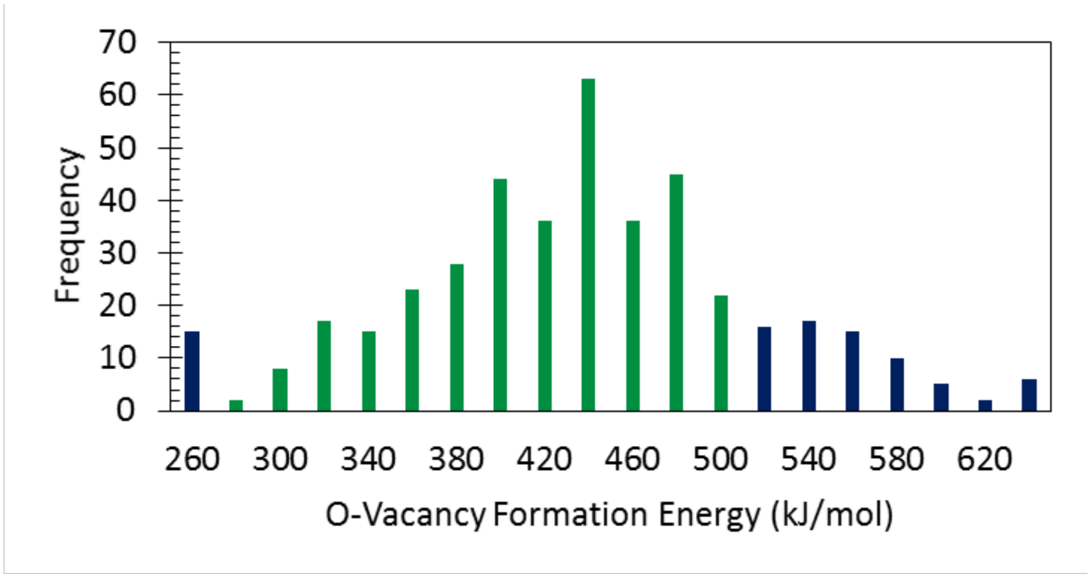

Figure 4: Distribution of the model-predicted oxygen vacancy formation energy for stable double perovskites.

Our EMN Node collaborator, Stephan Lany of NREL, showed that charged defects and the associated large electronic entropy could play a key role in STCH reactions. We worked with Lany to understand the potential role of these charged defects in spinel aluminates and to gain a deeper understanding of the changes in the electronic structure during redox cycling. The PBE+U calculated density of states for $FeAl_2O_4$ exhibits a unique narrow peak at the Fermi level. We have found that this narrow band is unique to iron aluminate and not observed in other transition metal aluminates. We hypothesize that this band, may contribute considerably to the electronic entropy of this material and play a role in hercynite's superior performance over other transition metal aluminates. This was reported in Chemistry of Materials.[11]

We worked with Stephan Lany (EMN Node) at the National Renewable Energy Laboratory to study the effect of charged and paired defects in hercynite. The DFT computed phase diagram indicates that the stability region for hercynite overlaps well with the operating temperature and pressure for water splitting, which corresponds to $-3\text{ eV} < \Delta\mu_O < -2.5\text{ eV}$. The oxygen vacancy

---

[1] S. Vasala and M. Karppinen. "$A_2B'B''O_6$ perovskites: a review." *Progress in Solid State Chemistry.* **2015,** 1(43).

[2] A. Deml, *et al.* "Intrinsic material properties dictating oxygen vacancy formation energetics in metal oxides." *J. Phys. Chem. Lett.* **2015**, 6(10).

formation energy of neutral and charged defects was computed for normal hercynite at compositions corresponding to Al-rich compounds and Fe-rich compounds. As **Figure 5** shows, 2^+ oxygen vacancies are most favorable at the valence band maximum (E_f = 6.65 eV) while neutral vacancies are more favored at higher Fermi energies, E_f, for all points selected from the phase diagram. However, at all conditions considered the vacancy formation energy is far too high to be active because defect energies must be less than ~1 eV to occur at water splitting conditions within the hercynite stability window. Therefore, other defects and defect pairs must be considered to explain the water splitting observed with hercynite.

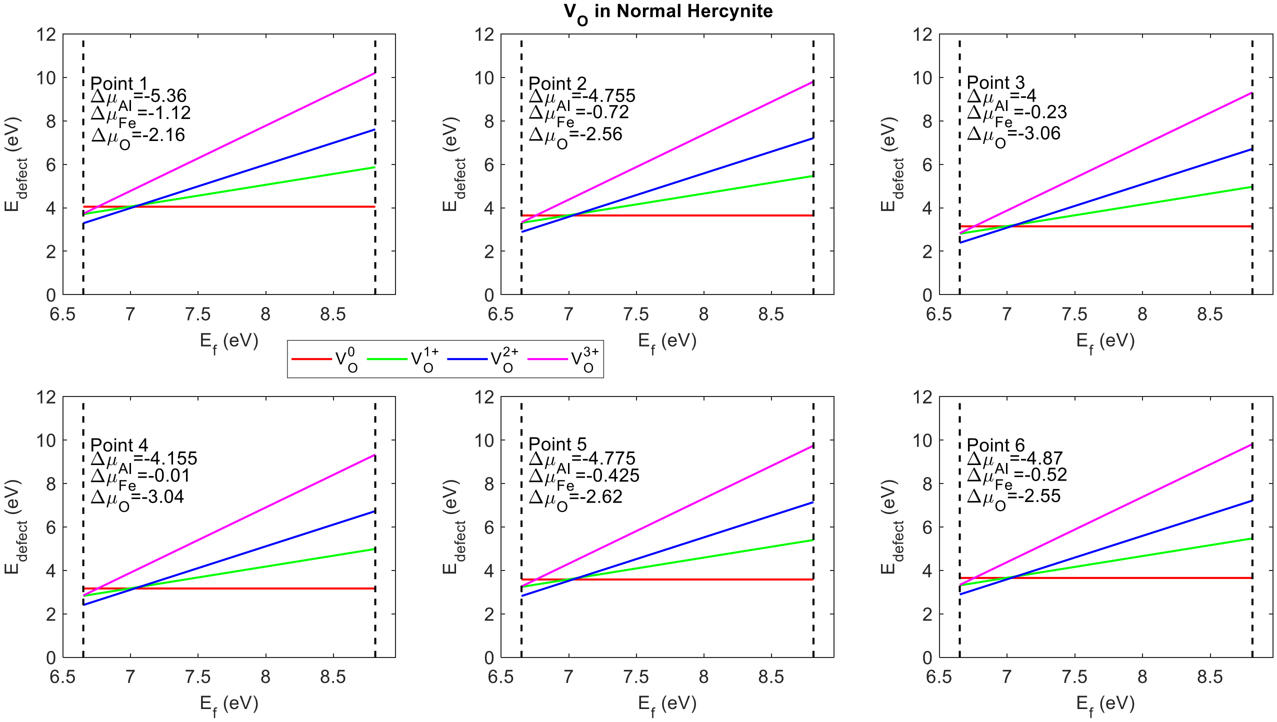

Figure 5: Oxygen vacancy formation energy of neutral and charged defects in normal hercynite.

The energy of antisite defects (i.e., Fe substituting on an Al site (Fe_{Al}) or Al substituting on an Fe site (Al_{Fe})) in hercynite are shown in **Figure 6a**. While neutral Fe_{Al} antisite defects are present at the valence band maximum (VBM), negatively charged Fe_{Al} defects are much lower in energy across most of the bandgap. Al_{Fe} antisite defects exist only in the 1^+ state. Antisite-vacancy defect pairs are shown in **Figure 6b**. The energy of these defects takes into consideration the energy to form the antisite defect, the energy to form an oxygen vacancy near that defect, and any defect pairing energy that may exist. From this it can be seen that the Fe_{Al} defects paired with oxygen vacancies are much lower in energy than oxygen vacancies found in normal hercynite. However, because the lowest energy defect pairs are negatively charged, they must be balanced by some positively charged defects. These defects come in the form of Al_{Fe}^{1+} defects. The crossover between the negatively charged $3Fe_{Al}+V_o$ defects with the positively charged Al_{Fe}^{1+} defects occurs at energies ~1eV which is low enough to be feasible at water splitting conditions. This demonstrates that these charged antisite-vacancy defect pairs are critical for understanding the water splitting ability in hercynite.

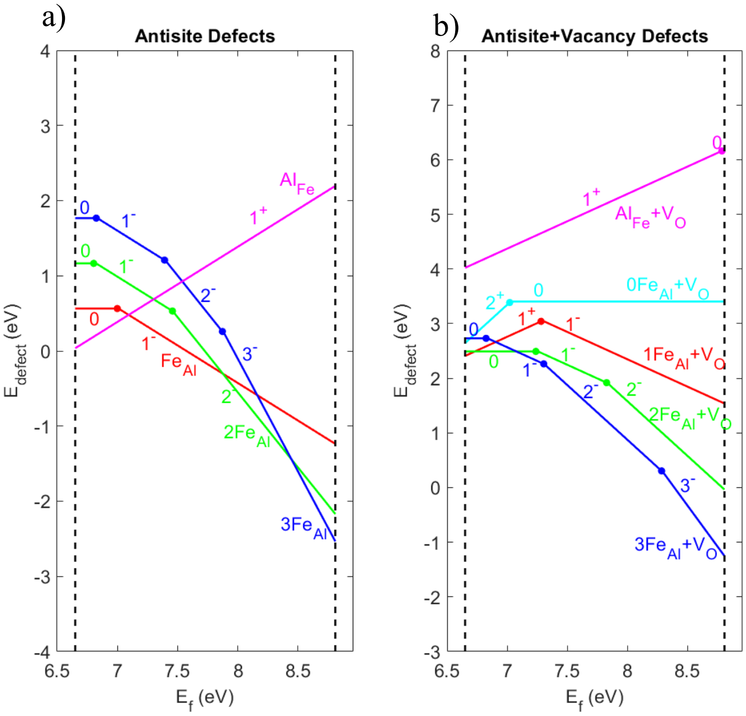

Figure 6: a) Charged and neutral antisite defects in $FeAl_2O_4$. b) Charged and neutral antisite+vacacy defect pairs in $FeAl_2O_4$.

Based on the first-principles defect calculations for herycynite paired antisite-vacancy defects, we performed thermodynamic modeling[11] to determine the stoichiometry change of $Al_2FeO_{4(1-\delta)}$ due to reduction as function of temperature (T) and O_2 partial pressure (pO_2). **Figure 7a** shows the theoretical Al-Fe-O phase diagram we calculated, expressed in terms of the elemental chemical potentials $\Delta\mu$. The ideal gas law is used to translate between $\Delta\mu_O$ and (T, pO_2). **Figure 7b** shows the predicted O vacancy (V_O) concentration for $pO_2 = 10^{-4}$ atm. When considering only isolated defects (V_O, Fe_{Al}, Al_{Fe}), the degree of reduction is very small with a maximal V_O concentration of about 10^{15} cm^{-3}. Defect pair formation (e.g., V_O-$2Fe_{Al}$) increases the O deficiency by as much as 3-4 orders of magnitude, highlighting the crucial role such pairs play in the defect thermochemistry. However, $\delta \approx 0.01\%$ still stays well below the $\delta \approx 1\%$ expected from experiments performed under comparable conditions.

An important conclusion of the present modeling is that the degree of reduction depends significantly on the cation stoichiometry. Under the Fe-rich condition (Fe excess in the form of a coexisting Fe-O phase in Fig. 1a), the O deficiency is considerably higher than under the Al-rich (coexisting Al_2O_3) condition. This finding suggests that an increased H_2 capacity could be achieved by purposefully preparing a Fe-rich composition. As a guideline, we used the predicted maximum Fe solubility in the spinel phase of about Fe/(Fe+Al) ≈ 0.5 (**Figure 7c**).

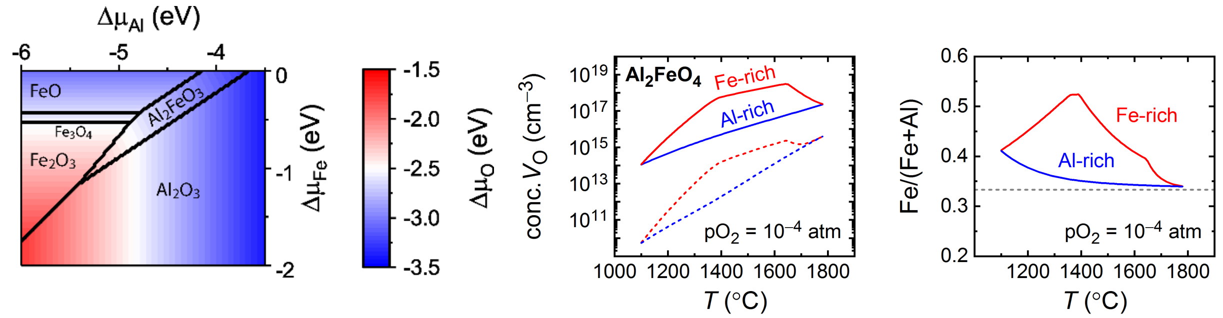

Figure 7: (a) Al-Fe-O phase diagram for the elemental chemical potentials Δμ. (b) V_O concentration as function of T at $pO_2 = 10^{-4}$ atm. The dashed line results when considering only isolated defects, the solid line is obtained when including defect pairs. (c) The resulting cation stoichiometry.

We conducted an additional investigation into the surface reconstructions of $FeAl_2O_4$ to probe the surface stability as a function of temperature (T), O_2 partial pressure (pO_2), and H_2O partial pressure (pH_2O). **Figure 8a** shows the predicted surface phase diagram. In agreement with our defect calculations, we find that an Fe-rich and O-poor surface is favored at highly reducing conditions. This finding further strengthens the idea that an Fe-rich $FeAl_2O_4$ could be favored at reaction conditions and may prove useful for determining the surface O deficiency.

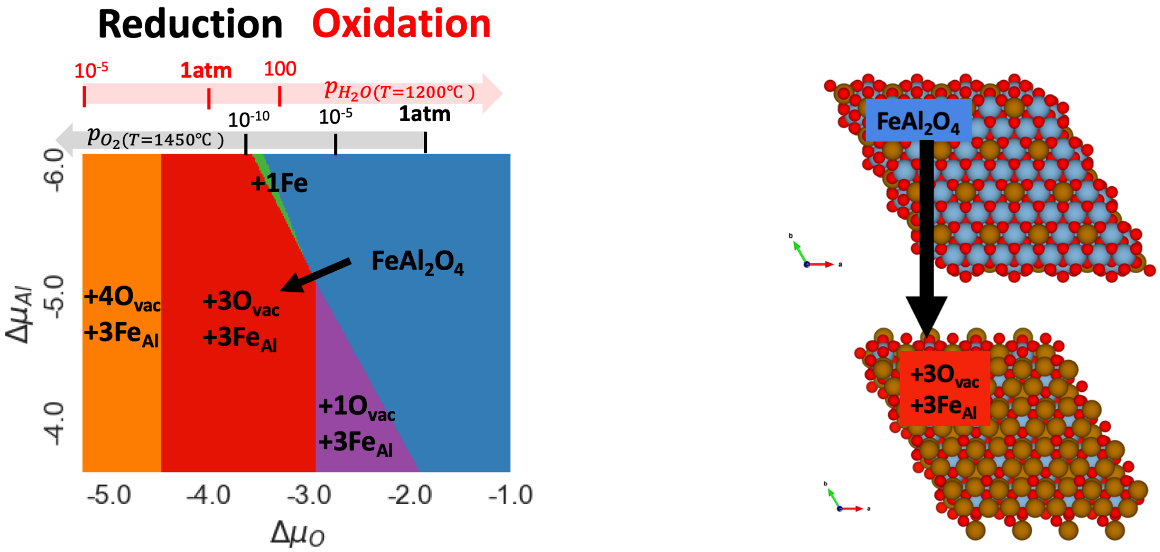

Figure 8: (a) The range of Δμ for Al and Fe is set by the stability of the $FeAl_2O_4$ phase shown in the plotted phase diagram. The surface phase diagram shows the most stable surface reconstruction relative to the most stable $FeAl_2O_4$ stoichiometric surface as a function of Δμ, pH_2O, and pO_2. (b) The structure of the stoichiometric $FeAl_2O_4$ surface (top) and a Fe-rich + O-poor reconstruction (bottom).

Our first-principles thermodynamic modeling of O_{vac} defects in hercynite showed that defect pair formation (antisite+oxygen vacancies) significantly increased the degree of reduction. As has been previously described, our thermodynamic predictions of the oxygen off-stoichiometry in hercynite using DFT+U calculations resulted in defect concentrations that are significantly below those expected from experiment (δ = 0.001% versus δ ≈ 1%). This is true even when charged defects and antisite-vacancy defect pairs are considered that raise the vacancy concentration by 3-4 orders of magnitude, depending on the temperature and partial pressure selected. This observed discrepancy between DFT+U and experimental oxygen vacancy concentrations may be caused by inaccurate vacancy formation enthalpies due to the choice of functional, vibrational contributions due to operating at elevated temperatures, or incorrect defect pair energies. We addressed each of these possible causes using beyond-DFT computation methods in order to further understand the disagreement between the equilibrium defect concentration predicted from DFT+U and the experimental H_2 production.

To understand the discrepancy, we conducted additional state-of-the-art calculations "beyond-DFT" methods to determine whether such calculations can resolve the remaining discrepancy. We also studied ternary materials by completing a deep-dive assessment of the defect mechanisms of hercynite ($FeAl_2O_4$) for STCH. In order to quantify the effect of the choice of functional on the vacancy formation enthalpy of isolated defects, we computed the defect formation enthalpy utilizing HSE and RPA/EXX. The reference neutral oxygen vacancy formation enthalpies ($\Delta\mu_O = 0$) calculated using DFT+U, HSE, and RPA/EXX are 6.24 eV, 6.22 eV, and 6.26 eV, respectively, indicating that the choice of functional only provides a minimal adjustment to the predicted oxygen off-stoichiometry of the isolate defect.

To provide an unambiguous representation of hercynite vibrational contributions at T > 0 K to the oxygen vacancy formation energy, we calculated the Gibbs free energy of the host and oxygen defective structures of hercynite using density functional perturbation theory (DFPT) within the quasi-harmonic approximation (QHA). The total energy difference

$$\Delta G_{V_O}(T) - \Delta H_{V_O}^{DFT+U}(0\ K).\ \Delta G_{V_O}(T)$$

was calculated using the following equation:

$$\Delta G_{V_O}(T) = G_{V_O}(T) - G_{FeAl_2O_4}(T) + \mu_O^{FERE}$$

where $G_{V_O}(T)$ is the total Gibbs energy for the neutral oxygen vacancy supercell, $G_{Al_2FeO4}(T)$ is the total Gibbs energy for the host supercell, and μ_O^{FERE} is the oxygen atom FERE chemical potential. We found that the lattice vibrational energy contribution to $\Delta G_{V_O}(T)$ varies non-monotonically with temperature. Specifically, at 690 K, the neutral O vacancy is maximally stabilized by 0.07 eV. However, the magnitude of this contribution decreases to zero at 1464 K and destabilizes the O vacancy by 0.04 eV at 1673 K. As a result, this contribution only provides a minimal adjustment to our DFT+U predicted $FeAl_2O_4$ oxygen off-stoichiometry at STCH conditions.

In order to investigate the effect of the choice of functional on the computed defect pair formation enthalpies we utilized the HSE meta-GGA functional to calculate the defect enthalpy of the six most prevalent defects as determined from DFT+U calculations. While RPA/EXX provides the most accurate total energies of the methods evaluated, it is computationally prohibitive for the large supercells required for modeling antisite and charged defects. Instead, we computed the defect formation enthalpies using HSE. HSE is significantly less computationally expensive than RPA/EXX and can be used on larger supercells and is known to result in improved band gaps, lattice constants, and defect energies relative to DFT.

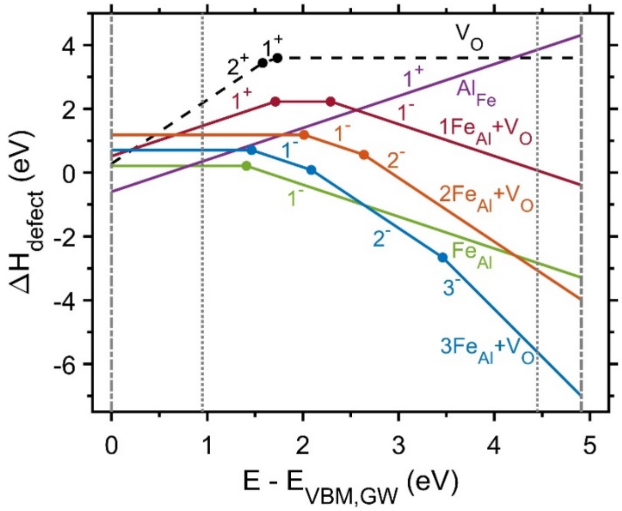

Figure 9: HSE formation enthalpies of most prevalent isolated defects and defect pairs in $FeAl_2O_4$ under Fe-rich conditions at 1400°C and $pO_2 = 10^{-4} atm$ ($\Delta\mu_{Fe} = -0.33\, eV, \Delta\mu_{Al} = -4.84\, eV, \Delta\mu_O = -2.62$). The oxygen vacancy formation energy in normal hercynite with no antisite defects is shown as a black dashed line. The GW and DFT+U band edges are shown as dash-dotted and dotted vertical lines, respectively.

The HSE computed antisite and antisite-vacancy defect pair formation energies for the most prevalent defects at 1400°C and $pO_2 = 10^{-4} atm$ under Fe-rich conditions are shown in **Figure 9**. The defect formation enthalpies calculated using HSE are very similar to those calculated using DFT+U. However, most of the defects are more favorable in HSE at the GW VBM. For instance, 1, 2, and 3 Fe_{Al}-V_O defect pairs are more favorable in HSE by 0.33, 0.28 and 0.40 eV, respectively, at the GW VBM for $\Delta\mu_i = 0$. Only the isolated Fe_{Al} is less favorable at the GW VBM in HSE, by 0.25 eV.

Based on these HSE calculations for hercynite paired antisite-vacancy defects, we performed thermodynamic modeling to determine the stoichiometry change of $FeAl_2O_{4(1-\delta)}$ due to reduction as a function of T and pO_2. In the case of isolated defects, the defect concentration predicted by HSE is less than one order of magnitude larger than that predicted by DFT+U due to the similar vacancy formation energies of the isolated defects. However, when considering defect pair formation, the O deficiency increases by 2.5 orders of magnitude for HSE as compared to the DFT+U. This results in an oxygen off-stoichiometry of $\delta = 0.8\%$ which is close to the defect concentration expected in experiment ($\delta \approx 1\%$). For both DFT+U and HSE calculations, the degree of reduction is predicted to depend significantly on the cation stoichiometry. Under the Fe-rich condition, the oxygen deficiency is considerably higher than under the Al-rich condition. This finding suggests that an increased reduction capacity could be achieved by purposefully preparing an Fe-rich composition. One unique property of this antisite-vacancy pair mechanism is that between 1550°C and 1700°C the predicted oxygen off-stoichiometry decreases with increasing temperature despite the fact that an increase in the temperature reduces the oxygen chemical potential. Without the antisite defects, oxygen vacancies cannot form. However, at these high temperatures $\Delta\mu_{Fe}$ is pinned at 0 while $\Delta\mu_{Al}$ continues to increase, making the antisite defect less favorable.

This large difference in predicted oxygen off-stoichiometry with respect to the choice of the functional is due in large part to the improved description of the dielectric constant and band gap in HSE calculations. Because HSE self-consistently corrects the band gap, both the band gap and dielectric constant are more accurate than those calculated using GGA. These are both important quantities for describing the electrostatic interactions of charged defect pairs. The dielectric constants for hercynite calculated with DFT+U, HSE, and GW are 11.4, 8.3, and 7.6, respectively, indicating that utilizing HSE instead of DFT+U will result in a significant effect on the charged defect binding energy while utilizing GW instead of HSE would only result in small changes to the defect binding energies. The cumulative change in the magnetic moment of Fe atoms neighboring a defect from their magnetic moment in bulk hercynite is less than 0.2 for all defects except Fe_{Al}, $(3Fe_{Al}, V_O)$, and $(3Fe_{Al}, V_O)^{1-}$. For those defects with small changes in the magnetic moment, this indicates that the oxidation state of Fe does not change significantly from the 2^+ oxidation state in the bulk. Depending on the overall charge of the paired defects, this may correlate to electron density being localized on the oxygen vacancy rather than reducing neighboring Fe atoms beyond 2^+. For example, in (Fe_{Al}, V_O), of the two electrons left in the lattice upon vacancy formation, one reduces the Fe_{Al} cation to 2^+ while the other remains on the oxygen vacancy site, forming a charged defect pair. For these charged defect pairs, selecting a function with a more accurate band gap and dielectric constant is critical for obtaining accurate defect formation enthalpies and corresponding defect concentrations. The three exceptions that have larger cumulative changes in the Fe magnetic moments are correspond to cases where the Fe is found in a 3^+ oxidation state because no additional electron density is available to reduce them. For example, in $(3Fe_{Al}, V_O)$ the two electrons left in the lattice after vacancy formation reduce two of the Fe_{Al} cations while the third Fe_{Al} cation remains in a 3^+ oxidation state.

We have predicted 343 ternary perovskite compositions to be stable utilizing the machine learned descriptor for perovskite stability τ. These compositions include only non-toxic, non-radioactive, and earth abundant elements. To reduce the number of DFT calculations and accelerate the screening, we have currently leveraged 2 existing materials databases: The Materials Project (MP) and The Open Quantum Materials Database (OQMD).

The OQMD contains 5329 tabulated ternary perovskite compositions, of which there are 4914 tabulated O_{vac} formation energies. This database was screened for compositions that have a vacancy energy (E_{vac}) in the range (280 kJ/mol $< E_{vac} < 500$ kJ/mol) that may drive STCH (**Figure 10**).

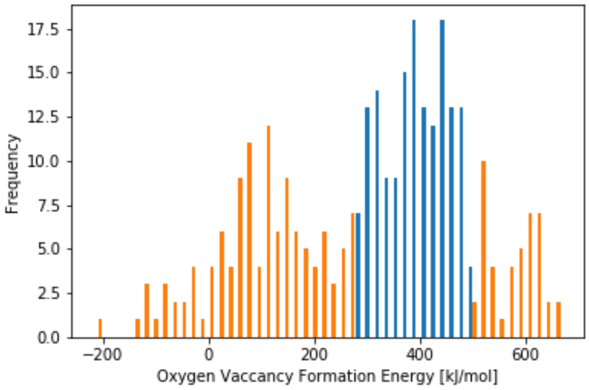

Figure 10: Tabulated E_{vac} energies from OQMD. Of the 343 τ-stable compositions, there are 158 compounds in the E_{vac} range that may drive STCH (indicated by blue bars) and only 22 compositions without a tabulated E_{vac}.

Of the 343 τ-stable ternary perovskite compositions, 158 compounds were identified in the E_{vac} range that may drive STCH. There are only 22 compositions missing from this database for which DFT calculations may be needed. To determine which DFT calculations are needed, the MP database was utilized to screen the 158 (E_{vac} in range) and 22 (E_{vac} missing) compositions for stability.

A convex hull thermodynamics analysis must be performed to evaluate stability which involves the calculation of all competing phases in a given chemical system. Performing DFT calculations on all competing phases would be extremely computationally demanding and lies outside of the scope of this project. However, the MP database contains ~60,000 oxide compositions, and so the evaluation of stability (phase diagram/hull analysis) can be performed directly from the tabulated energies existing in the database. The breakdown of the MP database stability screening of 170 compounds from OQMD is shown in **Figure 11**.

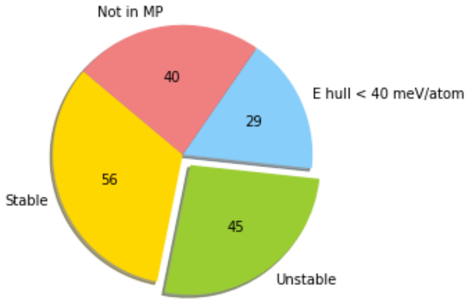

Figure 11: Breakdown of MP stability screening of 170 compounds from OQMD. There are 40 compounds that do not exist in the MP database, 29 compounds that have an E_{hull} < 40 meV/atom, 45 compounds predicted to be unstable, and 56 candidate compounds predicted to be stable.

There are 45 compounds predicted to be unstable and are therefore screened out at this stage. There are 40 compounds that do not exist in MP for which DFT calculations were performed. All DFT calculations were performed in the MP formalism with strict convergence criteria, magnetic sampling (where necessary), and without symmetry constraints to ensure: 1) a well converged geometry and 2) that these calculations are directly comparable with competing phases in MP.

There are 29 compounds with an E_{hull} < 40 meV/atom that cannot be excluded from our screening due to errors inherent to DFT on the order of about 40 meV/atom. DFT calculations were performed for these compounds. Finally, there are 56 candidate compounds predicted to be stable, which are passed to the next step in our screening: stability analysis based on oxygen chemical potential ($\Delta\mu_O$) range. The $\Delta\mu_O$ range ($-2.94 \leq \Delta\mu_O \leq -2.46$) is predicted from ideal gas calculations using the following inequalities for the thermal reduction and gas splitting steps:

Thermal Reduction: $T_{tr} \leq 1400$ °C, $pO_2 \geq 10^{-3}$ atm

Gas Splitting: $T_{gs} \geq 850$ °C, $pH_2 \geq 10^{-1}$ atm, $pH_2O = 1$ atm

A compound must be stable in this $\Delta\mu_O$ range to be viable for STCH and so a phase diagram was constructed to evaluate the $\Delta\mu_O$ stability window for a given compound using the following equation:

$$\Delta H_{f,A_xB_yO_z}(0\ K,\ 0\ atm) \approx \mathrm{x}\,\Delta\mu_A + \mathrm{y}\,\Delta\mu_B + \mathrm{z}\,\Delta\mu_O$$

The $\Delta\mu_O$ stability window can then be determined by finding the maximum and minimum $\Delta\mu_O$ for which a compound is stable. For reference, the stability windows for $FeAl_2O_4$ and CeO_2 are $-3.61 < \Delta\mu_O < -2.22$ and $-3.73 < \Delta\mu_O < 0$ respectively, both are stable in the required $\Delta\mu_O$ range. A phase diagram was constructed using the MP database for each of the 56 candidate materials and the breakdown of compounds in the specified range are shown in **Figure 12**.

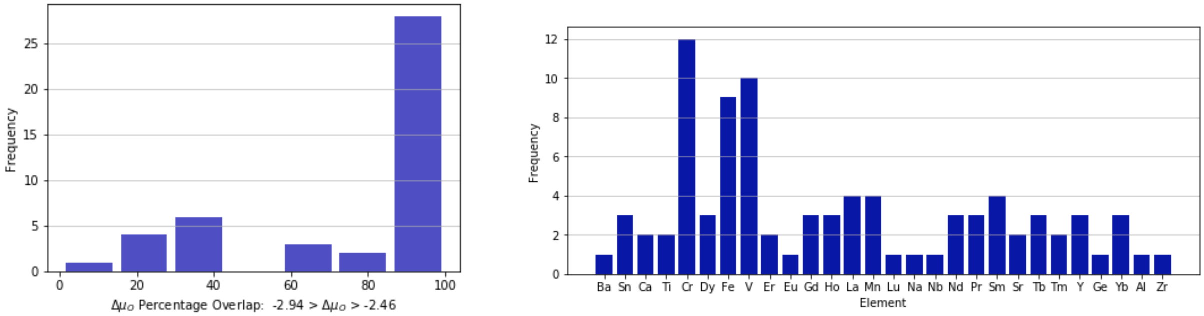

Figure 12: (**Left**) Screening of 56 candidate materials in MP database by $\Delta\mu_O$ range. Out of the 56 candidate materials only 44 are stable within the specified $\Delta\mu_O$ range. These materials are binned using the percentage of overlap with the specified $\Delta\mu_O$ range. (**Right**) The frequency of elements within the specified $\Delta\mu_O$ range.

Of the 56 candidate materials only 44 are stable within specified $\Delta\mu_O$ range. The percentage overlap with the $\Delta\mu_O$ range is an indication of how stable a material is over the full range of conditions specified above for thermal reduction and gas splitting. This value was utilized for rank ordering materials to be tested experimentally.

We have additionally utilized the MP database to screen all of the 343 τ-stable ternary perovskite compositions by stability and $\Delta\mu_O$ range as the first screening. This was done to find a set of stable compositions for which calculated O_{vac} energies to be compared to those existing in OQMD. Because we utilized different databases for our screening, an evaluation of compatibility is necessary. The breakdown of the MP screening of 343 τ-stable ternary perovskite compositions is shown in **Figure 13**.

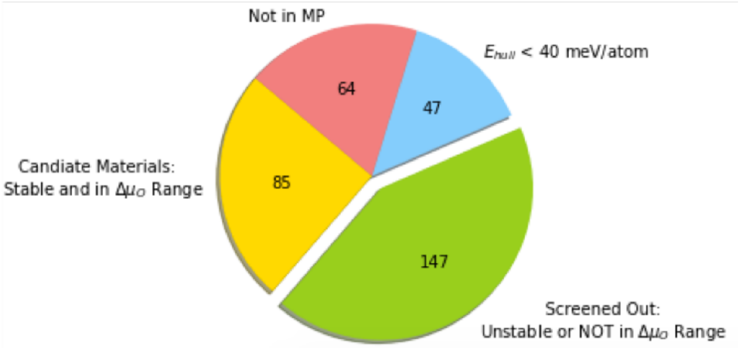

Figure 13: Breakdown of MP screening of 343 τ-stable compositions. There are 85 compositions predicted to be stable and with a $\Delta\mu_O$ within the specified range.

There are 85 compositions predicted to be stable and with a $\Delta\mu_O$ within the specified range. The O_{vac} formation energies are currently being calculated for a subset of these compositions to identify errors between the OQMD and MP formalisms used for the calculations in these databases. Using results from this analysis, we can determine if the bounds set for O_{vac} formation energy need to be expanded for screening the OQMD database.

STCH metal oxide candidate materials have been previously identified through their enthalpic requirements for oxygen vacancy formation (ΔH_{red}). However, it has been shown that the incorporation of entropic gains upon reduction can significantly enhance the performance of STCH materials. Previous work has demonstrated that materials with band gaps and highly concentrated electronic states near the conduction band could exhibit large entropic gains upon reduction. This large concentration of electronic states near the conduction band correlates to the density of states effective mass (m_e^*). The larger the density of states m_e^*, the larger the potential entropy gain upon reduction. For context, CeO_2 has an m_e^* of approximately 20 and its large electronic entropy contribution has been previously demonstrated. Additionally, magnetism and distortions are rarely considered when screening perovskites structures. We demonstrated methods for high-throughput perovskite screening with careful consideration of magnetic and distorted structures, and show that magnetism plays a key role in the energetics of vacancy formation.

Subtask 2.2: Accelerated development and optimization of reactive materials

We developed a method[14] of predicting distorted perovskites structures using SPuDS (Structure Prediction Diagnostic Software), with the only input being composition. Utilizing our machine learned descriptor for perovskite stability[4] τ in combination with SPuDS allows for rapid structure prototyping of stable perovskite structures. Traditional methods only consider the cubic perovskite and a few distortions for screening; however, our combined approach allows us to predict crystal structures with a high degree of accuracy, significantly reducing the computational expense associated with DFT calculation of the geometry, and also allowing of a larger number of distorted structures to be screened efficiently. We predicted the crystal structures of 314 τ-stable/-metastable ternary perovskite compositions in 8 unique tilting systems (**Table 1**).

Table 1: The 8 unique tilting systems considered in this project with frequency of tilting distortions found experimentally.

Glazer Tilt System	Space Group	Crystal System	Expt. Frequency
a+a+a+	Im-3	cubic	22
a-b+a-	Pnma	orthorhombic	119
a-a-a-	R-3c	trigonal	24
a+b0c-	Cmcm	orthorhombic	6
a0b-b-	Imma	orthorhombic	6
a0a0c+	P4/mbm	tetragonal	5
a0a0c-	I4/mcm	tetragonal	9
a0a0a0	Pm-3m	cubic	21

For each of the 2,512 structures comprised of 314 perovskite compositions in all 8 tilting systems a crystal structure was predicted using SPuDS and then a structural relaxation was performed using DFT. The resulting DFT predicted volume of the unit cell was compared to the SPuDS prediction (**Figure 14**).

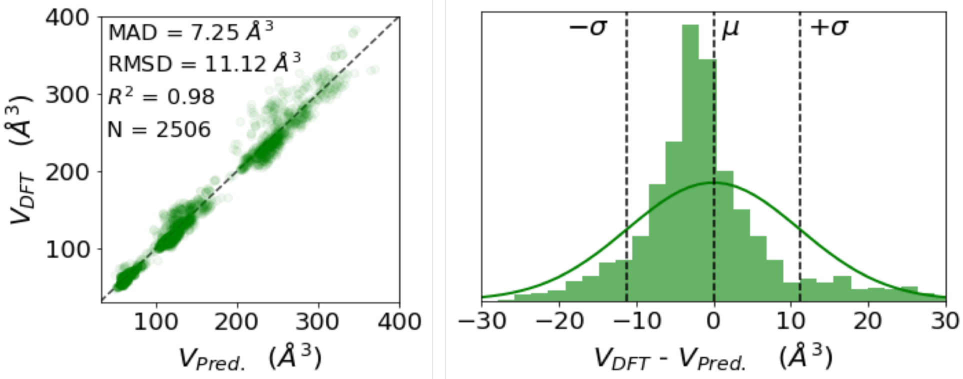

Figure 14: SPuDS prediction comparison to DFT results. The mean absolute deviation (MAD) is 7.25 Å^3 and the R^2 value is 0.98, showing fantastic agreement with DFT results. MAD is the mean absolute deviation, RMSD the root mean square deviation, N the number of points shown, μ the mean deviation and σ the standard deviation.

We utilized the bond valance method (BVM) in order to rapidly predict the structures and stabilities of 316 cubic ternary perovskite oxides. BVM can predict likely crystal structures from the “bond valence” of cation-anion pairs in a given crystal lattice both accurately and efficiently. This enables a key link between machine learning and quantum simulations in the high throughput search for new STCH redox mediating materials. BVM’s bond valence terms are empirically derived from experimental data and can be used to “rank order” the relative stability of different crystal structures. BVM is an attractive approach to crystal structure prediction because it: a) requires only composition and b) has been shown to yield crystal structures that agree well with experiment. We demonstrate how similar bond valence generated structures are to those of experiment when relaxed using density functional theory (DFT) in **Error! Reference source not found.**. Here, the lattice constant and formation energies of 316 DFT-relaxed cubic perovskite oxides are compared to DFT-relaxed ICSD experimental structures from the Materials Project database. Both lattice parameter and formation energy are very highly correlated, with $r^2 > 0.99$ for both properties. This suggests that BVM can accurately capture experimental cubic crystal structures. The implications of this are highly significant. If BVM can also be shown to capture the experimental crystal structures of complex perovskite oxides, new complex perovskite spaces could be rapidly and accurately explored computationally. With STCH-active materials known to exist in these complex spaces, rapid exploration using BVM and DFT could yield even more novel STCH compounds.

DFT structural relaxations were performed for the 314 ternary oxide perovskites predicted to be stable/meta-stable using τ. The predicted volume matches the DFT relaxed volume well with an R^2 of 0.98 and a mean absolute deviation of 7.25 Å^3. In addition to the volume comparison, we also utilized *structural fingerprinting* as a method to quantitatively compare the simularities of different structures. This fingerprinting method involves calculation of various statistics of bond lengths, angles, and coordination environments for each structure. Then, the difference between two structures can be computed by taking the normed vector distance between the two structural fingerprints. This value, SFPD (structural fingerprint distance), was calculated between the ground-state DFT predicted structure and SPuDS predicted structure. SPuDS minimizes the *Global Instability Index* (GII) to predict the distortions and attempts have been made previously to use GII as a measure of stability. We find that although GII does not directly correlate with stability, it still can be utilized for rank ordering distorted structures to predict the likelihood of stability. We found that 98% of the correct ground state structures are predicted to be among the 3 lowest GII structures of the 8 total distorted structures.

The mean SFPD value between the SPuDS-predicted structure and the DFT ground state structure is 0.42. The typical SFPD values for comparing the structures of cubic and distorted perovskites are 1.5 – 2, significantly larger than 0.42. This shows that SPuDS provides an accurate prediction of the structure of perovskites, especially considering its low computational expense. This provides a good starting guess for stable structures that significantly reduces the cost of each DFT relaxation with only the negligible additional cost of a SPuDS calculation. Beyond providing an improved starting structure for the DFT calculations and determining the stable polymorph, SPuDS also enables the use of structural descriptors in a machine learned model, as opposed to only compositional descriptors, to identify promising material properties. Additionally, for each of the 8 tilting systems given by SPuDS, the Global Instability Index can be computed which provides an indication of the relative stability of the predicted polymorph structures. By utilizing the GII to rank-order the possible perovskite tilting systems, the number of calculations required for each composition to capture the DFT ground-state structure with 98% confidence is 3 whereas without SPuDS, 8 DFT geometry optimizations are required to predict the most stable structure from the 8 titling systems with 100% confidence. Furthermore, SPuDS allows 100% of the correct ground state structures to be identified with 5 DFT optimizations, thus reducing the number of DFT optimizations from 8 to 5 to have 100% certainty of identifying the DFT predicted ground state polymorph. This combined approach of applying the machine-learned descriptor τ to initially screen for perovskite stability, then utilizing SPuDS to generate initial starting structures, and finally evaluating the GII to determine the most stable tilting systems *not only reduces the computational expense of each DFT relaxation by providing a better starting guess geometry, but it also significantly reduces the number of DFT calculations needed to identify the most stable distorted structure*.

Additionally, GII can be utilized to further screen perovskites for stability. We found that unstable polymorphs possess GII > 0.1 v.u. except for perovskites that are predicted to be cubic. The GII threshold is set to 0.1 v.u. for ternary perovskites that lie within 100 meV of the convex hull. This allows for screening of stable polymorph structures from only composition, except for cubic structures. For the cubic perovskites, the minimum GII always predicts the cubic structure to be the most stable due to insignificant tilting of the remaining 7 structures, meaning only a single DFT calculation is needed for GII predicted cubic perovskites.

We went beyond traditional high-throughput screening approaches by performing DFT calculations without symmetry constraints and with magnetic sampling to screen ternary perovskite compositions by stability and vacancy formation energy (**M2.1.3**). The workflow is as follows: 1) identify τ-stable compositions, 2) predict distortions using SPuDS, 3) perform ferromagnetic structure relaxation to identify stable polymorphs, 4) magnetically sample stable polymorphs, 5) map magnetism to supercell and perform O-vacancy calculations for all symmetrically unique sites. A critical difference between our approach and traditional approaches is the sampling of O-vacancies in symmetrically unique sites. Although in the ternary perovskite structure all oxygen sites have identical coordination environments, bond lengths, and nearest neighbors, the inclusion of magnetism breaks this symmetry, and as is shown in **Figure 15**, can lead to very different vacancy formation energies.

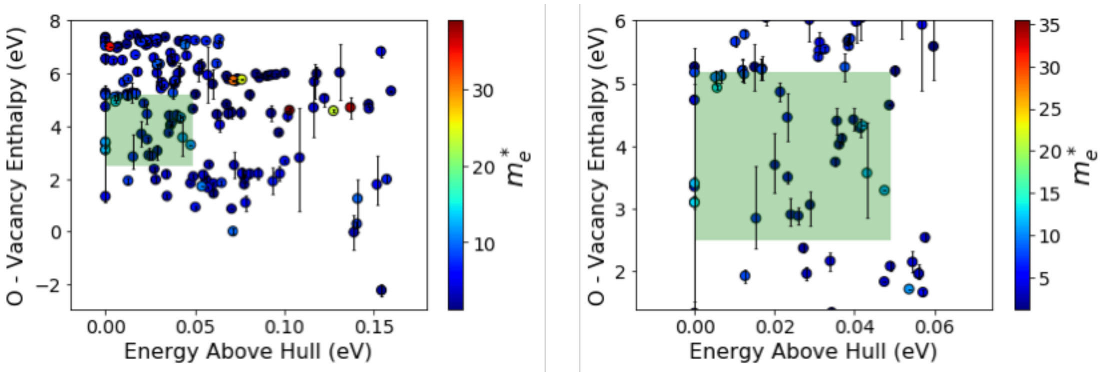

Figure 15: Left: Oxygen vacancy formation enthalpy and stability of τ-stable ternary perovskite compositions. Right: Zoomed in plot of Left. The green highlight shows the area of interest for water splitting materials. The color bar shows effective mass of electrons at 1000K. The error bars show the max/min oxygen vacancy formation energies.

The green rectangle in **Figure 15** indicates the region of interest for water splitting materials in terms of the vacancy's ability to split water and the perovskites stability. We found that only a few compositions lie within this window and we found even fewer compositions that have "large" m_e^*. None of the ternary perovskites in this window have an m_e^* comparable to CeO_2. There are however a few compositions that posses an m_e^* larger than CeO_2 that are stable/meta-stable. Optimizing these materials through alloying could shift the vacancy formation energy into the optimal window for STCH. Interestingly, we find that $BaCeO_3$ and $LaAlO_3$ have large effective masses and some of the known water splitting materials are alloys of these two compositions. Additionally, $GdAlO_3$ and $GdGaO_3$ have very large m_e^* and we plan to explore alloys of these materials further. Some materials in **Figure 15** have large error bars, demonstrating the importance of magnetism in vacancy formation. These differences can be as large as 2.5 eV in some of the Ni containing perovksites, showing that a single, ferromagnetic oxygen vacacny calculation is insufficient to properly describe vacancy formation, which demonstrates the nessecity of our more thorough screening approach.

A subset of ternary oxides ($LaBO_3$ and $GdBO_3$ compounds, where B is any other element on the B site in the perovskite structure) were examined for their m_e^*. The computed crystal structures of these compounds were taken from the Materials Project Database. $LaBO_3$ compounds exhibit a broad range of oxygen vacancy formation enthalpies across B-site elements (approximately 1.5 to 6.5 eV/atom.) However, these thirteen $LaBO_3$ compounds also possess m_e^* significantly below that of ceria. Of the thirteen compositions considered, five structures are metallic (do not possess a band gap) and therefore a DOS m_e^* could not be calculated. Of the eight ternary perovskites with a band gap, $LaFeO_3$ reported the highest m_e^* at 11.97. There are fewer converged $GdBO_3$ structures (6) compared to $LaBO_3$ structures (13). This is due to limited representation of $GdBO_3$ compounds in the materials project database. This could also explain why the ternary $GdBO_3$ perovskites do not exhibit the same continuum of ΔH_{red} as $LaBO_3$. Only two converged structures exhibit ΔH_{red} less than ~ 4.5 eV/atom. One of these structures ($GdFeO_3$) has a large negative ΔH_{red}, suggesting phase instability. However, both $GdAlO_3$ and $GdGaO_3$ structures exhibit m_e^* larger than ceria (~38 and ~26, respectively.) This suggests large ΔS_{red} could be exhibited by select $GdBO_3$ compositional subspaces.

We identified the 0 K DFT-predicted ground state geometry of 544 promising STCH ternary perovskite oxide compositions using a modified bond valence method with anion/anion interactions (BVM_{oo}). Ternary perovskite oxide starting structures in different lattice geometries (polymorphs) were generated using BVM$_{oo}$ and subsequently optimized with DFT. As demonstrated by the similarity of their structural fingerprints, which is a vector representations of a structure based on the location and identity of species in the lattice, the BVM$_{oo}$ generated structures are very similar to DFT optimized structures both prior to and following DFT relaxation. This greatly accelerates the optimization of DFT structures and thus the subsequent evaluation of promising materials by DFT.

This similarity not only improves the rate at which BVM$_{oo}$ structures converge to their DFT-relaxed structure, which is highly useful for high-throughput exploratory schemes of large theoretical materials spaces, but also justifies using BVM$_{oo}$'s *built-in* Global Instability Index (GII$_{oo}$) measure of instability to prescreen lattice geometries. The GII$_{oo}$ is the root mean square of BVM$_{oo}$ "discrepancy factors" normalized per atom; GII$_{oo}^2$ has been previously shown to be correlated with overall energy. The Pearson coefficient between GII$_{oo}^2$ and DFT-computed formation energy (i.e. their energies relative to their competing elemental phases) confirms this relationship for most compositions in our dataset. Shown below are the Pearson correlations for the 530 ternary perovskite oxide compositions that possess at least 3 structurally unique polymorphs.

The tendency for formation energy and GII$_{oo}^2$ to be strongly, positively correlated suggests that GII$_{oo}^2$ provides fundamental insight into the relative stability of competing polymorphs. We therefore quantified the frequency that a polymorph is the DFT-predicted ground state based upon its GII$_{oo}^2$ value. Our results show that ~90% of ground state polymorphs are captured when all polymorphs with GII$_{oo}^2$ ≤ 0.2 are computed. This increases to ~95% when all polymorphs with GII$_{oo}^2$ ≤ 0.3 are computed. We note that because GII$_{oo}^2$ is so computationally efficient to compute, it provides a way to greatly accelerate the determination of stable polymophs in addition to the structures to be then evaluated by DFT.

Our results also show that the DFT predicted ground states primarily possess the Pnma lattice symmetry (~93% of all compositions). This high frequency offers another potential avenue to pre-screen lattice geometries prior to DFT calculations, as certain lattice geometries (such as I4/mcm and Pm-3m) are never the predicted ground state in our dataset. These geometries--- at least for single perovskite systems--- can likely be confidently bypassed. One question to still be addressed is if these lattice symmetries remain the ground state structures at STCH temperatures.

Finally, we quantified the proportion of polymorph pairs that are correctly ordered by GII$_{oo}^2$ according to their DFT-computed stability as a function of their GII$_{oo}^2$ difference. We took the difference in GII$_{oo}^2$ between each pair of competing polymorphs in a system (represented in the **Figure 16** by *i* and *j*) and labelled them as correctly or incorrectly ordered. These polymorph pair orderings were then binned by GII$_{oo}^2$ difference, upon which a positive, logarithmic trend was observed. A logarithmic "likelihood" curve was fitted to the resulting points. Assuming that our dataset is representative of the larger perovskite space, this relationship could be used to predict the likelihood that any two polymorphs are correctly ordered according to their GII$_{oo}^2$ values.

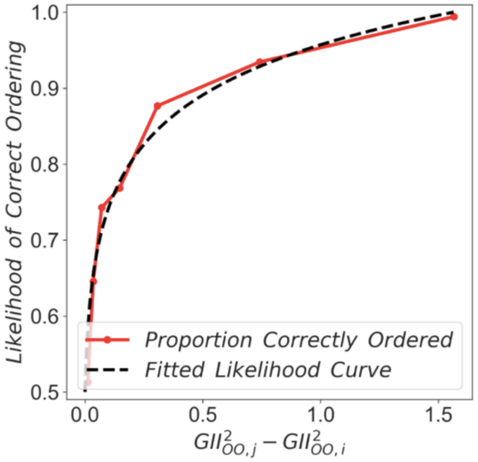

Figure 16: Likelihood of correct polymorph ordering by GII_{oo^2}.

We benchmarked the ability of DFT to predict experimental synthesizability by computing the decomposition enthalpies (ΔH_d) of 229 experimentally realized ternary perovskite oxides. Perovskite polymorph structures were generated in 11 Glazer tilts using the Global Instability Index (GII) minimization procedure implemented within the Structure Prediction and Diagnostic Software (SPuDS) package. **Figure 17** shows the distribution of ΔH_d values for the DFT computed ground state Glazer tilts; a significant number of polymorphs have ΔH_d values over 100 meV/atom and a few even exceed 200 meV/atom, well beyond the range that is typically used to predict experimental synthesizability (50-100 meV/atom). This suggests that experimentally synthesizable perovskites can exhibit decomposition enthalpies well above the convex hull; the broad variability of decomposition enthalpies has been accounted for in our current multinary oxide screening procedure.

Figure 17 shows the distributions of decomposition enthalpies (ΔH_d) for eight preserved Glazer tilts calculated relative to their Materials Project tabulated competing phases. Distributions are ordered (top to bottom) by mean stability of each Glazer tilt, from the most stable --- orthorhombic (Pnma) to the least stable --- cubic (Pm-3m). The overwhelming majority (189/200) of DFT predicted ground states in our dataset originate from the orthorhombic Pnma (a-b+a- Glazer tilt) structure, whereas the overwhelming majority of least stable Glazer tilts in our dataset (193/200) originate from the cubic Pm-3m (a0a0a0 Glazer tilt) symmetry. Consistent with our own and other previous investigations, this confirms that the cubic Glazer tilt is not the DFT predicted ground state for the majority of experimentally realized perovskite oxides. This further reinforces our contention that accurate DFT predictions of ABO_3 perovskite stability must consider distortions from the cubic structure.

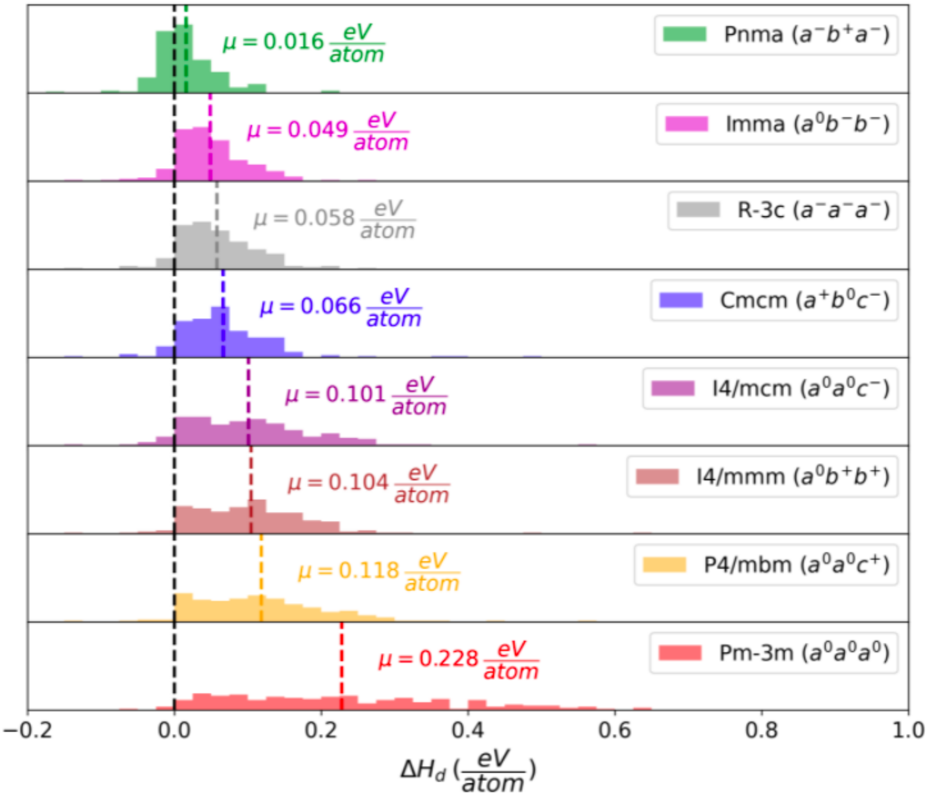

Figure 17: Distribution of ΔH_d (200 ABO_3 compositions) for the eight preserved Glazer tilts in our dataset. The dashed black line indicates $\Delta H_d = 0$ eV/atom, and the dashed colored lines represent the mean ΔH_d for each Glazer tilt; the bin width is 0.025 eV/atom. Cubic (Pm-3m) polymorphs are generally the least stable Glazer tilt and the orthorhombic (Pnma) Glazer tilt, identified as the ground state space group in 189/200 compositions, is generally the most stable.

The computed crystal structures of Gd and La ternary oxide perovskites were used to predict new alloyed perovskites. Ternary perovskite structures were taken directly from the Materials Project database. Alloyed perovskites were generated using the Special Quasirandom Structures (SQS) algorithm from the Alloy Theoretic Atomic Toolkit (ATAT) and the Data Mined Ionic Substitution module (DMSP) from the Pymatgen python library. For SQS, 50% of perovskite A-sites were assigned the label A', and 50% of perovskite B-site were assigned the label B'. SQS simulates random disorder of A, A', B and B' species. The Data-Mined Ionic Substitution Probability model (DMSP) developed by Hautier *et al.* was used to determine highly probable A'→A and B'→B substitutions. Highly probable elemental substitutions in base structure A and B sites were substituted for A' and B' sites in the disordered $AA'BB'O_6$ templates. The relaxed structures of these substituted multinary perovskites were then calculated using DFT.

Using this screening criteria, several Gd oxide perovskite compounds with large density of states m_e^* were identified. Oxygen vacancy formation energies were also calculated from 10 uniquely sampled oxygen sites for the Gd compounds. The largest Gd oxide m_e^* are significantly larger than that of the La oxides, and even larger than that of CeO_2. The Gd_2AlGaO_6 formulation is particularly interesting because it exhibits oxygen vacancy formation enthalpies in the range of ~4.2 to 4.9 eV. This range is near the calculated oxygen vacancy range of CeO_2 of ~4.7 to 5 eV, but the effective m_e^* of this material is approximately 30. This represents a 33% increase in m_e^* compared to CeO_2.

This suggests that stable Gd-Ga-Al oxide perovskites, among other Gd compounds, could be of interest for further study.

In addition to using the SQS approach to generate random alloy configurations, we also validated the SPuDS structure prediction approach on a number of multinary perovskite compositions (**Figure 18**).

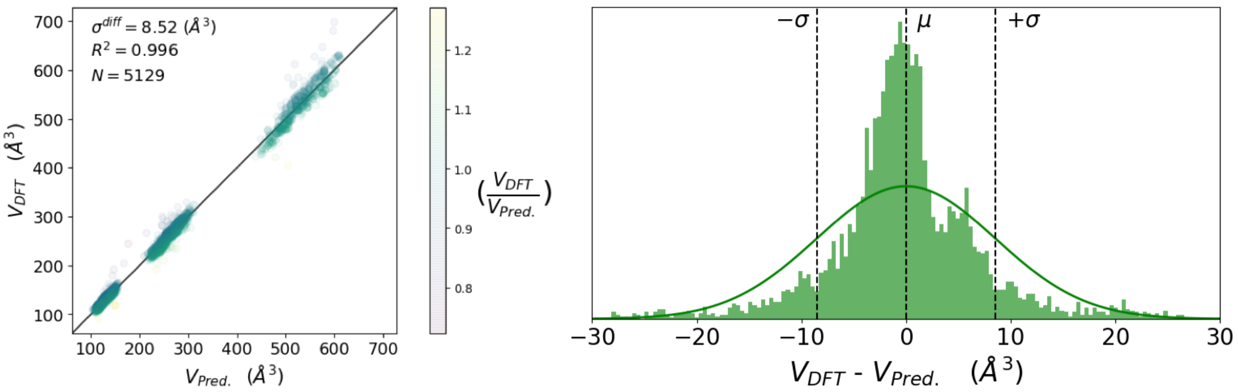

Figure 18: SPuDS predictions vs DFT for multinary perovskites. The predicted structures agree with DFT structures similar in magnitude to the ternary compositions.

The SPuDS predicted structures for the multinary perovskite compositions agree well with the DFT calculated structures, allowing us to use SPuDS for structure prediction beyond the ternary space. We utilized the SPuDS structure prediction method to predict structures that can serve as good initial geometries for DFT to minimize the computational expense of DFT geometry optimizations. Furthermore, we used SPuDS' ability to efficiently predict structures and their relative energies to screen for stable perovskite polymorphs. We also demonstrated that SPuDS predicts structures that are quantitatively similar to DFT optimized structures. We constructed a python interface to the SPuDS software to enable the high-throughput prediction of perovskite structures. We subsequently used this interface to create a database of multinary perovskite structures for 75,782 charged balanced/size constrained compositions, resulting in 527,955 structures in seven of the most likely glazer tilting systems.

We previously reported a new effort to utilize structure prediction (SPuDS) to minimize the computational expense of DFT geometry optimizations and to screen for stable perovskite polymorphs. Furthermore, we have previously applied the structural fingerprinting measure of structural dissimilarity to demonstrate that SPuDS predicted structures are quantitatively similar to DFT optimized structures. We have employed our new python interface to SPuDS developed to enable the high-throughput prediction of perovskite structures, to increase our database of multinary perovskite structures from 75,782 to 120,145 charged balanced/size constrained compositions. Thus, we have expanded our database by over 308K structures, now totaling 836,217 predicted structures in the various crystal structures (glazer tilting systems, **Figure 19**).

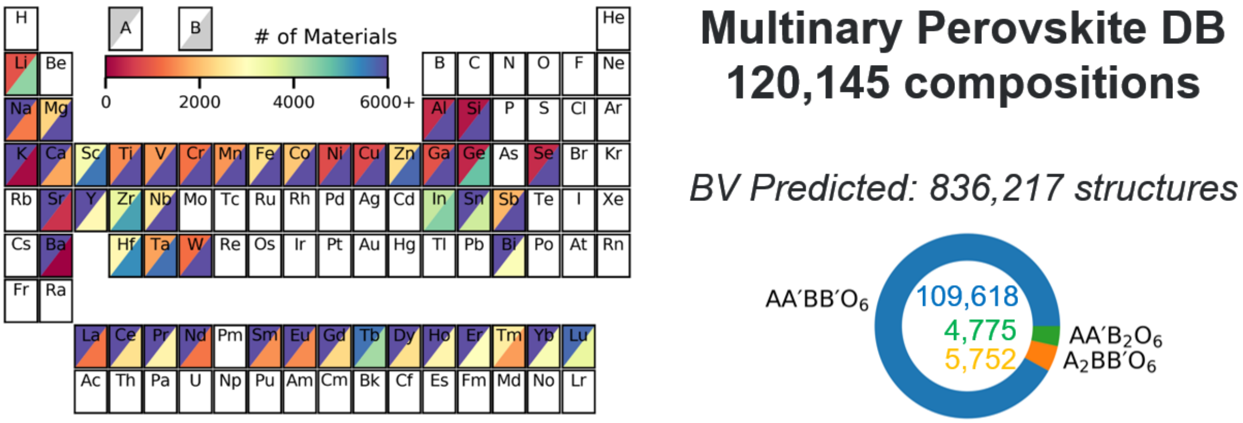

Figure 19: Multinary Perovskite Database: Bond valence structure prediction using the SPuDS program for 120,145 unique compositions resulting in 836,217 crystal structures. Our database contains 109,618 AA'BB'O_6, 4,775 AA'B_2O_6, and 5,752 A_2BB'O_6 compositions. The periodic table plot shows the elements present in our database. The shading indicates the frequency of compositions with the element on the A site (upper left) and B site (bottom right).

Our constructed database contains machine learned (ML) stability predictions using the ML descriptor tau for each composition and Global Instability Index (GII) predictions for each structure. These perovskite structures have rock-salt B-site ordering and A-site ordering determined by a minimum Ewald summation of all symmetrically unique A-site orderings. Additionally, our database contains the .cif files for each structure with the partially occupied Wycoff sites (before A site ordering).

For reference, the Materials Project (MP) contains a total of about 60,000 oxide structures consisting largely of non-perovskite compositions. Our new data base, which were added to MP, and is the largest ever created for oxides and especially perovskite oxides. Utilizing the oxide structures from MP in combination with our database allows for rapid screening of stable STCH candidates in this vast chemical space. Additionally, these predicted structures allow for use of structural descriptors in ML models developed later.

We uploaded our multinary perovskite database to Materials Project. The results of all our calculations are open source and readily available on the MP website. Furthermore, we initiated a collaboration with MP about creating a perovskite specific app complete with metadata such as A-site, B-site, element oxidation states, tau predictions, and more, to make it easier for open-source development of perovskite specific ML models. Additionally, we have started development of structure prediction software for perovskites, similar to SPuDS, but written in Python and with improved functionality, to be implemented the pymatgen python package and possibly on the main MP website. The new software features many improvements over SPuDS such as: 1) allowing structure predictions in all 23 unique glazer tilting systems compared to the maximum of 11 allowed in SPuDS, 2) adding anion-anion interactions, a major drawback in SPuDS that results in unfavorable O-O bond distances due to over tilting in some glazer systems, 3) enabling additional structures to be added such as layered perovskites and other ionic structures, and 4) enabling rapid, automated predictions of hundreds of thousands of accurate perovskite structures.

To date, we have performed DFT optimizations for 44,711 multinary perovskite compositions in 68,928 tilting structures and have calculated oxygen vacancy formation energies for 108 of the compositions determined to be stable using a convex hull analysis.

The stability of each ground state structure was determined by comparing the structure's decomposition enthalpy to that of its competing phases (as tabulated by the MP database.) Because our DFT stability analysis is at 0 K, and STCH temperatures range between 1000 K and 1650 K, we used a stability cutoff of 200 meV/atom above the convex hull. We used this cutoff so as not to exclude perovskite oxides that could be stable at high temperature. 7,000 complex perovskites oxide compositions were shown to fall within this cutoff. The distribution of decomposition enthalpies is shown in **Figure 20** with those materials that fall within the stability cutoff highlighted in green.

As discussed above, it has been shown that the incorporation of entropic gains upon reduction can significantly enhance the performance of STCH materials. Previous work has demonstrated that materials with band gaps and highly concentrated electronic states near the conduction band minimum (CBM) could exhibit large entropic gains upon reduction through the formation of charged defects. The concentration of electronic states near the CBM can be represented by the density of states (DOS) m_e^*, with larger m_e^* corresponding to larger potential entropy gain upon reduction. The effective mass of the 7,000 materials that fall within the stability cutoff are shown in **Figure 20**. Materials having a higher m_e^* than ceria (~20) are highlighted in yellow; 76 perovskites fall within this range.

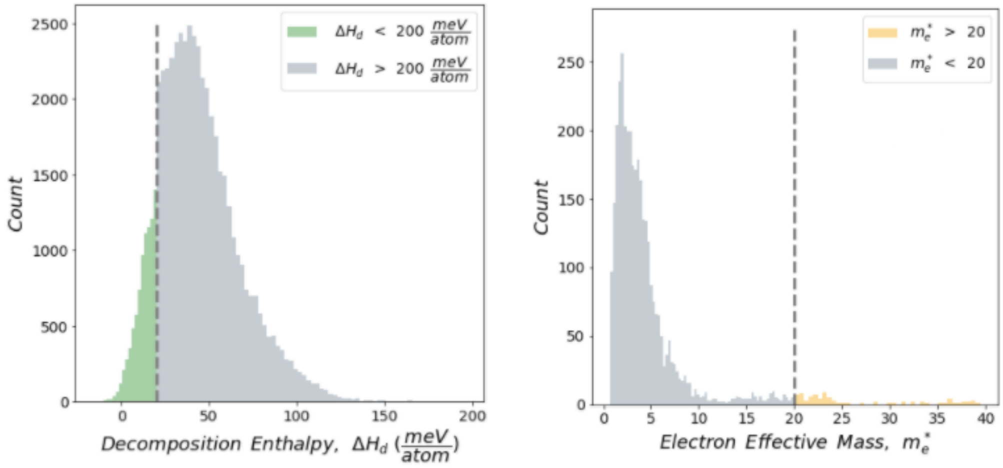

Figure 20: Distributions of ~50,000 AA'BB'O_6 perovskite oxide decomposition enthalpies (left) and ~7,000 AA'BB'O_6 perovskite oxide electron effective masses (right). The distribution of compounds below the 200 meV/atom decomposition enthalpy cutoff and above the m_e^* cutoff of 20 are shown in green and yellow, respectively.

In addition, we have calculated the DOS m_e^* at 1000 K for all stable oxides within 50 meV of the convex hull in the MP database with tabulated DOS information, including non-perovskite compounds. Furthermore, we have projected the DOS on to oxidation state decorated species to identify the elements that most contribute to compositions with large m_e^*, and compared the results from all MP oxides to stable perovskites from our calculated multinary perovskite database.

In our work to develop a descriptor for high m_e^* compounds, we found that only three elements, Ce, Gd, and La, on average produce stable compositions with the highest m_e^*. However, these calculated m_e^* are not particularly accurate due to using the DOS, which does not contain sufficiently sampled data for the calculation of m_e^*. However, this information is not readily accessible from the MP database and so we performed the analysis in **Figure 21** with the information available. A more accurate method involves utilizing eigenvalues to obtain the weighted integration along various k-point symmetries. This information is available in our calculated multinary perovskite database and thus, we have performed an analysis using this more accurate method (**Figure 21**).

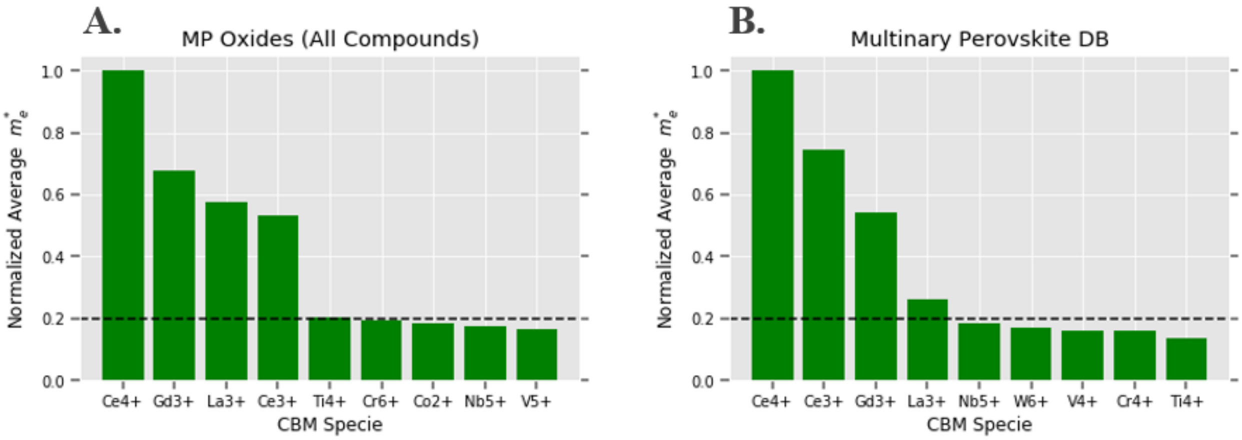

Figure 21: A) Normalized average m_e^* comparison to the species with largest contribution to m_e^* for all stable MP oxides including non-perovskite compounds. Three elements of interest for STCH, namely Ce, Gd, and La, show significant contributions to compounds with the largest m_e^*. B) Normalized average m_e^* comparison to the species with largest contribution to m_e^* for stable multinary perovskites in our calculated database. The same three elements, Ce, Gd, and La, are present in perovskite compositions with high m_e^*.

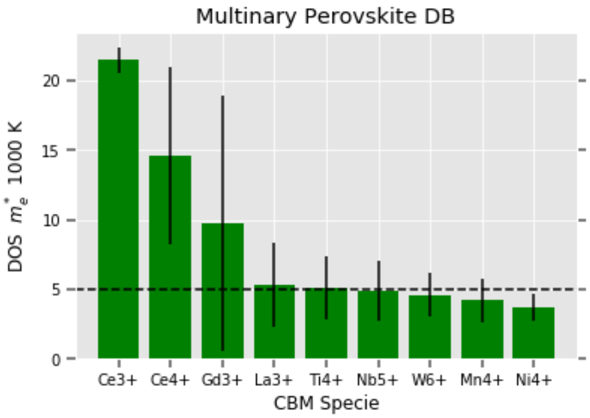

Figure 22: Calculated average DOS m_e^* at 1000 K comparison to the species with largest contribution to m_e^* for the stable multinary perovskites in our calculated database. The error bars show the max/min m_e^* values for each specie. Again, the same three elements, Ce, Gd, and La, are present in perovskite compositions with the highest m_e^*, further highlighting the significance of these elements in the design of compositions with large m_e^*.

Ce and La are commonly found in known water splitting materials and it has been previously reported that CeO_2 ($m_e^* \approx 20$) has a large electronic entropy that contributes significantly to its water splitting ability. Interestingly, we find both Ce and La are present in perovskite compositions with the highest m_e^*. From the ternary perovskite screening conducted previously, we showed that Gd containing compositions had large m_e^*. We had again identified Gd as a potentially interesting element to be utilized in the design and optimization of high m_e^* multinary perovskite compositions, a previously unexplored space for STCH. The error bars in **Figure 22** provide an indication to the degree of m_e^* tunability for each specie in the multinary perovskites space. Of all elements of interest for STCH, Gd shows the highest promise for compositional tuning to maximize m_e^*.

Most significantly, we have shown that La, Gd, and Ce are dominantly present in oxide compounds with large m_e^* even outside of the perovskite space. Further investigation into the structure/composition m_e^* relationship will likely expand the candidate materials space beyond spinels and perovskites for identification of optimal STCH materials.

Finally, neutral oxygen vacancy calculations were performed for the 76 stable perovskite candidate compositions with high m_e^*. A distribution of the minimum and maximum calculated oxygen vacancy enthalpies for these compositions is shown **Figure 4**. Nearly 40 compositions exhibited calculated oxygen vacancy enthalpies within the predicted STCH active range (2.5-5 eV). Additionally, a linear-regressed model was developed to predict the oxygen vacancy enthalpies of perovskite oxides, as shown in **Figure 4b**. Using the formation enthalpy, band gap and oxygen 2p band centers of a bulk material, the oxygen vacancy enthalpy of ternary and complex perovskites could be predicted with similar mean absolute error (MAE.) Further fine-tuning of this model to improve MAE could result in accurate oxygen vacancy enthalpies without the need for explicit calculations. This would enable the rapid exploration of complex perovskite oxide spaces.

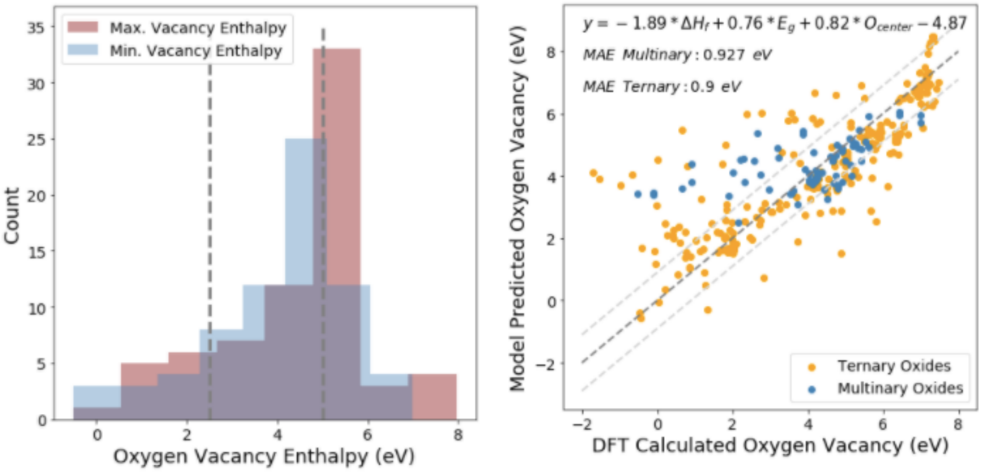

Figure 4: Left) Distributions of the maximum and minimum oxygen vacancy enthalpies calculated for the 76 identified candidate perovskite materials. The number of oxygen vacancies calculated per material was dependent upon the number of unique oxygen sites in that material's crystal lattice. Right) Scatter plot of oxygen vacancy predictions using a linearly-regressed model (equation shown in figure.) ABO_3 compositions are shown in yellow, whereas $AA'BB'O_6$ are shown in blue.

As discussed above, it has been shown that the incorporation of entropic gains upon reduction can significantly enhance the performance of STCH materials. Previous work has demonstrated that materials with band gaps and highly concentrated electronic states near the conduction band could exhibit large entropic gains upon reduction through the formation of charged defects. The concentration of electronic states near the conduction band minimum can be represented by the density of states effective m_e^*, with larger m_e^* corresponding to larger potential entropy gain upon reduction. However, in order for this large m_e^* to be realized as a large entropic gain, the cross-over between charged defects and neutral defects must occur near or above the conduction band edge. We developed a high-throughput workflow to calculate charged defect formation enthalpies. These calculations are considerably more computationally demanding than the calculation of neutral vacancies due to the need to accurately determine the energetic effect of removing electrons from the system and the inherent dependence of the defect enthalpy on the Fermi level.

We identified Gd and Ce as potential dopants to maximize the electronic entropy of reduction. We then screened multinary compositions that contain Gd and Ce. Results from this more focused high-throughput screening are presented below. Our initial results from this subtask were the identification of 12 materials from our computational screening to be experimentally tested at SNL and CU (**Table 2**).

Table 2: Screened materials identified for experimental testing at SNL and CU.

Formula	**O-Vac Enthalpy (eV)**	**Electron Effective Mass m_e^***	**Testing Location**
Ba_2CeSnO_6	4.382 - 4.382	19.233	SNL
$BaSrCeVO_6$	4.397 - 4.553	17.799	SNL
Sr_2CeTiO_6	5.045 - 5.045	19.501	SNL
$BaSrCeSnO_6$	4.345 - 4.450	18.048	SNL
$BaSrCeWO_6$	5.297 - 5.376	17.563	SNL

$BaSrCe_2O_6$	5.041 - 5.109	22.197	CU
Ba_2CeHfO_6	5.326 - 5.326	19.508	CU
$BaSrCeHfO_6$	5.335 - 5.335	18.883	CU
$BaCaCeHfO_6$	3.321 - 5.657	16.769	CU
Sr_2CeHfO_6	5.750 - 5.750	15.92	CU
Sr_2CeSnO_6	4.330 - 4.330	16.193	CU
$CaGdMgSbO_6$	2.705 - 2.738	23.617	CU

We generated 223 experimentally observed ternary perovskite compositions (incorporating proper A- and B-site assignments) to benchmark the ability of the Structure Prediction and Diagnostic Software (SPuDS) program to create accurate starting structures for DFT property prediction. SPuDS is based on the Bond Valence Model and we added O-O anion parameters to the BVM parameters used for SPuDS, which does not generally use anion-anion interactions, but which we found is important for accurate predictions with BVM. 25 of the compositions were predicted to be cubic perovskites by SPuDS, resulting in a final dataset of 198 compositions in all 11 Glazer tilting systems. The ionic and electronic degrees of freedom of the structures predicted by SPuDS were relaxed using DFT (SPuDS-DFT), and the starting and final structures were compared using the normed structural fingerprint distance (SFPD), which quantifies the degree of similarity between two structures. SFPD = 0 indicates two identical structures, whereas an SFPD > 0.9 indicates highly dissimilar structures (i.e., structures with significantly different coordination environments). For context, the SFPD between the Pnma and Pm-3m $LaTiO_3$ perovskite polymorphs is 2.02, as these two structures have different A- and B-site coordination environments. Across the full dataset SPuDS and SPuDS-DFT structures tend to be very similar, with a mean SFPD of 0.489 with ~86% < 0.9, indicating the percentage of very similar structures. When only considering the *DFT predicted ground states structures* for each composition, the mean SFPD = 0.374 with ~97% < 0.9, indicating that our scheme SPuDS-DFT scheme accurately predicts DFT structures.

DFT relaxations of the benchmarking dataset were performed with Materials Project-compatible parameters, enabling the decomposition enthalpies of the ground states to be computed relative to competing phases in the Materials Project. Ground state polymorphs with decomposition enthalpies < 0 eV/atom are predicted to be s relative to Materials Project competing phases, while polymorphs with decomposition enthalpies between 0 meV/atom and ~100 meV/atom are typically considered metastable such that they might become stable when temperature effects are explicitly included. Notably, some of the experimental perovskites in our dataset constitute phases that are only observed or synthesized at high temperatures or pressures. One example is $MgSiO_3$, which is unstable relative to its competing phases (decomposition enthalpy of 216 meV/atom) under standard temperatures and pressures although it has been observed in the Earth's mantle. 0 K DFT calculations do not explicitly account for these pressure and temperature effects, and therefore the experimental synthesizability of these phases could be incorrectly predicted. We therefore also compared the 0 K ground state polymorph energies predicted in our dataset to the 0 K energies of the ground state polymorph energies tabulated in the Materials Project.

Of the 198 ground state polymorphs in our dataset, 172 of these structures were tabulated in the Materials Project with computed formation energies. The comparison between computed formation energies is shown in **Figure 24**. The two noticeable outliers are the ground state polymorphs for the $GdFeO_3$ and $EuScO_3$. The ground state formation energies for these compositions are predicted to be significantly lower in our benchmarking dataset (by 1,650 meV/atom and 800 meV/atom, respectively) than in the Materials Project, suggesting some inaccuracy in the DFT results for tabulated in Materials Project. Neglecting these outliers, the root mean squared error between the SPuDS-DFT ground state formation energies and the MP tabulated formation energies is 49 meV/atom, within the acceptable DFT error range for oxides. This confirms that SPuDS structures relaxed using DFT are comparable in both geometry and final energy to existing structures in the Materials Project database.

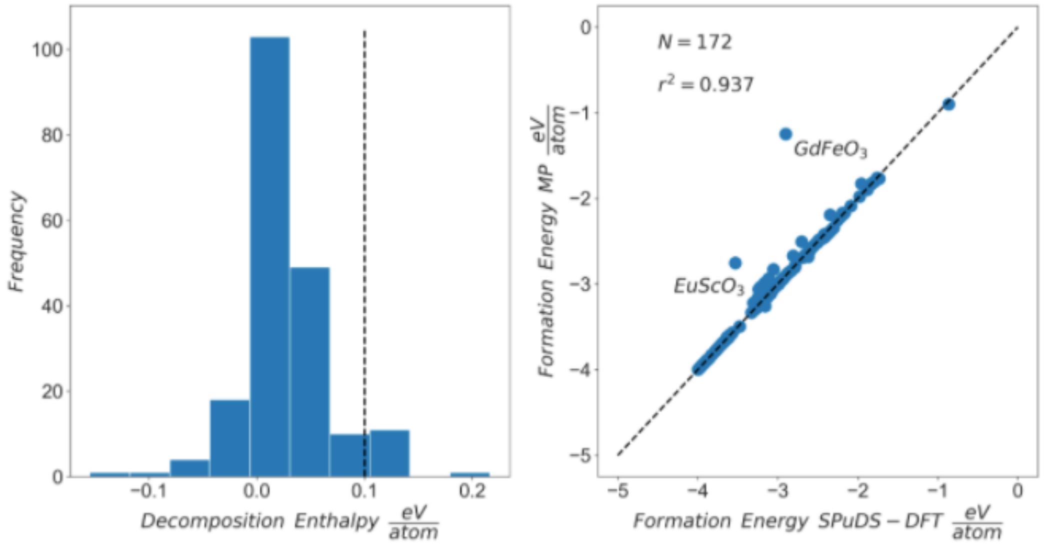

Figure 24: a) Distribution of decomposition enthalpies for ground state perovskites in our dataset. The black line depicts a decomposition enthalpy value of 100 meV/atom. b) SPuDS-DFT formation energies vs. tabulated Materials Project formation energies. The outlying compositions ($GdFeO_3$ and $EuScO_3$) have formation energies that are underpredicted by the Materials Project.

As depicted in **Figure 25**, the majority (~90%) of ground state ternary perovskite oxides identified using our SPuDS-DFT scheme originated from the Glazer tilt #10 polymorph, or Pnma, geometry. This aligns with experiment, where Pnma is the most frequently observed geometry amongst the ternary perovskite oxides. This result suggests that for theoretical studies involving ternary perovskite oxides, and likely for more complex $A_2BB'O_6$ and $AA'BB'O_6$ perovskites, the SPuDS-DFT Pnma structure is often the best approximation to the DFT-predicted ground state formation energy. As shown in **Figure 25b**, accurate ground state identification is integral in predicting the STCH-relevant electronic properties (i.e., band gap) of a material. **Figure 25b** shows the distribution of normalized band gaps (i.e., the band gap of each polymorph in a compound divided by the maximum band gap for polymorphs in that compound) for the 11 Glazer tilt systems. Pnma results in the largest normalized band gap, whereas Pm-3m (cubic symmetry) results in the smallest. This suggests that using the cubic perovskite structure to estimate stability and electronic properties, which is commonly done in high-throughput, computational studies of theoretical materials, is both an improper approach to estimating stability because tilting isn't explicitly included, which can lead to severe underestimates of the band gap of the DFT predicted ground state.

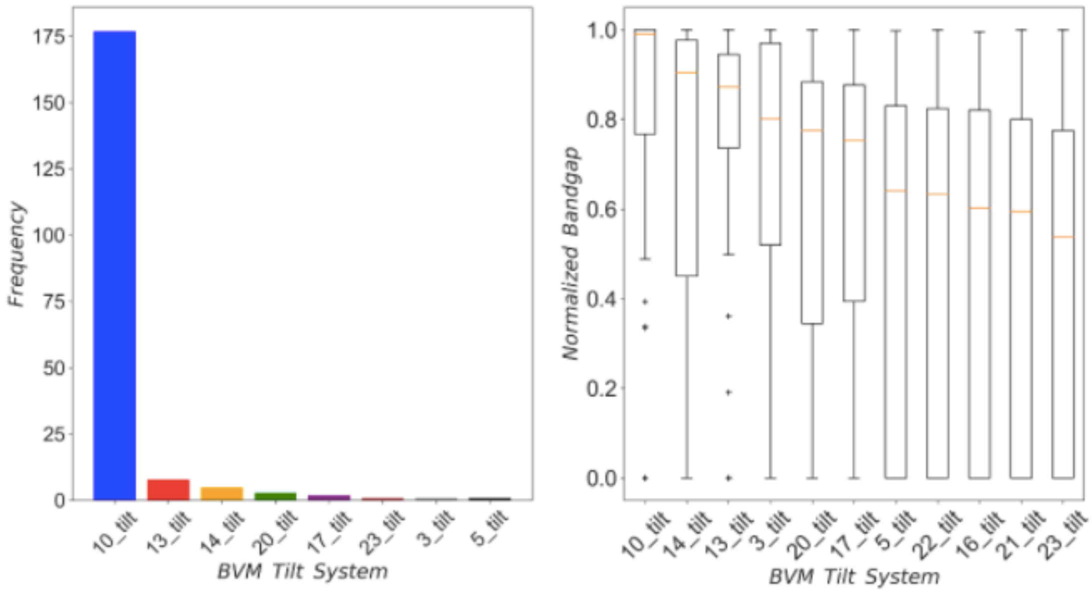

Figure 25: a) Distribution of SPuDS-DFT predicted ground states by starting Glazer tilt system. b) Box plot of normalized band gaps by starting Glazer tilt system. The largest normalized band gaps are observed in Glazer tilt #10 (10_tilt; Pnma), whereas the smallest are observed in 23_tilt (Pm-3m).

Correlation between BVM GII and DFT Energy:

We previously discussed BVM's unique ability to reliably predict perovskite oxide structures optimized using DFT. BVM's predictive ability can be attributed to the relationship between DFT energy and the global stability index (GII). GII quantifies the deviation of cation coordination environments in a crystal from ideal coordination environments predicted by the cation/anion pair bond valence parameters; larger GII values are therefore associated with greater structural "instability." Previous investigations of perovskite oxides have established the correlation between the GII and DFT energy, albeit for a small, select sets of experimental perovskite compositions with certain constraints (i.e., only varying the lattice parameter in the cubic geometry). Our study is much larger and comprehensive and aimed at supporting the potential use of BVM/GII for accelerated and reliable screening of massive perovskite spaces for water splitting where not only are large numbers of compositions considered, but redox materials are analyzed with their relevant crystal structures.

Our perovskite investigation is the first to examine this relationship for both experimental and theoretical perovskite oxide compositions across the 22 competing Glazer tilt systems (polymorphs). For our dataset of ternary perovskite oxides, we've quantified the relationship between the GII and DFT energy by computing the Pearson correlation coefficient, p, between GII and DFT formation energy (ΔH_f) for polymorphs of a given composition. Of the 200 experimental and 116 theoretical ternary perovskite oxide compositions considered, 164 (82%) and 104 (90%) of compositions exhibit $p > 0.7$, which by convention indicates a strong, linear correlation.

As shown in **Figure 26**, the relationship between GII and ΔH_f for the experimental perovskite $LaTiO_3$ correctly identifies the orthorhombic polymorph (blue) as the ground state and the cubic polymorph (red) as highly unstable, and exhibits a linear relationship with ΔH_f for the remaining metastable polymorphs (orange). GII can therefore be used to estimate DFT energy, with the potential to bypass many DFT calculations in high-throughput schemes and still identify the correct perovskite polymorph ground state. Our high-throughput investigations into double ($A_2BB'O_6$) and multinary ($AA'BB'O_6$) perovskite oxides leveraged this relationship to more rapidly identify potential STCH candidates.

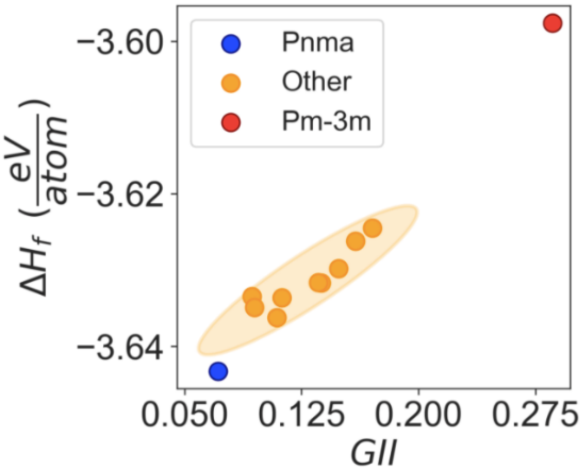

Figure 26*:* Linear correlation between GII and relative polymorph energies for $LaTiO_3$. Note that most computational studies assume the high symmetry cubic (Pm-3m) polymorph, although it is highly unstable, as correctly predicted using GII.

Effects of Magnetism on DFT Energy:

Bulk magnetism (spin state) can have a non-negligible effect on the properties, including the electronic characteristics and DFT energies, which are critical to the water splitting abilities of perovskite oxides; this is especially pertinent in systems with magnetic elements on both the A and B sites (such as $GdVO_3$). However, many previous high-throughput studies have neglected to consider initial magnetization explicitly; these studies assumed that the easily computed high-spin ferromagnetic state is sufficient to capture ground state DFT properties. Our results prove that this assumption to be incautious at best, as it demonstrates the substantial variability in DFT energy caused by magnetism for 10 competing polymorphs of $GdVO_3$. Consequently, ignoring the specific spin state of the material in both its perfect and defective structures will generally lead to inaccurate predictions that will mislead computational predictions of materials properties.

In the example of $GdVO_3$, single-point calculations were performed for one ferromagnetic and nine unique antiferromagnetic spin initializations (high-spin with random spin orientations). Because no geometry optimization occurs in single-point calculations, differences in DFT energy are attributed to electronic effects caused by the initial magnetic moment(s) (final magnetic state/moment, electron density re-distribution) rather than ionic effects (species position, unit cell size). For all 10 $GdVO_3$ polymorphs, magnetic sampling identifies a lower DFT energy than the high-spin ferromagnetic initialization typically used in other computational studies. This indicates that spin sampling is required to accurately predict the right state of the system, although this can be performed as single-point calculations at atomic structures optimized in the high-spin ferromagnetic state.

The average difference between the high-spin ferromagnetic energy and the minimum energy found with magnetic sampling is 76 meV/atom, with a maximum difference of 132 meV/atom. Notably, while magnetic sampling improves the energy predictions for all systems, the change in energy is not entirely systematic (e.g., marginal improvements in energy prediction for the P4/mbm polymorph). This suggests that initial magnetism warrants consideration not only to determine perovskite formability relative to formation of its decomposition products but also the ***relative*** stability of competing polymorphs.

Magnetic sampling not only significantly improves DFT energy predictions but also the correlation of GII with DFT energy. The Pearson correlation coefficient, p, between GII and DFT energy improves from $p = 0.792$ to $p = 0.935$ when magnetism is explicitly incorporated. This further reinforces our conclusion that BVM is an attractive method for DFT structure and energy predictions, as GII better reproduces DFT energy predictions conducted with the PBE exchange correlation functional when the effects of magnetic spin state initialization are more rigorously considered. For these reasons, magnetic sampling was performed for all high-throughput perovskite calculations.

In **Subtask 2.1** we showed that the Pnma (orthorhombic) distortion provides a good initial estimate for the ground state stability and band gap. Thus, our initial screening for stable multinary perovskite oxides started with the Pnma structure rather than the Pm-3m (cubic) structure, in contrast to the traditional approach. Furthermore, we showed that magnetic sampling is necessary to correctly determine the relative stability and accurately predict the electronic structure properties of perovskite polymorphs. We performed high-throughput screening using mostly the BVM-predicted cubic polymorphs. In contrast, later performed the high-throughput screening of 20,766 multinary compositions in the a-b+a- glazer mode, which is the glazer mode of the Pnma orthorhombic distortion for single perovskite compounds.

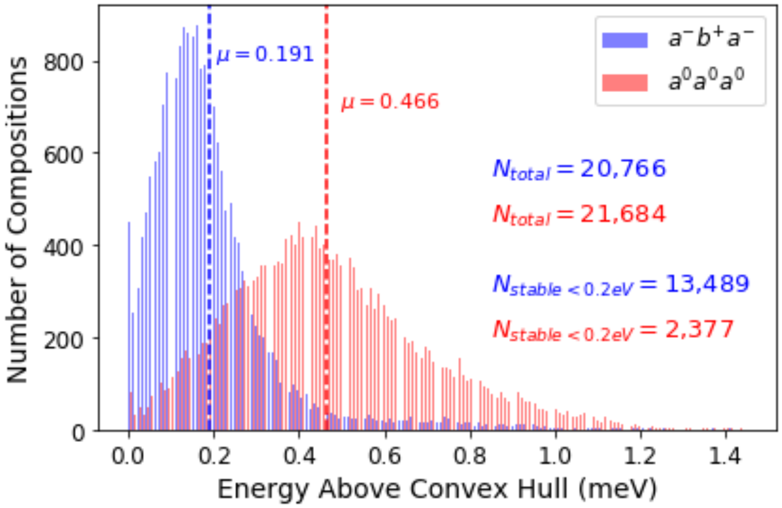

Figure 27: High-throughput multinary perovskite stability comparison between the non-tilted cubic a0a0a0 structures (red) and the tilted a-b+a- distortions (blue). This shows that analyzing candidate materials in the orthorhombic symmetry greatly improves the prediction of stability and shows that the most commonly used approach of assuming cubic symmetry leads to inaccurate predictions and likely a considerable number of false negatives.

The a-b+a- tilt (μ = 0.191 eV) is generally stabilized relative to the cubic polymorphs (μ = 0.466 eV), and as such, we identify significantly more stable compounds that lie within 0.2 eV of the convex hull for the a-b+a- tilt (13,489 compounds) compared to the cubic assumed structure (2,377 compounds). This agrees with the results from the ternary screening and further emphasizes the need to include distortions in the screening; screening by cubic alone, which is traditionally reported in the literature, misses a large number of stable candidate materials.

The next step in our workflow after screening for stability, is to screen based on oxygen vacancy formation energy and the m_e^* of electrons. This screening procedure involves: 1) magnetic sampling of stable candidate materials, 2) relaxing structures with symmetry off to allow for local distortions, 3) sampling symmetrically unique oxygen vacancy sites, and 4) calculating the DOS m_e^* at 1000 K of each host structure. We then chose to focus our study on Mn containing compounds as they have proven promising in previous studies. In our database, ~400* Mn containing compounds lie within 100 meV of the convex hull (*this number is dynamic as calculations continue to converge), and we have completed the workflow for 312 of these compounds), indicating that they are stable or at most moderately metastable relative to their decomposition products (See **Figure 27**).

Numerous compounds possess oxygen vacancy formation energies within the liberal STCH range of 1-5 eV, and a few compounds also posses large m^*_e, indicating that vacancy formation is aided by a large electronic entropy contribution. We narrowed the number of candidate materials using the following criteria: 1) oxygen vacancy energy must be < 4.6 eV, 2) band gap must be > 0.8 eV, and 3) m^*_e must be > 8. This analysis identified a few candidates with larger m^*_e and smaller oxygen vacancy energy relative to CeO_2, indicating that they are promising water splitting candidates. Furthermore, we identified Ca_2TiMnO_6 from this screening which was recently demonstrated by Wolverton and Haile as one of the best STCH materials to date with activity similar to $FeAl_2O_4$. We plan to forward these materials to experimental nodes at Sandia (Coker and McDaniel) and our internal experimental collaborator (Weimer) to perform high-temperature XRD, and redox cycling to test their H_2 generation abilities. However, before suggesting any of the compounds for experimental study, we first performed a sampling of the polymorphs to ensure our calculations are for the true ground state for each composition.

We compiled the 312 materials to identify promising candidates to be sent for experimental testing at CU and Sandia. We screened these compounds in two ways: **A)** 1) minimum oxygen vacancy must be > 2.0 eV, 2) maximum oxygen vacancy energy must be < 5.1 eV, 3) band gap must be > 0.9 and < 3.0 eV, and 3) m^*_e must be > 6; and **B)** 1) stability relative to the convex hull (E_{Hull}) must be < 50 meV/atom, 2) band gap must be > 0.0 eV, and 3) mean oxygen vacancy energy must be > 2.0 and < 5.0 eV. Screening by methods **A** and **B** produced two lists of 42 and 69 candidate materials, respectively. To further narrow the candidates to a more tractable number for synthesis and experimental characterization, we cross-referenced lists **A** and **B** to identify the top candidates in both lists, and we searched the Materials Project database for candidates with corresponding ICSD numbers (i.e. materials that have been successfully synthesized). We identified 8 materials with ICSD numbers, 6 of which are possibly water splitting candidates. One of the compounds, namely In_2MnNiO_6, was synthesized at high P and we calculate E_{Hull} = 56.5 meV/atom above the convex hull, thus validating our choice of stability cutoff used in **B**.

Using the methods described above, we were able to narrow the candidate list to 16 promising materials that span a range of stabilities, vacancy energies, and electron m_e^*. 8 of 16 materials were forwarded to Sandia (Coker and McDaniel) and 8 of 16 were sent to our internal experimental collaborator (Weimer) to perform high-temperature XRD, and redox cycling to test their H_2 generation abilities (**Table 3**).

Table 3: List of 16 materials sent for experimental testing (See **Figure 28** for O_{vac} screening data).

Sandia		CU	
Order	Compound	Order	Compound
1	$KYMnWO_6$	1	La_2MnNiO_6
2	$CaCeMnYO_6$	2	Y_2CoMnO_6
3	$CeSrMnYO_6$	3	$CaZrMgMnO_6$
4	$BiNdMnVO_6$	4	$CaHfMnNiO_6$
5	Bi_2MnVO_6	5	$CaHfMgMnO_6$
6	$CaZrMnVO_6$	6	Nd_2MnNiO_6
7	$ZrYLiMnO_6$	7	Bi_2MnNiO_6
8	$TbKMnWO_6$	8	$CaCeGdMnO_6$

We previously narrowed the lasted candidate list to 16 promising materials that span a range of stabilities, oxygen vacancy energies, and electron m_e^*. 8 of these 16 materials were forwarded to Sandia (Coker and McDaniel) and the other 8 of 16 were sent to our internal experimental collaborator (Weimer) to perform high-temperature XRD, and redox cycling to test their H_2 generation abilities (**Table 3**). 2 of 8 materials sent from CU were determined to split water experimentally.

At that time, 9 water splitting materials have been discovered using our computational screening workflow. Ca_2TiMnO_6 was identified independently by our screening procedure and was previously shown in the literature to split water. The remaining 8 of 9 materials were demonstrated to split water at CU ($SrGdAlMnO_6$, La_2MnNiO_6, Nd_2MnNiO_6, $BaSrCe_2O_6$, Ba_2CeHfO_6, $BaSrCeHfO_6$, $BaCaCeHfO_6$, and Sr_2CeHfO_6) or at Sandia ($GdLaCoFeO_6$).

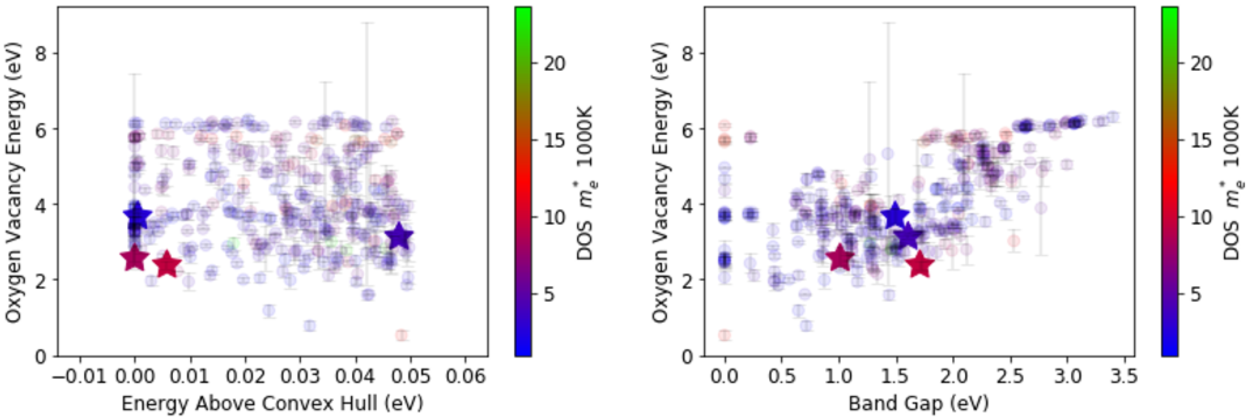

Figure 28: Multinary perovskite manganate screening. The stars indicate discovered water splitting materials (Ca_2TiMnO_6, $GdLaCoFeO_6$, La_2MnNiO_6, and Nd_2MnNiO_6) predicted with our computational workflow.

The discovered water splitting materials are stable ($E_{hull} < 50$ meV/atom) and possess band gaps between 1.0-2.5 eV, average oxygen vacancy formation energies between 2.0-4.0 eV, and 1000 K DOS $m^*_e > 2.0$. 122 candidate materials in our multinary database with properties that fall within the above cutoffs, however, only 4 of these materials have large m_e^* with $m^*_e > 15$, namely: $CeSmLiMnO_6$, $CeNdLiMnO_6$, $CeNdMnNaO_6$, and $CeSmMnNaO_6$.

We previously identified the composition $GdLaCoFeO_6$ (GLCF) as a potential perovskite oxide using the machine-learned descriptor tau. To computationally evaluate the stability of the GLCF perovskite relative to its competing phases, e.g., Gd_2CoO_3, $LaFeO_3$, etc., the total energy of the GLCF perovskite (with the triclinic crystal symmetry and ordered A and B sites) was computed using DFT. The GLCF perovskite exhibits an energy above the convex hull, E_{hull}, of 6.8 meV/atom, which suggests that the GLCF perovskite phase is thermally accessible under experimental synthesis conditions. Similarly, the perovskite oxide La_2CoFeO_6 (L2CF), which represents known La-Co-Fe-O thermochemically-active perovskite oxide redox mediators such as $La_{0.6}Sr_{0.4}Co_{0.2}Fe_{0.8}O_3$ and $LaFe_{0.75}Co_{0.25}O_3$, is on the convex hull (E_{hull} = 0 meV/atom). The oxygen vacancy enthalpies, ΔH_{Ovac}, of L2CF and GLCF were therefore evaluated using DFT to predict the STCH relevant thermal reduction enthalpies, ΔH_{TR}, of these materials. ΔH_{Ovac} of Gd_2CoFeO_6 (G2CF) was also evaluated.

The distributions of ΔH_{Ovac} computed using DFT for the symmetrically unique sites of L2CF, GLCF, and G2CF are shown in **Figure 29**. The ΔH_{Ovac} distribution of GLCF is bounded by the ΔH_{Ovac} distributions of L2CF (lower bound) and G2CF (upper bound). Herein, we report the mean oxygen vacancy enthalpy, $\overline{\Delta H}_{Ovac}$, of CeO_2 ($\overline{\Delta H}_{Ovac}$= 3.95 eV/atom) computed at the same DFT level of theory as the upper bound for the STCH active range. We use a liberal lower bound of 2 eV/atom to account for uncertainty in DFT energetics, which approaches the computed $\overline{\Delta H}_{Ovac}$ of the $SrGdMnAlO_6$ redox mediator reported in Q15 ($\overline{\Delta H}_{Ovac}$ = 1.95 eV/atom). Materials approaching the minimum ΔH_{Ovac} for STCH activity exhibit slow oxidation kinetics and/or degradation during redox cycling, whereas materials approaching the maximum ΔH_{Ovac} for STCH activity suffer from reduced H_2 capacity. GLCF exhibits both O vacancies with low and high ΔH_{Ovac}, where vacancies with low ΔH_{Ovac} participate in H_2 production and those with high ΔH_{Ovac} are less likely to form under STCH operating conditions and their absence can therefore preserve the perovskite lattice during redox cycling. This ΔH_{Ovac} distribution predicts enhanced cyclability of GLCF relative to L2CF and increased H_2 production capacity relative to G2CF.

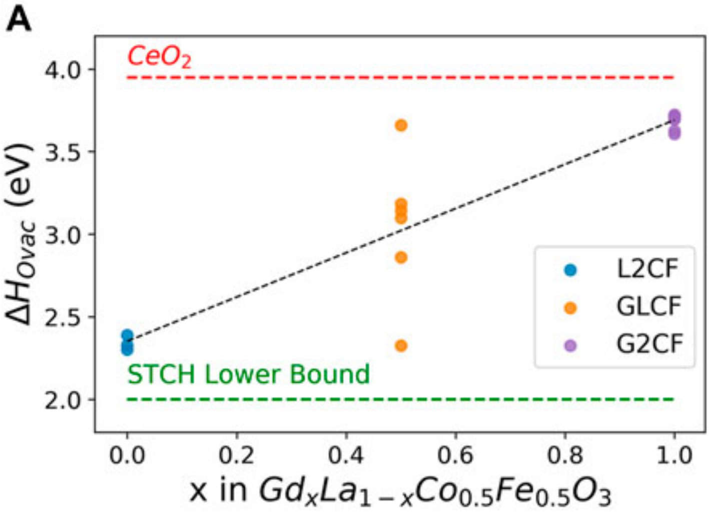

Figure 29: Computed ΔH_{Ovac} values vs. Gd fraction (x) in $Gd_xLa_{1-x}Co_{0.5}Fe_{0.5}O_3$ compositions. Higher concentration of Gd (x) increases ΔH_{Ovac} and therefore the stability of the perovskite oxide. L2CF, GLCF and G2CF exhibit mean oxygen vacancy enthalpies, $\overline{\Delta H}_{Ovac}$, within the estimated STCH active range (2.0 eV ≤ $\overline{\Delta H}_{Ovac}$ ≤ 3.95 eV).

We previously identified the composition $GdLaMnNiO_6$ (GLMN) as a potential perovskite oxide using the machine-learned descriptor tau. To computationally evaluate the stability of the GLMN perovskite relative to its competing phases, e.g., Gd_2MnO_3, $LaNiO_3$, etc., the total energy of the GLMN perovskite (with the monoclinic crystal symmetry and ordered A and B sites) was computed using DFT and compared to competing phases tabulated in the Materials Project Database. The GLMN perovskite exhibits an energy above the convex hull, E_{hull}, of 59 meV/atom, which suggests that the GLMN perovskite phase is thermally accessible when synthesized at moderate to high temperatures. The known perovskite oxide La_2MnNiO_6 (L2MN) possesses a similar E_{hull} of 48 meV/atom, and was also predicted to split water. The oxygen vacancy formation enthalpies, ΔH_{Ovac}, of GLMN and L2MN were evaluated using DFT to predict the STCH relevant thermal reduction enthalpies, ΔH_{TR}, of these materials. The ΔH_{Ovac} of the theoretical mixed lanthanide-transition metal perovskite Gd_2MnNiO_6 (G2MN) was also evaluated.

The distributions of ΔH_{Ovac} computed using DFT for the symmetrically unique sites of L2MN, GLMN and G2MN are shown in **Figure 29**.

The ΔH_{Ovac} distribution of GLMN is bounded by the ΔH_{Ovac} distributions of L2MN (lower bound) and G2MN (upper bound). Herein, we report the mean oxygen vacancy enthalpy, $\overline{\Delta \mathrm{H}}_{Ovac}$, of CeO_2 ($\overline{\Delta \mathrm{H}}_{Ovac}$= 3.95 eV/atom) computed at the same DFT level of theory as the upper bound for the STCH active range. We use a liberal lower bound of 2 eV/atom to account for uncertainty in DFT energetics, which approaches the computed $\overline{\Delta \mathrm{H}}_{Ovac}$ of the $SrGdMnAlO_6$ redox mediator reported in Q15 ($\overline{\Delta \mathrm{H}}_{Ovac}$ = 1.95 eV/atom). Materials approaching the minimum ΔH_{Ovac} for STCH activity exhibit slow oxidation kinetics and/or degradation during redox cycling, whereas materials approaching the maximum ΔH_{Ovac} for STCH activity suffer from reduced H_2 capacity. GLMN exhibits both O vacancies with low and high ΔH_{Ovac}. However, the mean vacancy enthalpy computed for GLMN (3.33 eV/atom) is greater than that of the $GdLaCoFeO_6$ (GLCF) redox material reported in Q16, which suggests that this material possesses a larger thermodynamic driving force for thermal reduction i.e., water splitting.

Thermodynamic analysis by Muhich et al. and others showed that viable STCH redox materials must satisfy the following STCH Gibbs free energy inequalities:

$$\Delta H_{cycle} = \Delta H_{TR} + \Delta H_{WS} \geq 286 \text{ kJ/mol}$$

$$\Delta S_{cycle} = \Delta S_{TR} + \Delta S_{WS} \geq 44.4 \text{ J/mol·K}$$

Ideal STCH redox mediators possess a reduction enthalpy, ΔH_{TR}, large enough to reduce steam, but not so large that excessively high temperatures are required to reduce the mediator. In contrast, maximizing the reduction entropy, ΔS_{TR}, benefits both requirements, as large ΔS_{TR} decreases the free energy of reduction (ΔG_{TR}) at a given temperature and therefore lowers the temperature necessary to reduce a material with a given ΔH_{TR}. Recent investigations of STCH active materials have characterized contributions to ΔS_{TR}. For instance, Naghavi et al. showed that the state-of-the-art STCH redox material CeO_2 exhibits a "giant", positive onsite electronic entropy of reduction, $\Delta S_{TR,elec}$, in addition to configurational and vibrational entropies associated with oxygen vacancy formation. Ceria's large $\Delta S_{TR,elec}$ arises from the multiplicity of unoccupied Ce f-orbital states that lie near the conduction band minimum (CBM), which become thermally accessible relative to the Fermi level of CeO_2 at STCH reduction temperatures. This insight led to the identification of $CeTi_2O_6$ as a STCH active redox material following a computational investigation of Ce-containing oxides by Wolverton et al.

More generally, Lany et al. showed that the formation of charged oxygen vacancy defects under STCH reduction conditions results in large $\Delta S_{TR,elec}$ if a material possesses a large DOS electron

m_e^* near the CBM. $m*_e$ quantifies the multiplicity of states in a manner that is not Ce f-orbital specific, meaning that the contributions to the multiplicity of states from other elements are also considered. Larger $m*_e$ corresponds with larger $\Delta S_{TR,elec}$, and can be rapidly and accurately characterized using first-principles electronic structure calculations such as Density Functional Theory (DFT). Oftentimes, the evaluation of $\Delta S_{TR,elec}$ incurs no additional computational expense relative to first-principles bulk stability screening, which is typically performed in computational studies of theoretical perovskite oxides prior to experimental STCH characterization to assess the likelihood that a metal oxide composition is synthesizable and phase stable as a perovskite. In this manner, the evaluation of $m*_e$ and $\Delta S_{TR,elec}$ can be efficiently integrated into high-throughput computational frameworks for STCH candidate discovery.

Perovskite oxides that possess large $m*_e$ should by extension exhibit larger $\Delta S_{TR,elec}$

relative to perovskite oxides with smaller $m*_e$. Previous studies have shown that certain cation species (e.g., Ce^{4+}) contribute large numbers of electronic states to the DOS near the CBM of metal oxides, which can result in large $m*_e$. To quantify contributions to $m*_e$ on a cation-by-cation basis, we evaluated the $m*_e$ of all available metal oxides, including non-perovskites, tabulated in the Materials Project (MP) database. The MP currently contains the DFT-computed structures and energies of >140,000 inorganic materials with ~70,000 of these entries being metal oxides. Of these, ~24,000 metal oxides possess tabulated electronic structure information from which $m*_e$ can be computed. To make the following analysis cation specific, we assigned oxidation states to elements present in the MP-tabulated perovskite oxides using the pymatgen python package's oxidation state assignment algorithm. In this manner, we identified the cations that produce the largest $m*_e$ amongst the cations present in MP entries with tabulated DOS.

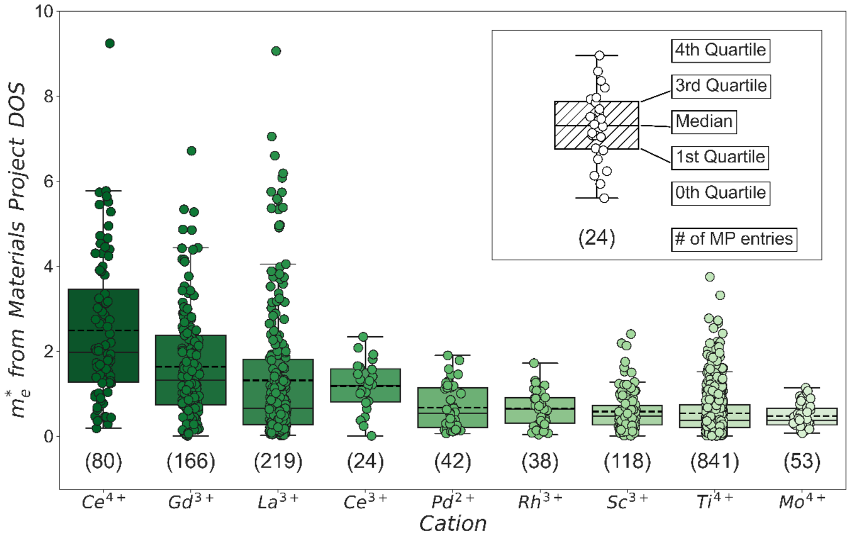

Figure 30: Distributions of electron $m*_e$ for the nine cations present in Materials Project tabulated oxides that, on average, have the largest $m*_e$. Only the cations present in at least 20 MP entries with tabulated DOS are shown. Cations are ordered by their mean $m*_e$ (black dashed line) from left to right. MP entries containing the cations Ce^{4+}, Gd^{3+}, La^{3+} and Ce^{3+} are predicted to have the largest average $m*_e$s ($m*_e$ = 2.485, 1.633, 1.313, and 1.180, respectively). Numbers in parentheses below the box plots denote the number of entries evaluated that contain the associated cation.

Figure 30 plots the distributions of effective m^*_e for the 23,723 MP metal oxides with tabulated DOS. The horizontal axis shows the nine cations present in at least 20 MP entries with tabulated DOS that have the largest mean m^*_e. Notably, Ce^{4+} is rediscovered as the cation that, on average, contributes the largest density of accessible electronic states near the CBM at 1000 K, followed by the lanthanide cations Gd^{3+}, La^{3+}, and Ce^{3+} in decreasing order. MP entries containing these four cations are computed to possess larger average m^*_e than MP entries containing the 86 other cations considered, which suggests that one or more of these cations should be included in STCH metal oxide candidate compositions to increase ΔS_{TR}. This analysis identifies the cations that, on average, result in the largest m^*_e, but does not quantify changes in the m^*_e if one cation is substituted for another. Additionally, the data analyzed constitutes all metal oxide entries tabulated by the MP, as opposed to specifically evaluating the perovskite oxide structures. This suggests that Gd^{3+} substitution in metal oxide compositions could increase ΔS_{TR} regardless of geometry. However, as this investigation is focused on perovskites, we leveraged our ABO_3 perovskite dataset to isolate contributions to the m^*_e attributable to single cation substitutions in perovskite oxides. Our dataset consists of 657 single perovskite oxide compositions generated in up to six unique perovskite geometries as denoted by their Glazer tilt notation.

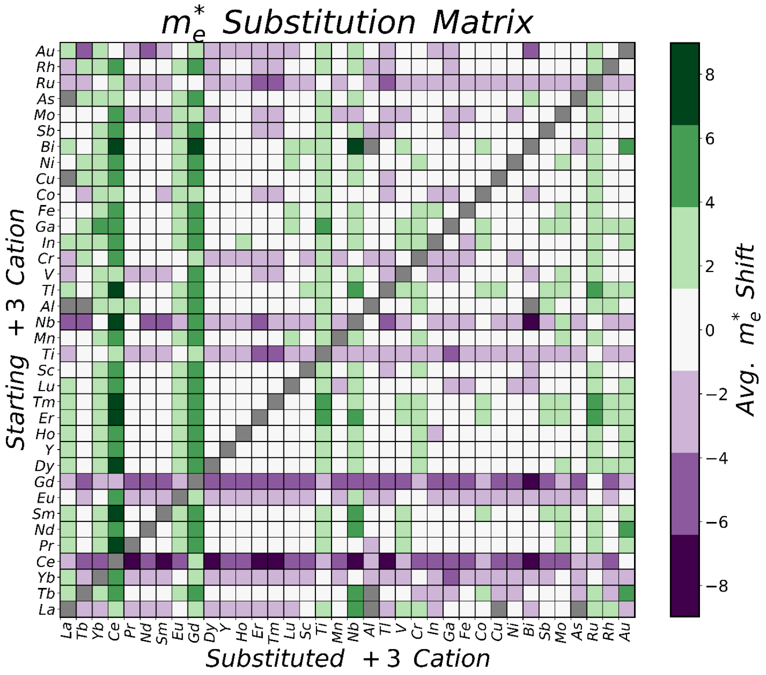

Figure 31: Substitution matrix showing the average shift in the m^*_e upon substitution of the starting *A*-site cation (vertical axis) with a substituted cation (horizontal axis) for the 657 ABO_3 perovskite oxides in our database. Green indicates an increase in m^*_e following substitution, whereas purple indicates a decrease in m^*_e. Cations that cannot be interchanged because the ABO_3 substitution criteria are not satisfied are colored grey. Substitutions of nearly all +3 cations present in our dataset by Ce^{3+} or Gd^{3+} (fourth and ninth columns, respectively) increase m^*_e. On average, Gd^{3+} substitutions for Ce^{3+} increase the m^*_e in the ABO_3 perovskite oxides considered.

Figure 31 displays the average shifts in m^*_e following the replacement of initial +3 cations (vertical axis) with substituted +3 cations (horizontal axis). This matrix shows that, on average, substitution of nearly all +3 cations present in our dataset by Ce^{3+} or Gd^{3+} increases m^*_e. Consistent with the MP analysis described above, substitution of Ce^{3+} by Gd^{3+} also increases m^*_e

on average. Substitutions by La^{3+} generally increase m^*_e when La^{3+} is substituted for other lanthanide +3 cations, e.g., Tb^{3+}, Yb^{3+}, Pr^{3+}, etc. Therefore, our ABO_3 perovskite dataset confirms the trends in m^*_e uncovered in the MP tabulated metal oxides reported in **Figure 31**, which suggests that to maximize m^*_e for STCH applications, perovskite oxides should preferentially include one or more of the +3 lanthanides Ce^{3+}, Gd^{3+} and La^{3+}. Because the Ce- and La-containing compositional spaces possess known STCH redox mediators that have been previously characterized, we examined the largely unexplored Gd-containing compositional space and identified several novel STCH perovskite oxides, including those in the Gd-La-Mn-Ni-O compositional system (L2MN, GLMN and G2MN) and Gd-La-Co-Fe-O compositional system (GLCF).

When oxygen atoms are removed from a metal oxide upon oxygen vacancy formation, the electrons withdrawn from the surrounding metal atoms by the more electronegative oxygens are transferred back to the lattice to occupy electronic states at the Fermi level. All previously reported STCH-active perovskite compositions that reduce via oxygen vacancy formation include at least one redox flexible cation that accepts this electron density.

In all compositions, nearest-neighbor Mn^{4+} and Ni^{2+} cations are reduced when oxygen vacancies form. To investigate the extent of these reductions, we compared the magnetic moments μ_B of the nearest-neighbor Mn and Ni cations in the bulk and oxygen-defect structures. For reference, the Gd and La f-orbital magnetic moments are the same in the host and defect structures, indicating that these cations remain in the +3 oxidation state following reduction. **Figure 32a** shows the average change in the magnetic moments of the Mn and Ni nearest-neighbors to the O vacancy of the host and defect structures, $\Delta\mu_B$. $\Delta\mu_B$ of nearest-neighbor Ni cations *decreases* upon oxygen vacancy formation, consistent with the Ni^{2+} to Ni^{+} transition represented by Ni's octahedral field splitting diagram shown in **Figure 32b**. Furthermore, $\Delta\mu_B$ of the nearest-neighbor Mn cations *increases* upon oxygen vacancy formation, consistent with the octahedral field splitting of the Mn^{4+} to Mn^{3+} transition shown in **Figure 32c**. These results confirm that both Mn^{4+} and Ni^{2+} are partially reduced following vacancy formation and suggest that these cations are redox active in L2MN, GLMN and G2MN.

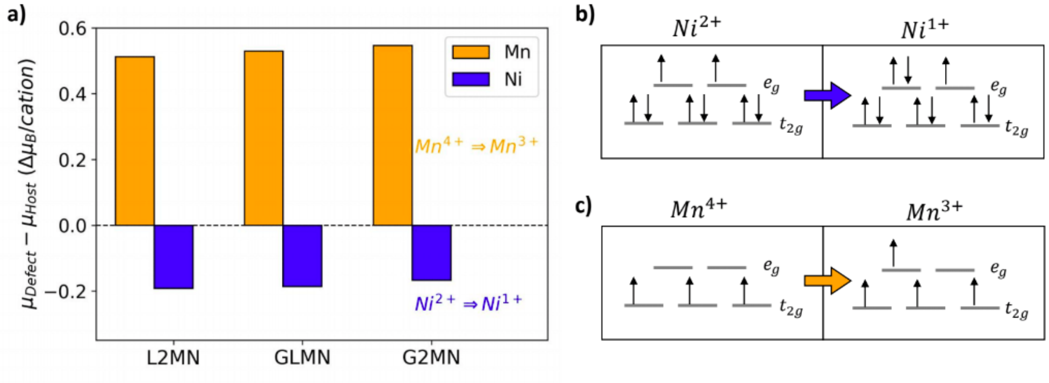

Figure 32: a) Differences in d-orbital magnetic moments for Mn and Ni cation nearest-neighbors to the oxygen vacancies of L2MN, GLMN, and G2MN. On average, the magnetic moments μ_B increase for Mn and decrease for Ni. b) Octahedral field splitting diagrams for high-spin Ni^{2+} and Ni^{+} exhibit a decrease in μ_B upon reduction, in agreement with the DFT predicted magnetism. c) Octahedral field splitting diagrams for high-spin Mn^{4+} and high-spin Mn^{3+} exhibit an increase in μ_B upon reduction, in agreement with the DFT computed magnetism.

At STCH thermal reduction conditions, O vacancies form at the redox mediator surface and diffuse into the bulk material. When steam is introduced into the STCH reactor at oxidizing conditions, these vacancies migrate back to the surface, split water and re-oxidize the material. While the vacancies' thermodynamic driving force to reduce water dictates whether water splitting occurs spontaneously, the ease with which O vacancies diffuse through the bulk dictates the rate at which O vacancies migrate to the surface and thus the rate of hydrogen production. Smaller diffusion barriers correspond with faster redox kinetics, which enables more vacancies to participate in water splitting during a redox cycle and increases total STCH production. DFT has been shown to accurately predict these bulk diffusion barriers. For example, DFT studies of ceria have reported bulk diffusion barriers of between 0.45 eV and 0.60 eV, which generally agree with the experimentally determined range of barriers of 0.53 eV to 0.76 eV.

We computed oxygen vacancy diffusion barriers of 0.78 eV for L2MN, 0.87 eV for GLMN and 0.94 eV for G2MN using the climbing image Nudged Elastic Band (NEB) method as implemented in the Vienna Ab-initio Simulation Program, VASP. These DFT computed diffusion barriers are higher than those previously reported for ceria, and trend inversely with the DFT optimized unit cell volumes, where L2MN has the largest volume (230.41 Å^3) and the smallest transition state barrier. The STCH bulk diffusion kinetics of L2MN, GLMN and G2MN are therefore predicted to be less facile than those of CeO_2, with G2MN being the most kinetically limited of the three materials. These results suggest that substituting Gd^{3+} for the larger radius La^{3+} cation, which causes greater tilting and more asymmetrical distortion of the octahedra as described in Section IB, can inhibit the bulk diffusion of oxygen through the perovskite lattice to the detriment of STCH performance and explains the observation of no water splitting by G2MN by McDaniel, despite the thermodynamic screening indicating that it should be a capable water splitter.

We finalized our high-throughput dataset of mulintary perovskite oxides. In this work, we first generated 69,407 $A_{0.5}A'_{0.5}B_{0.5}B'_{0.5}O_3$ perovskites using a custom HT python wrapper to SPuDS. We report the formation enthalpies (ΔH_f) and decomposition enthalpies (ΔH_d) computed relative to MP-tabulated elemental references and competing phases for the 66,516 structures converged using DFT geometry optimization. We show that SPuDS structures match or are in the same structural family as DFT-optimized structures for 56,716 compositions but differ for 6,808 of the 66,516 converged structures (~10%) that relaxed out of the perovskite phase. We also benchmarked the dataset's DFT energies against the MP database and show that the dataset greatly expands the MP's multinary oxide compositions. The HT SPuDS python wrapper used to generate structures is available on Github and all structures are available as tabulated entries in the MP with the complete metadata available on MPContribs.

Currently, the MP database contains only 3,904 entries composed of the 39 elements considered herein with the chemical formulae $A_{0.5}A'_{0.5}B_{0.5}B'_{0.5}O_3$, $AB_{0.5}B'_{0.5}O_3$, or $A_{0.5}A'_{0.5}BO_3$. We report the structures and energetics of 66,516 multinary oxides, which expands this compositional space by over ten-fold. We anticipate that this dataset will facilitate materials discovery in a space with many current and potential applications, but where DFT calculations were previously sparse. Additionally, and in contrast to other high-throughput perovskite studies that have used template structures or assumed the un-tilted cubic aristotype, we explicitly considered octahedral tilting before DFT optimization. Our investigation into ternary perovskite oxides showed that octahedral tilting typically stabilizes the cubic perovskite phase by more than 100 meV/atom, and by as much as several hundred meV/atom. Thus, explicit consideration of BO_6 tilting should better approximate ground state perovskite energetics, and more reliably predict perovskite phase stabilities and synthesizability. Finally, we include non-perovskite structures in the dataset and report each structure's perovskite/non-perovskite classification in the metadata. This is intended to direct materials scientists towards compositions where the perovskite phase is preserved by DFT optimization so that data scientists can use this designation for machine learning (ML). We are in the process of using ML to mine our database for promising STCH candidates. To our knowledge, high-throughput DFT investigations typically do not confirm nor repudiate phase preservation in their metadata, and this has not been reported for a multinary perovskite oxide dataset of this size. This has posed a significant challenge to the STCH community because we have found that STCH properties are sensitive to the perovskite structure and assuming that the material is in the high symmetry cubic phase leads to incorrect O vacancy energy predictions.

Figure 33a shows the distribution of the ratios of DFT-optimized structure volumes to SPuDS volumes for compositions in our dataset. The mean ratio is 1.05, meaning that SPuDS slightly underpredicts volumes but generally captures multinary perovskite oxide unit cell sizes relative to DFT. Because the SPuDS and DFT volumes are so similar, one might assume that SPuDS structures also accurately estimate multinary perovskite oxide *site positions* relative to DFT. This postulate is further evaluated in a manuscript in preparation, where we show that site positions predicted by SPuDS approximate DFT optimized site positions for ~85% of compositions in our dataset, which can greatly aid in the evaluation of STCH candidates. The Goldschmidt tolerance factor predicts experimental perovskite synthesizability for ternary (ABX_3) compositions from their cation and anion radii. We computed Goldschmidt tolerance factors for *multinary* compositions in our dataset by stoichiometrically averaging their A and B site Shannon ionic radii using:

$$t = \frac{(\frac{r_A + r_{A'}}{2}) + r_O}{\sqrt{2}[(\frac{r_B + r_{B'}}{2}) + r_O]}$$

As shown in **Figure 33b**, ~91% of compositions in the dataset are within the reported range of Goldschmidt tolerance factors expected to form perovskites, $0.825 < t < 1.059$. Finally, Figure 33c shows that all 66,516 compositions in the dataset have negative ΔH_f and are thus stable relative to their elemental reference states. **Figure 33d** shows that for all compositions in the dataset $\Delta H_d <$ 650 meV/atom above the convex hull defined by competing phases in the MP, with a mean ΔH_d of 170 meV/atom.

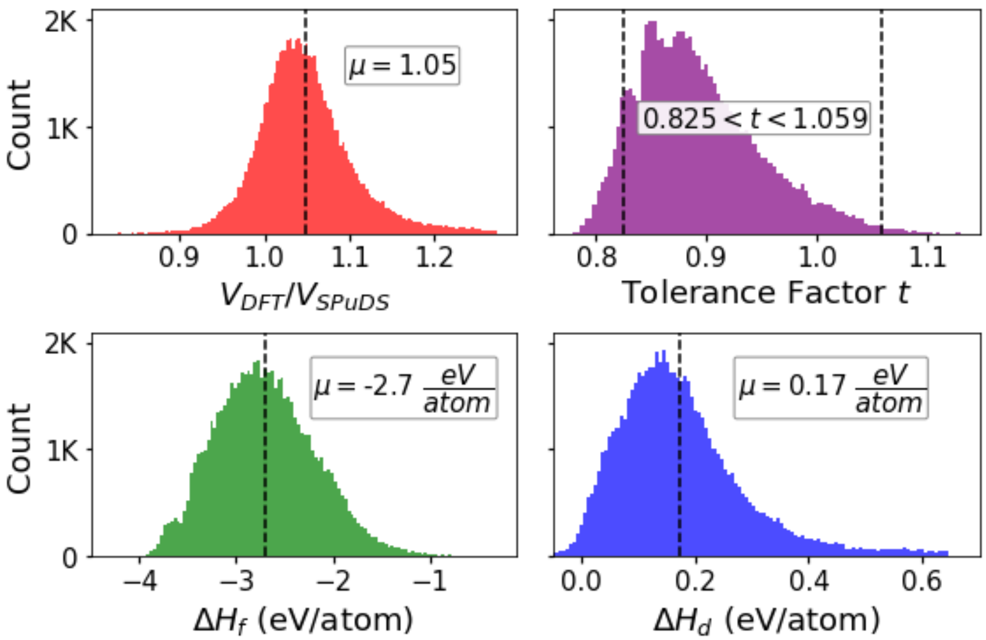

Figure 33: a. Distribution of the ratios of DFT-optimized structure volumes to SPuDS perovskite volumes for the 66,516 compositions in the dataset. b. Distribution of Goldschmidt tolerance factors for compositions in the dataset, computed using Eq. 1. c. Distribution of formation enthalpies (ΔH_f) for compositions in the dataset, computed relative to MP tabulated elemental references. d. Distribution of decomposition enthalpies (ΔH_d) for the dataset, computed relative to MP tabulated competing phases.

All metadata is hosted on MPContribs and can be accessed using the MPContribs API and/or downloaded in JSON or CSV format directly on the host webpage (see **Figure 34**). The tabulated metadata includes: a) identities of elements on the A- and B-sites, b) assigned oxidation states of all elements, c) Goldschmidt and Bartel perovskite tolerance factors, d) formation and decomposition enthalpies computed with respect to MP-tabulated elemental references and competing phases, respectively, e) perovskite/non-perovskite classification, and f) initial SPuDS generated structures. Other relevant properties such as the DFT-relaxed structure and calculation details are available on each materials data page in the main MP repository (https://contribs.materialsproject.org/projects/Multinary_Oxides).

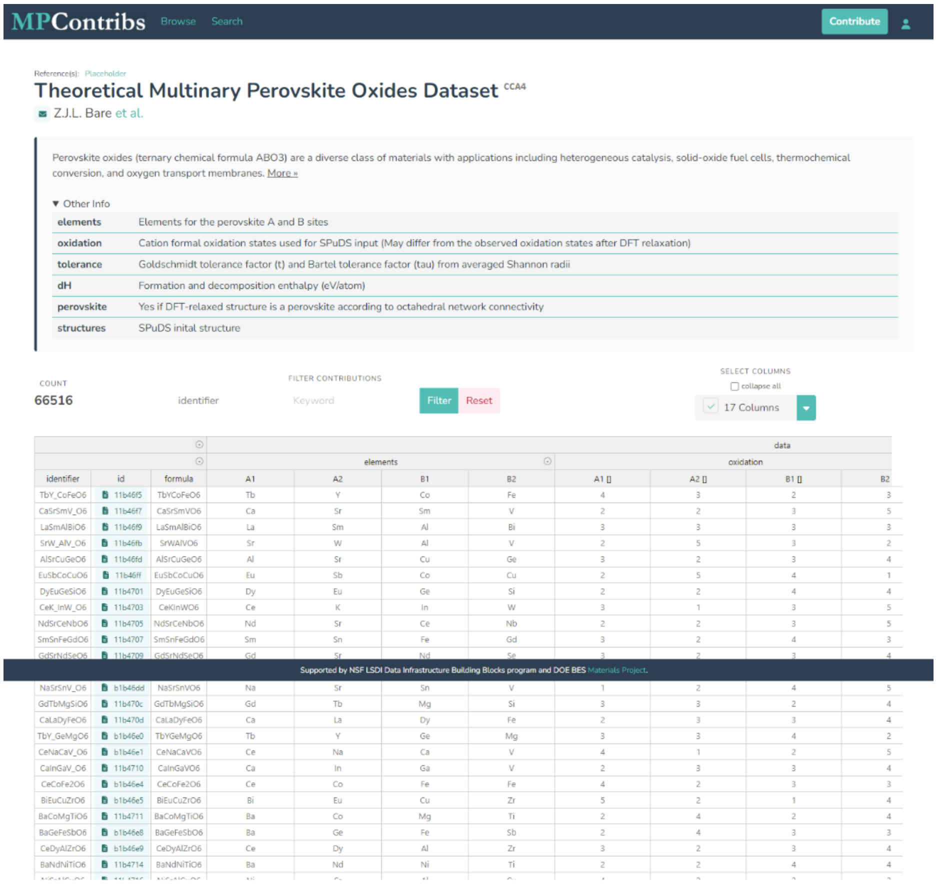

Reference(s): Placeholder

Theoretical Multinary Perovskite Oxides Dataset CCA4

Z.J.L. Bare et al.

Perovskite oxides (ternary chemical formula ABO3) are a diverse class of materials with applications including heterogeneous catalysis, solid-oxide fuel cells, thermochemical conversion, and oxygen transport membranes. More »

▼ Other Info

elements	Elements for the perovskite A and B sites
oxidation	Cation formal oxidation states used for SPuDS input (May differ from the observed oxidation states after DFT relaxation)
tolerance	Goldschmidt tolerance factor (t) and Bartel tolerance factor (tau) from averaged Shannon radii
dH	Formation and decomposition enthalpy (eV/atom)
perovskite	Yes if DFT-relaxed structure is a perovskite according to octahedral network connectivity
structures	SPuDS inital structure

COUNT 66516

identifier

FILTER CONTRIBUTIONS

SELECT COLUMNS

☐ collapse all

☑ 17 Columns

			data							
			elements				oxidation			
identifier	id	formula	A1	A2	B1	B2	A1 []	A2 []	B1 []	B2
TbY_CoFeO6	11b46f5	TbYCoFeO6	Tb	Y	Co	Fe	4	3	2	3
CaSrSmV_O6	11b46f7	CaSrSmVO6	Ca	Sr	Sm	V	2	2	3	5
LaSmAlBiO6	11b46f9	LaSmAlBiO6	La	Sm	Al	Bi	3	3	3	3
SrW_AlV_O6	11b46fb	SrWAlVO6	Sr	W	Al	V	2	5	3	2
AlSrCuGeO6	11b46fd	AlSrCuGeO6	Al	Sr	Cu	Ge	3	2	3	4
EuSbCoCuO6	11b46ff	EuSbCoCuO6	Eu	Sb	Co	Cu	2	5	4	1
DyEuGeSiO6	11b4701	DyEuGeSiO6	Dy	Eu	Ge	Si	2	2	4	4
CeK_InW_O6	11b4703	CeKInWO6	Ce	K	In	W	3	1	3	5
NdSrCeNbO6	11b4705	NdSrCeNbO6	Nd	Sr	Ce	Nb	2	2	3	5
SmSnFeGdO6	11b4707	SmSnFeGdO6	Sm	Sn	Fe	Gd	3	2	4	3
GdSrNdSeO6	11b4709	GdSrNdSeO6	Gd	Sr	Nd	Se	3	2	3	4
NaSrSnV_O6	b1b46dd	NaSrSnVO6	Na	Sr	Sn	V	1	2	4	5
GdTbMgSiO6	11b470c	GdTbMgSiO6	Gd	Tb	Mg	Si	3	3	2	4
CaLaDyFeO6	11b470d	CaLaDyFeO6	Ca	La	Dy	Fe	2	3	3	4
TbY_GeMgO6	b1b46e0	TbYGeMgO6	Tb	Y	Ge	Mg	3	3	4	2
CeNaCaV_O6	b1b46e1	CeNaCaVO6	Ce	Na	Ca	V	4	1	2	5
CaInGaV_O6	11b4710	CaInGaVO6	Ca	In	Ga	V	2	3	3	4
CeCoFe2O6	b1b46e4	CeCoFe2O6	Ce	Co	Fe	Fe	4	2	3	3
BiEuCuZrO6	b1b46e5	BiEuCuZrO6	Bi	Eu	Cu	Zr	5	2	1	4
BaCoMgTiO6	11b4711	BaCoMgTiO6	Ba	Co	Mg	Ti	2	4	2	4
BaGeFeSbO6	b1b46e8	BaGeFeSbO6	Ba	Ge	Fe	Sb	2	4	3	3
CeDyAlZrO6	b1b46e9	CeDyAlZrO6	Ce	Dy	Al	Zr	3	2	3	4
BaNdNiTiO6	11b4714	BaNdNiTiO6	Ba	Nd	Ni	Ti	2	2	4	4

Supported by NSF LSDI Data Infrastructure Building Blocks program and DOE BES Materials Project.

Figure 34*:* Screenshot of the Multinary Oxide dataset hosted on MPContribs (https://contribs.materialsproject.org/projects/Multinary_Oxides).

We validated the SPuDS software program used to generate initial perovskite oxide structures for DFT optimization. SPuDS accurately predicts perovskite oxide structures with multiple octahedral cations relative to experimental structures, which we expected would limit the computational expense of our HT DFT investigation generating a dataset of perovskite oxides. However, SPuDS has not been evaluated for a dataset of this scope or scale, i.e., with tens of thousands of DFT-optimized theoretical perovskite oxides with multiple A and B sites. We benchmarked SPuDS for HT DFT by comparing the structural fingerprint distances (SFPD) and structural similarity metrics (ε) of 66,516 SPuDS and DFT-optimized perovskite oxide structures, as more similar structures should result in less DFT optimization expense. As implemented in the Matminer python package, a structural fingerprint is a vector of statistical information, i.e., minimum, maximum, mean, and standard deviation, derived from a structure's coordination environment distributions. The SFPD is the normed difference between two structural fingerprints and quantifies two structures' similarity; according to the MP, structures with $0 \leq \text{SFPD} \leq 0.9$ are typically similar, whereas structures with $\text{SFPD} > 0.9$ are typically different. As implemented by the AFLOW software framework's Xtal-Finder, ε measures the structural similarity between two structures by computing deviations between crystal lattices ($\varepsilon_{\text{latt}}$) and mapped site positions ($\varepsilon_{\text{coord}}$). It also includes a failure metric ($\varepsilon_{\text{fail}}$) for incompatible structures. Hicks et al. reported that structures with $0 \leq \varepsilon \leq 0.1$ match and structures with $0.1 < \varepsilon \leq 0.2$ reside in the same family, whereas structures with $\varepsilon > 0.2$ are different. Because SFPD and ε are interpretable, scalar quantities, but are derived independently from one another, we compared SPuDS structures to DFT-optimized structures using both metrics.

We calculated SFPD vs. ε for the 48,742 compositions in the dataset where Xtal-Finder reports an ε. There is considerable agreement between SFPD and ε; by minimizing Gini impurities using the scikit-learn python package, we find that $0 \leq \text{SFPD} \leq 0.522$ generally corresponds with $0 \leq \varepsilon \leq 0.1$ and $0.522 < \text{SFPD} \leq 0.927$ generally corresponds with $0.1 < \varepsilon \leq 0.2$, which supports the Materials Project claim regarding SFPD. 25,349 of the 29,969 compositions with $0 \leq \text{SFPD} \leq 0.522$ have $0 \leq \varepsilon \leq 0.1$ (~85%), while 42,305 of the 45,250 compositions with $0 \leq \text{SFPD} \leq 0.927$ have $0.1 < \varepsilon \leq 0.2$ (~93%). Xtal-Finder is unable to map DFT-optimized structures to their starting SPuDS structures for the remaining 17,774 compositions. This does not necessarily mean that the structures for these compositions are dissimilar, however, as 13,549 of the 17,774 unmapped structures have $\text{SFPD} \leq 0.927$. Rather, this is a failure of the Xtal-Finder algorithm, which cannot always map the reference structure to the structure to be compared. Based on the general agreement between SFPD and ε, and because $\text{SFPD} \leq 0.927$ for 56,716 compositions in our dataset (~85%), we conclude that the majority of SPuDS structures either match or are in the same structural family as their DFT-optimized counterparts, meaning that SPuDS reliably estimates multinary perovskite oxide structures for HT DFT. We would therefore expect SPuDS to, on average, estimate initial perovskite oxide structures that are *at least* within the same structural family as their DFT-optimized counterparts. This should limit the computational expense associated with optimizing perovskite structures for the millions of multinary oxide compositions not reported in our dataset.

We performed an in-depth assessment the oxygen vacancy formation enthalpies of La_2MnNiO_6 (L2MN), $GdLaMnNiO_6$ (GLMN) and Gd_2MnNiO_6 (G2MN) perovskite oxides synthesized and characterized for their STCH activities. Known STCH perovskite oxide redox mediators --- including SLMA and BCM --- are reduced via off-stoichiometric mechanisms, whereby oxygen vacancies form in the perovskite structure at STCH thermal reduction temperatures. This mechanism preserves the perovskite phase over many redox cycles, which limits redox material degradation and results in near-constant STCH production. For the present investigation, we assumed that L2MN, GLMN and G2MN also operate by off-stoichiometric reduction mechanisms. We therefore estimated the experimental reduction enthalpies, ΔH_{TR}, of these materials from their oxygen vacancy formation enthalpies, ΔH_{Ovac}, calculated from DFT-computed energies using the equation below. Along with ΔS_{TR}, ΔH_{TR} is used to calculate ΔG_{TR}, which dictates the experimental STCH thermodynamics of redox mediators.

$$\Delta H_{Ovac} = E_{tot}^{defect} - E_{tot}^{host} + \mu_O,$$

E_{tot}^{host} is the DFT total energy of the bulk perovskite oxide, E_{tot}^{defect} is the DFT total energy of the reduced perovskite oxide, and μ_O is the reference chemical potential of oxygen. μ_O was taken from most stable oxygen reference entry tabulated in the Materials Project (mp-12957), with an additional 0.68 eV atom^{-1} energy correction to account for oxygen over-binding by GGA+U DFT. E_{tot}^{defect} were calculated for all symmetrically unique oxygen sites --- determined using pymatgen's SpaceGroupAnalyzer --- that are present in each 80-atom bulk perovskite oxide supercell. The DFT optimized B-site rock salt (RS) ordered structures have many symmetrically equivalent vacancies, each of which has only one unique vacancy computed with DFT. Fewer vacancies are symmetrically equivalent in the partially ordered structures, and all vacancies are unique according to SpaceGroupAnalyzer for the structures with Special Quasi-random Structure (SQS) random B-site order. The 2% defect concentration limit in the 80 atom supercells simulates experimental STCH vacancy defect concentrations and avoids spurious self-interactions with periodic images.

In **Figure 35** below, we compare the ΔH_{Ovac} distributions of L2MN, GLMN and G2MN perovskite oxides computed with B-site RS, partial, and random ordering. We also report the Boltzmann weighted average vacancy formation enthalpies, $\Delta\overline{H}_{Ovac}$, calculated for these systems assuming T_{TR} = 1350°C: $\Delta\overline{H}_{Ovac}$ = 3.70, 3.72 and 3.74 eV atom^{-1} for RS ordered L2MN, GLMN and G2MN, 2.92, 2.93 and 3.07 eV atom^{-1} for partially ordered L2MN, GLMN and G2MN, and 2.32, 2.40 and 2.42 eV atom^{-1} for randomly ordered L2MN, GLMN and G2MN. The difference in Boltzmann averaged vacancy energies across all compositions for *fixed B-site ordering* can be as small as 40 meV atom^{-1}, while the difference in averaged vacancy energies for a fixed composition with *variable B-site ordering* can be as large as 1.4 eV atom^{-1}. This difference in $\Delta\overline{H}_{Ovac}$ caused by the degree of B-site ordering is large enough to dramatically change the experimental STCH performances of these materials, and explains the distinct H_2 production capacities observed for L2MN and GLMN in contrast to that of G2MN.

This result indicates that the effect of cation disorder on the local oxygen atom/vacancy environment can significantly affect oxygen vacancy energetics and consequently, the ability of a perovskite to serve as a STCH redox mediator. This has considerable implications on the computational strategy required to reliably predict the performance, and thus screen, hypothetical redox mediators.

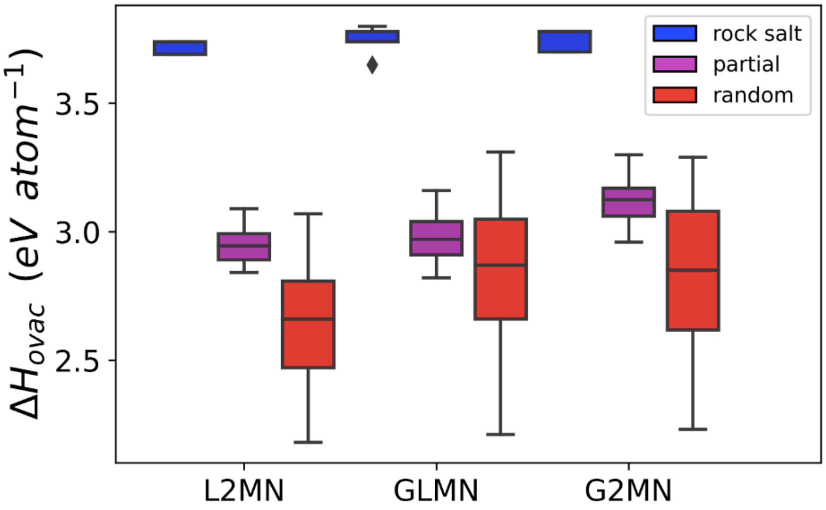

Figure 35: Distributions of oxygen vacancy formation enthalpies (ΔH_{Ovac}) for (left to right) L2MN, GLMN, and G2MN with (left to right) B-site rock salt, partial and random ordering.

Task 3: Kinetic screening of active materials

Subtask 3.1: Explicit computational modeling

We have identified a method for converging NEB calculations that significantly speeds up the calculation time. First the initial and final states are converged in the same manner as normal NEB calculations. Then, instead of converging the band using the initial/final k-point mesh, the band is converged at the Gamma point. After converging the band at the Gamma point, single point calculations are performed using the initial/final k-point mesh. This method has been shown to give accurate transition state (TS) energies for a variety of systems (**Figure**). In this study, 5 systems have been investigated: System 1 (Sys 1) is the hydrogenation of N* to NH* on the Fe(100) surface, System 2 (Sys 2) is the hydrogenation of NH_2* to NH_3* on the Fe(100) surface in the presence of spectator ions, System 3 (Sys 3) is the dissociation of N_2* on the Fe(100) surface, System 4 (Sys 4) is the migration of a N atom on a complex supported Fe nanoparticle, and System 5 (Sys 5) is oxygen diffusion in bulk hercynite. The accuracy of the calculated TS energy for the variety of systems studied shows the robustness of the Gamma-point method.

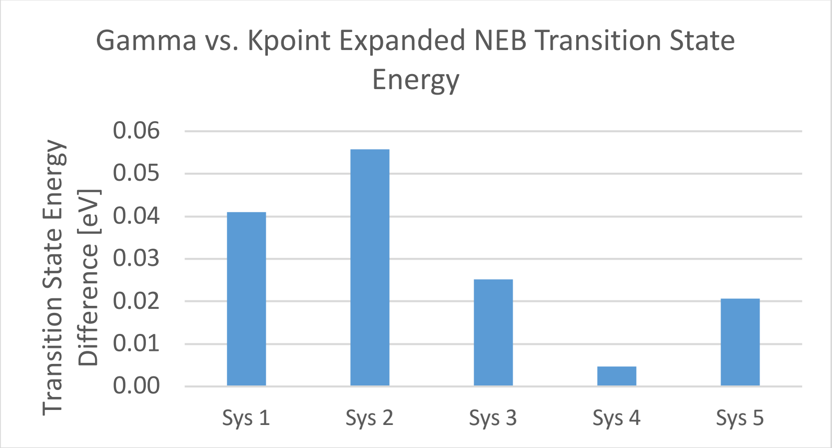

Figure 36: TS Energy Differences Between Gamma-point and K-point-expanded NEB Calculations – the largest error is < 0.06 eV, which is well within the accuracy limits of the method.

The Gamma-point method is in good agreement (±0.06 eV) with the k-point-expanded NEB calculations shown in **Figure** . In addition to producing accurate TS energy predictions, the Gamma-point method also reduces the computational cost dramatically (**Figure**).

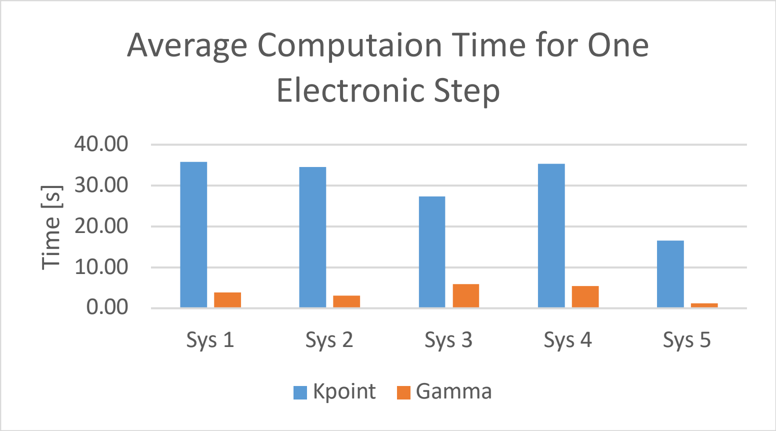

Figure 37: Computation Time Differences (Gamma-point vs. K-point-expanded)

Utilizing the Gamma-point method dramatically reduces computational expense without compromising accuracy for efficient TS calculations.

Using this approach, we extended the kinetic investigation we previously performed on hercynite to a variety of new materials. We illustrate some of what we took into consideration in the following summary of the current work on the oxidation reaction on pure hercynite. The conversion of water to hydrogen naturally occurs on the surface of whatever catalyst we are using, in this case hercynite. Because the water splitting reaction does not evolve oxygen with the hydrogen, we know the oxygen remaining on the surface occupies oxygen vacancies in the reduced material. At this point there are two possible reaction pathways, one where the oxygen vacancy participates in the hydrogen formation reaction, and one where oxygen remains on the surface over the course of the reaction and then separately combines with the oxygen vacancy. In either case how the hydrogen is actually formed also must be considered: it can desorb in a single concerted step off of the oxygen atom of water, or it can dissociate into unique sites across the surface, and then later form into H_2. There are four pathways by which hydrogen can arrange itself on the surface and be close enough to each other to form H_2, including a concerted mechanism. In addition, considering the previous possibility that oxygen on the surface results in 8 different pathways to explore, each with multiple transition states. Prioritizing calculating transition states for pathways that do not involve high energy intermediates allowed us to eliminate all pathways that don't involve an oxygen surface vacancy. For instance, the high energy intermediate of the pathway that does not involve an O vacancy is higher in energy than any other transition state. This ultimately resulted in only two pathways needing to be fully explored computationally for a total of four transition states. Accounting for the replenishment of vacancies from the bulk is similar to the process above, but more limited in scope due to the high degree of symmetry present in bulk systems. We have adapted symmetry analyzers in the code pymatgen to not only identify unique oxygen sites, but unique diffusion pathways. In pure hercynite, this left only 3 transition states that needed calculating.

A major challenge in high-throughput screening for kinetics is finding the global minimum energy pathway (MEP) for a reaction. This is due to the large number of: a) possible adsorption/vacancy sites, b) reaction coordinates, and c) adsorbate degrees of freedom, etc. To address this challenge we have developed an approach which significantly reduces the number of calculations needed to ensure a global MEP by employing the following automated workflow (**Figure 38**):

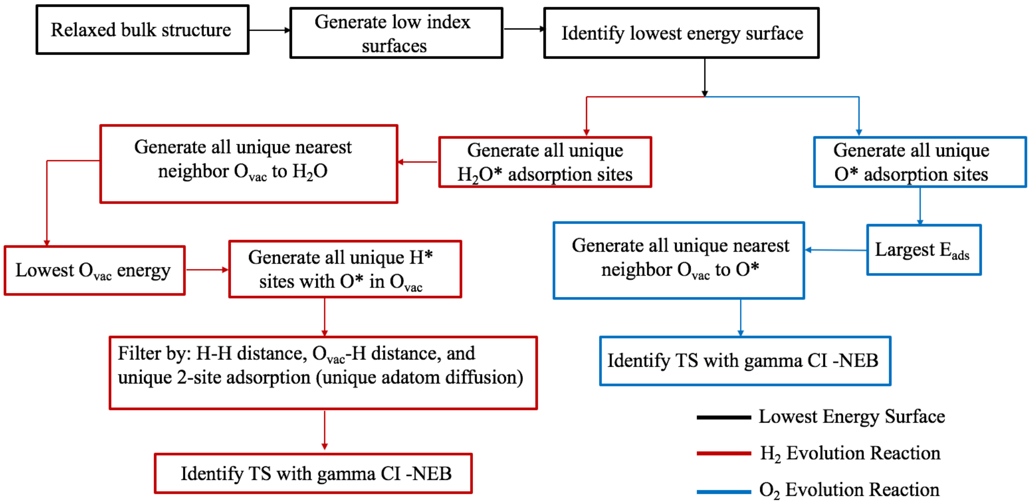

Figure 38: Algorithm and automated workflow for elucidating MEP for H_2 and O_2 evolution reactions. This workflow significantly reduced the number of calculations needed to ensure a global MEP for both reactions on any given metal-oxide surface.

We first identify the lowest energy surface by relaxing a number of low index slabs and determine which has the lowest surface energy relative to the bulk structure. Then using this slab, we generate all unique H_2O^*/O^* adsorption sites (using a script developed in Q2) and all unique oxygen vacancy (O_{vac}) sites nearest to the adsorbate. This ensures that we identify the lowest energy adsorption state that includes adsorbate-O_{vac} interactions. For the O_2 evolution reaction one additional geometry is generated: the lowest energy O_{vac} site. For the H_2 evolution reaction a number of intermediate states are generated. We showed in Q2 that this surface reaction proceeds through several routes including: metal-hydride formation, hydroxide formation, and even direct H_2 evolution (no intermediates). We generate intermediate structures including H^* sites within a reasonable distance from the O_{vac} site and then filter these structures to only include realistic H-H distances, and O_{vac}-H distances and to remove any unreasonable/duplicate pathways. This workflow ensures finding the global minimum adsorption state and a Climbing Image Nudged Elastic Band (CI-NEB), or Growing String Method (GSM) calculation reveals transition states (TS) and any intermediate geometries which may lie on the MEP. Intermediates are relaxed and a new CI-NEB/GSM path is created to confirm the TS. 1-3 initial pathways are generated for each material so that each reaction is well-described and the global MEP can be elucidated.

The results from this process are shown in **Figures 39** (**a-c**). Bulk diffusion and oxygen evolution are nearly identical for all materials, and are summarized in **Figures 39b** and **c**. In contrast, the H_2 evolution reaction has a number of intermediates, and so the complete reaction pathways for all 23 materials evaluated thus far are shown in Figure 5. To determine whether a reaction is feasible or not we apply the criteria that at STWS temperatures barriers of fast reactions are less than 3.25 eV, and barriers for reactions that occur, but potentially are too slow for effective STWS are less than 4.34 eV. We scale these values for bulk diffusion to account for the large number of diffusion events that must occur for macroscopic results.

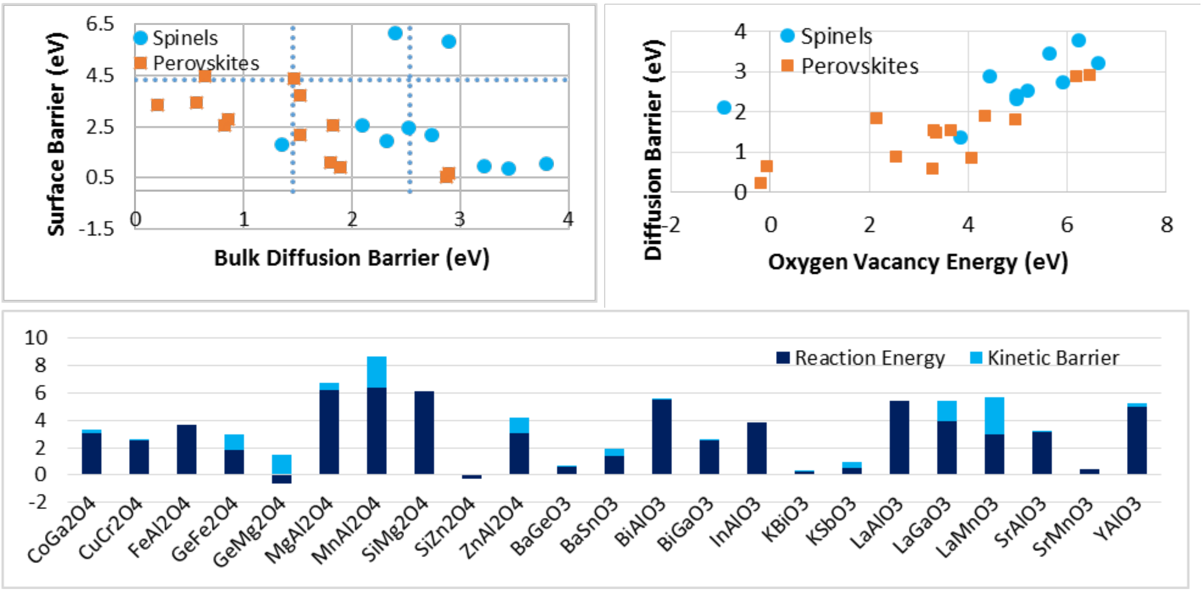

Figure 39: Complete reaction pathways for 23 perovskite and spinel materials. (a) Scatter plot of bulk barriers vs. rate limiting step barrier for H_2 evolution. Dashed lines indicate cutoffs for fast reactions, and feasible reactions. (b) Bulk diffusion barriers for all 23 materials plotted against the bulk oxygen vacancy formation energy. (c) O_2 evolution barriers for all materials. Most materials have no additional kinetic barriers.

Using the above criteria we analyzed the results of the kinetic calculations. Surface hydrogen evolution is insufficiently fast for 4 of the 23 cases, with 2 of these cases being borderline; most materials evaluated undergo fast surface reactions. The bulk reactions do not segregate as clearly, largely because of the "penalty" imposed by the many diffusion events. There are roughly equal numbers of materials with fast O vacancy diffusion, slow but feasible diffusion, and impractical diffusion. These results suggest that we should focus on understanding and modeling the bulk diffusion reactions as it is more likely to determine the kinetic viability of the water splitting material. Furthermore, we found a strong correlation between the diffusion barrier and oxygen vacancy formation energy suggesting that we can apply machine-learning to identify new descriptors to rapidly predict kinetics from more easily calculated thermodynamic properties as we generate more kinetic data. For the O_2 evolution reaction, ~30% of the materials have a surface reaction barrier for O_2 evolution larger than the barrier to create an oxygen vacancy and some materials possess moderately large vacancy formation energies. Thus, it is essential to identifying even the materials that have an additional barrier to O_2 formation to screen for kinetic viability. For kinetic studies, understanding when materials possess a barrier larger than the O vacancy formation energy was a priority.

Subtask 3.2: Identify TS characteristics

We developed efficient methods to identify reaction and diffusion transition states to accelerate the prediction of kinetic properties. Most of this effort initially focused on bulk transport. This effort has established an efficient approach to define upper and lower bounds on the transition state, which enables us to rapidly eliminate high barrier pathways. To achieve Milestone 3.2 we loosened some of the following constraints, but even our current approach is significantly faster than explicit transition state calculations. The methodology we have developed involves:

By definition, any point on the MEP (minimum energy pathway) must have an energy less than, or equal to the transition state energy. Finding any point on the MEP therefore gives a lower bound on the transition state energy. A normal relaxation run within VASP can only find two points on the MEP, the initial and final states. However, we can establish constraints that remove a single degree of freedom from the most mobile atom i.e. the one diffusing. This prevents relaxation down the MEP to the stable points. For bulk diffusion, we implemented this constraint by freezing the migrating atom to the plane equidistant from the initial and final state. This produces a reliable point on the MEP, generally close to what would be the transition state. From this MEP point (lower bound), we found an upper bound on the transition state by doing two separate IDPP pathways, from the MEP point, to both the initial and final state. An example of the results of this approach can be seen in **Figure 40**. To make the figure, we made an additional assumption, that the pathways were unimodal. This allowed us to use a unimodal search algorithm to find the maximum of each pathway with approximately 15

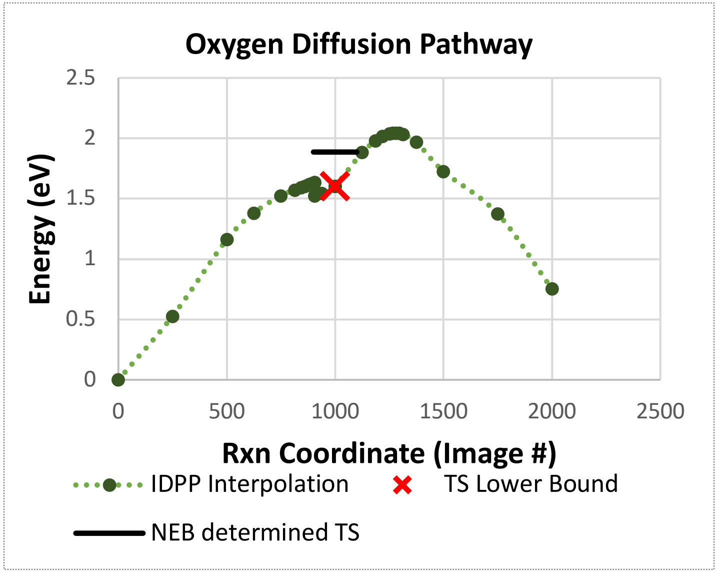

Figure 40: Results of constrained optimization and subsequent IDPP interpolation. The explicitly calculated NEB TS is provided to assess the relative accuracy of the upper and lower bounds provided by the methods presented.

single point calculations instead of the 30-70 points that normally would have been required to resolve the maximum within 0.01eV.

Using these bounds as a proxy for the transition state, the lower bound predicts the TS energy of various inverse and doped hercynite diffusions with a mean error of 0.20 ± 0.15 eV. The subsequent IDPP interpolation to determine the upper bound was less successful with a mean error of 0.60 ± 0.86 eV. We are examining two approaches to improve this result. The first is to use an improved interpolation method other than IDPP to prevent unrealistically short bonds. We are also looking at iterating the process, and finding a new constraint plane along the pathway to obtain a second point on the MEP. With more fixed points on the MEP, the interpolated pathway should deviate less from the true MEP.

We have also looked at applying the above methodology to surface reactions. However, additional complications arise associated with the surface reactions, namely more atoms participate in the reaction, and the presence of a vacuum space allows for a greater range of motion. Because of these issues, the approach has not been as successful. The constrained optimization results in states very close to either the initial or the final state. We are exploring ways to add more restrictive constraints to optimizations that still allow us to identify definitive upper or lower bounds on the transition state.

We have further developed the methods previously outlined and began to write and implement the automation necessary to apply these methods to high-throughput calculations. We have begun the process of systematically identifying possible oxygen vacancy diffusion pathways so calculations can be run with minimal manual input on relatively large numbers of candidate STCH materials. The process to do this is as follows: First, using symmetry analysis tools available in pymatgen, identify all unique oxygen environments. For each type of environment, select a representative oxygen atom. We use the centermost oxygen atoms for ease of visualization and to avoid any potential confusion associated with diffusing into neighboring cells. From here, all potential diffusion pathways are labeled. Once again, a symmetry analysis is performed to eliminate duplicate pathways. For hercynite this process identifies, 12 possible diffusion pathways, although only 3 of them are unique.

As can be seen in **Figure 41**, the upper/lower bound method successfully bounds the TS over a wide range of materials. The ranges on a few of the bounds are large enough to not be useful for screening, but even these still represent a significant improvement over a single point IDPP pathway, which can have errors well in excess of 100%. We have also begun quantifying the exact speedup achieved by only calculating reaction bounds; the bounding method only needs about one fifth of the force calculations.

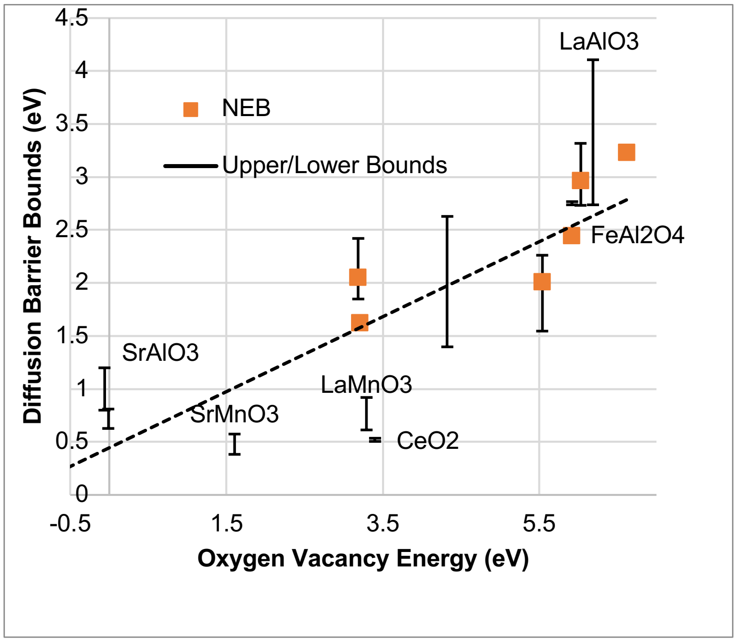

Figure 41: Diffusion Barrier vs. Oxygen Vacancy Energy. All depicted materials have upper and lower bounds, but are not visible when they are within 0.01 eV of the true TS.

Furthermore, on average the bounding method requires fewer force calculations (approximately 83) than even the fastest NEB we have currently performed (approximately 100 force calculations), and significantly faster than an average NEB (approximately 325 force calculations).

An initial guess for a path must be generated to execute a TS search using the CI-NEB method.

The conventional Image Dependent Pair Potential (IDPP) method was used to generate an initial guess for the reaction pathways. This method provides a reasonable guess for the reaction path in most cases, but fails significantly for H_2 and O_2 desorption (**Figure**). We have developed an algorithm and written a corresponding script to generate more realistic initial guesses for these systems that utilizes a Lennard-Jones (LJ) type potential (**Figure**). While this potential provides a better initial guess for O_2 and H_2 desorption, it is meant to demonstrate an approach for faster TS predictions for rapid kinetic screening and better potentials were implemented later.

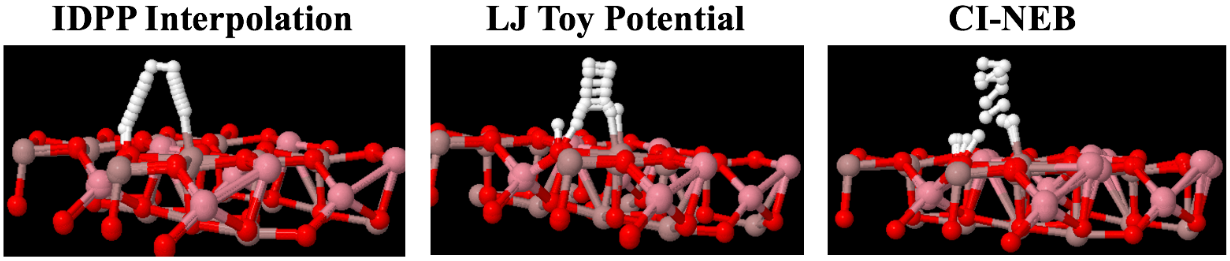

Figure 42: The conventional IDPP TS guess (left) fails for molecular desorption where an unrealistic desorption pathway is predicted. Using a LJ type potential (center), an initial path is generated that more closely resembles the converged CI-NEB path (right).

A linear interpolation is used to obtain an initial path, then an NEB calculation is performed using forces calculated by the approximate potential. This calculation is very fast due to the simplicity of the potential but is currently only developed for diatomic molecule adsorption/desorption, which are the two most relevant reaction types for STWS. The path predicted using the approximate potential provides a better initial guess for a DFT CI-NEB calculation. This script is still under development to generate improved initial paths for any given surface reaction. Our results indicate the possibility that simple atomic potentials could sufficiently describe complex PESs to enable rapid TS searches for truly high throughput kinetic screening.

At the cost of additional accuracy, we can speed up our process even further. The bulk of the computational expense is in using a constrained relaxation to determine the lower bound. By forcing this process to end early, we sacrifice our strict lower bound of the transition state but save the majority of the computational expense. This pseudo-lower bound can still used to determine an upper bound. **Compared to a single point IDPP interpolation, this reduces the error by ~60% and uses less than 50% additional CPU.** Both, the lower bound only, and upper/lower bound methods remained applicable to our screening. The decision of which method to use depended on how accurately we needed to know a given transition state.

Subtask 3.3: Rapid identification of kinetically active STWS materials

We applied the rapid TS identification approaches developed in subtask 3.2 to a variety of materials, the results of which are reported in publication 10. To further speed up this process, and possibly avoid explicit TS calculations altogether, we also deployed the SISSO machine learning approach on the collected results. Our preliminary model, used only limited input descriptors such as the material density, band centers, band gap and the vacancy formation energy. It is able to determine the TS bounds with a mean average error between 0.36 eV and 0.54 eV.

The number of materials investigated for neutral vacancy diffusion has increased to 70 unique materials. As is well-known in computational modeling, the calculation of kinetic properties is a computationally demanding task and this represents an extensive examination of the kinetic properties of hercynite and perovskite oxides. We investigated the effect of charged vacancies on the diffusion barriers, using the bounding methods we have developed and discussed in previous reports. Of the 20 materials for which we have studied both charged and neutral vacancies, 13 materials have diffusion barriers for charged vacancies that are lower than the vacancy diffusion barriers of their corresponding neutral vacancies by 0.5 eV, while only 3 have a charged diffusion barrier that is higher than that of the neutral vacancy by 0.5 eV. This result suggests that charged vacancies may be an important factor for determining kinetic viability of a material and was therefore be included in the kinetic evaluation of redox materials.

Expanding upon previous results, we have investigated 210 unique diffusion pathways for 90 different materials. We have also started to implement a machine learned model using SISSO to predict the vacancy diffusion barriers, using materials properties available from both the unit cell, and stable oxygen vacancy. Our model ultimately only used properties that could be calculated from the unit cell and predicts the average diffusion barrier of our bounded method with a RMSE of 0.38 eV (**Figure 43**).

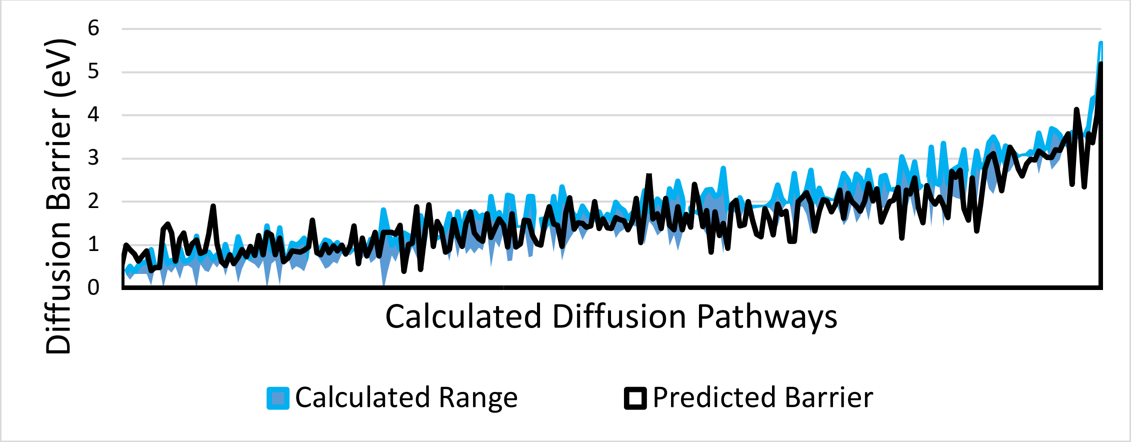

Figure 43: Calculated (blue) compared to predicted (black) diffusion barriers, for 210 diffusion reactions in 90 unique materials.

We began formally benchmarking the methods we derived to rapidly estimate oxygen vacancy diffusion, and thus the redox kinetics of candidate materials to determine how reliably our TS model identifies materials as either fast or slow as stated in Milestone 3.3.1. During this process, we also sought to compare our model derived using the SISSO ML method to other machine-learned models. For this benchmarking effort, we have not performed any explicit nudged elastic band (NEB) calculations. Instead, we have compared our results only to our bounded TS method discussed previously due to the extremely high computational expense of NEB calculations. At that time, 13% of the materials investigated have bounds that encompass our cutoff for fast and slow reactions (2.48 eV). For example, we calculated $CaSnO_3$ to have a lower bound of 2.13 eV, and an upper bound of 2.56 eV. Because of this, we cannot definitively say if oxygen diffusion in $CaSnO_3$ occurs with a barrier more than or less than the cutoff diffusion barrier of 2.48 eV. Because we are unsure of the kinetic viability of these 13%, we are unable to definitively claim if our faster machine-learned models correctly classify more than 90% of the materials we wish to investigate. However, there is no reason to presume that all 13% of the materials with lower and upper bounds that span the cutoff TS energy would be incorrectly classified. In assessing how accurate our model could be, we used a conservative estimate that half of the 13% will be incorrectly identified. This leaves us in search of a model that can correctly classify our materials as either fast or slow, with only a 3.5% failure rate for the remaining materials.

A simple linear regression model is incapable of achieving such a narrow failure rate. It misidentifies 27% of the remaining materials, justifying our search for a more sophisticated model. Using a decision tree classifier greatly improved this failure rate to only 5.7% before overfitting the available data. However, not only is this too high to be likely to hit our milestone but it misidentifies TS barriers significantly far from our 2.48 eV energy cutoff. The model generated by the SISSO ML approach and discussed in previous reports continues to be the best model we have analyzed. It misidentifies only 3.3% of the remaining data, which is within the 3.5% cutoff we previously established. Furthermore, all definitively misidentified diffusion barriers are within 0.5 eV of our cutoff energy, which indicates the accuracy of the model. Given these results, we later hit Milestone 3.3.1.

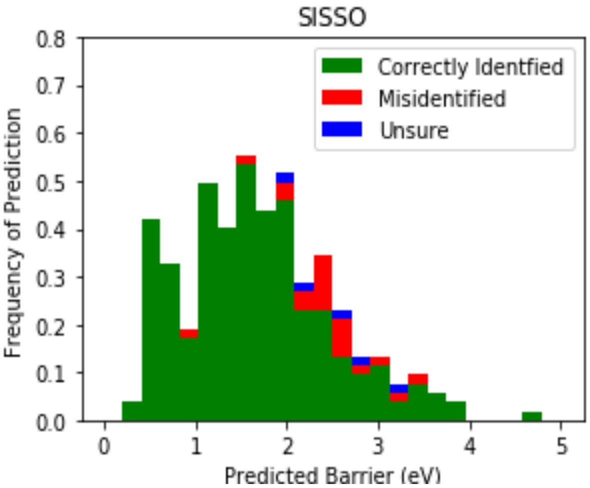

Figure 5: Diffusion barrier predictions for various models. In accordance with Milestone 3.3.1 the results are benchmarked not with their absolute error, but by whether they successful identify a material as fast (barrier < 2.48 eV) or slow (barrier > 2.48 eV). The green bars denote materials successful identified, while the red bars denote materials that have been misidentified. Blue bars show materials that cannot be successful classified because of uncertainty with the underlying bounding method. These combined errors have < 10% misidentification rate.

We implemented advancements that resulted in our meeting Milestone 3.3.1. To meet this milestone, we developed a model that can distinguish materials as either fast or slow water splitters, based on a strict 2.48 eV cutoff of the vacancy diffusion barrier. The origin of this strict cutoff is discussed previously. Materials with a predicted barrier less than 2.48 eV are presumed to be fast, and those with a barrier greater than 2.48 eV are presumed to be slow. We had developed a model with a failure rate of at most 16%. This failure rate was comprised of two sources of error. The first error is from the actual model, e.g. the model predicts a barrier over 2.48 eV, when the barrier is known to be definitively less than this value. The rate for this error was between 3% and 16%. The second source of error was from the underlying dataset. We did not calculate explicit transition state (TS) values, instead we used strict upper and lower bounds to the TS. Some materials have bounds that encompassed the cutoff, and as such could not be reliably determined as having a TS above or below the specified cutoff. 13% of the materials had TS bounds that encompassed the explicit TS cutoff energy.

To meet Milestone 3.3.1 we improved the error from both sources. We recalculated upper and lower bounds for the 13% of materials whose predicted upper and lower bounds encompassed the cutoff. After this recalculation only 2% of materials had barriers that spanned the cutoff energy. Furthermore, we performed a rigorous reevaluation of our machine learned model. Two major parameters for SISSO are the number of features to use in a given model, and the complexity of features (rung) used in that model. We determined that a model using more features, but with each feature being less complex created a more generalizable model that better fit our data. The new model has a misidentification rate of only 8%. The resulting classification from this SISSO model are shown in **Figure 5**.

Task 4.0: Experimental demonstration of active materials

Subtask 4.1: Experimental thermodynamic testing

During Q1, experimental thermodynamic testing was primarily concentrated on testing transition metal doped hercynite, $A_{0.5}Fe_{0.5}Al_2O_4$ (A=Mn, Ni, Cr, Co, Cu). Labview scripts were generated to allow for testing of these materials at temperatures consistent with the parameters of this proposal (i.e. T_{red}=1450°C and T_{ox}=1200°C) in the stagnation flow reactor. Each of the TM-doped hercynite materials was tested for 5 cycles at these conditions. The Mn-doped material was found to have the highest hydrogen production; however, additional experiments are now being conducted to reduce the standard deviation of the measured hydrogen production so further conclusions can be drawn and these results can be compared to predicted values.

In addition to testing spinels in the SFR, in Q1 we synthesized 15 new materials (both spinels and perovksites) which were tested in the SFR. These materials were synthesized using the citrate gel method. This method has been demonstrated to form homogeneous distributions of cations in the crystal structure and is thus ideal for the complex oxides used in this work.

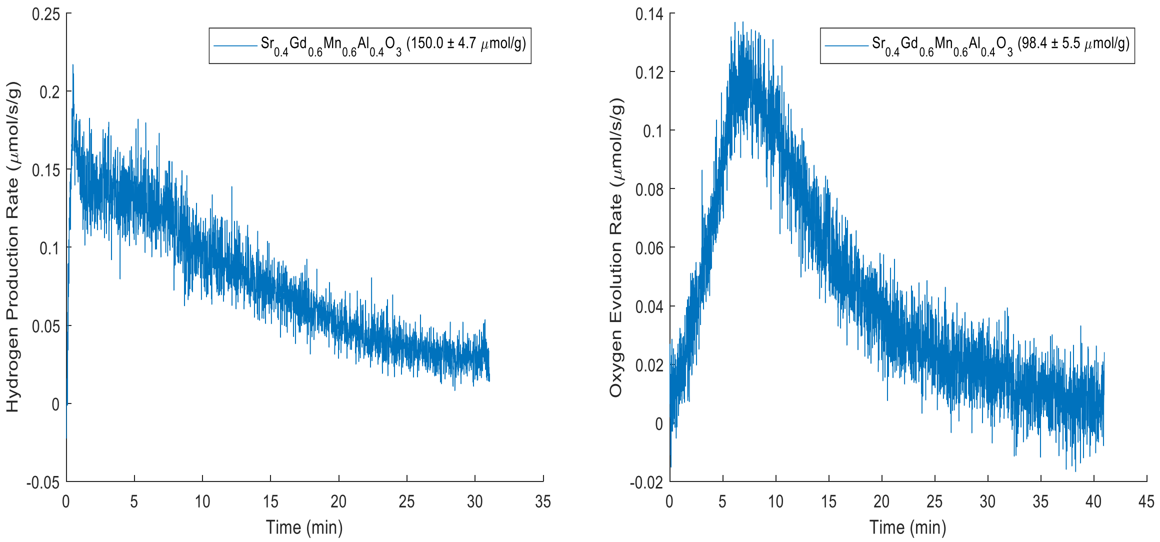

Figure 6: Resulting hydrogen and oxygen production rate from testing $Sr_{0.4}Gd_{0.6}Mn_{0.6}Al_{0.4}O_3$ at 1350°C reduction and 1000°C oxidation.

We used the TGA to analyze the extent of nonstoichiometry at various temperatures and oxygen partial pressure to further characterize the thermodynamics of various materials for STCH. We have modified our TGA, calibrated our mass flow controllers, and developed a procedure to enable this analysis. Initially we are focusing on characterizing hercynite ($FeAl_2O_4$). Preliminary experiments have been completed under a constant oxygen partial pressure of 1.91×10^{-4} atm at temperatures between 1000 to 1400°C. However, we have encountered some issues due to the slow kinetics of hercynite. The material did not reach an equilibrium oxygen nonstoichiometry during the two-hour isothermal hold initially utilized in the experiment. We planned to modify the procedure utilized in the experiment to allow for longer reduction times.

As discussed previously, gadolinium-based perovskites have been identified as promising candidate materials for further experimental testing due to their high m_e^*. Five different perovskites ($GdMnO_3$, $GdAlO_3$, $Sr_{0.4}Gd_{0.6}Mn_{0.6}Al_{0.4}O_3$, $Sr_{0.4}Gd_{0.6}Mn_{0.6}Ga_{0.4}O_3$, and $GdGaO_3$) were synthesized using the modified Pechini method. Formation of the perovskite phase was confirmed using X-ray diffraction.

Three of the five perovskites ($GdMnO_3$, $GdAlO_3$, and $Sr_{0.4}Gd_{0.6}Mn_{0.6}Al_{0.4}O_3$) have been tested in a stagnation flow reactor. Our computations predict that $GdMnO_3$ and $GdAlO_3$ will not produce significant amounts of H_2 due to their high O-vacancy energy (experimentally, this means that they should not reduce at reasonable temperatures). In contrast, $Sr_{0.4}Gd_{0.6}Mn_{0.6}Al_{0.4}O_3$ has a computed O-vacancy energy within the appropriate range to reduce and split water.

During initial testing, both $GdMnO_3$ and $GdAlO_3$ did not produce any oxygen or split water when operating at 1350°C for reduction and 1000°C for oxidation.

When $Sr_{0.4}Gd_{0.6}Mn_{0.6}Al_{0.4}O_3$ was tested in the reactor, hydrogen was produced when the material was reduced at 1350°C reduction for 60 minutes and oxidized at 1000°C oxidation for 30 minutes. After four redox cycles, the average production was 98.4 ± 5.5 µmol O_2/g and 150.0 ± 4.7 µmol H_2/g as shown in **Figure 6**. Testing of additional Gd-based materials and validation of the potentially promising performance of the $Sr_{0.4}Gd_{0.6}Mn_{0.6}Al_{0.4}O_3$ composition is ongoing.

In addition to these materials being investigated at CU, three materials have also been forwarded to our EMN collaborators Tony McDaniel, Eric Coker, and Andrea Ambrosini at Sandia National Lab for synthesis and testing using the laser-heated stagnation flow reactor and thermogravimetric analyzer (TGA): $Gd_{0.5}La_{0.5}Co_{0.5}Fe_{0.5}O_3$, $Ba_{0.8}K_{0.2}Ce_{0.5}Nb_{0.5}O_3$, and $Ba_{0.5}Sr_{0.5}Ce_{0.5}Zr_{0.5}O_3$. These materials are within 30 meV/atom of the hull and have high m_e^*.

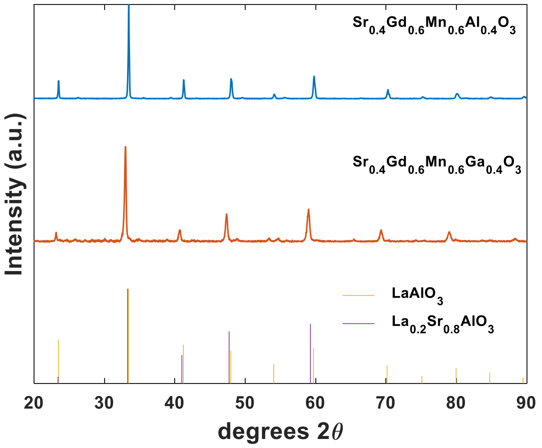

Figure 7: XRD patters for synthesized $Sr_{0.4}Gd_{0.6}Mn_{0.6}Al_{0.4}O_3$ and $Sr_{0.4}Gd_{0.6}Mn_{0.6}Ga_{0.4}O_3$ compounds compared to $LaAlO_3$ and $La_{0.2}Sr_{0.8}AlO_3$. Synthesized compounds formed cubic perovskites with no significant impurities.

At CU, we continued our study of Gd-based perovskites. The formation of the perovskite phase was confirmed with X-ray diffraction (XRD) using a Bruker D8 Advance diffractometer with Cu Kα radiation. The cubic perovskite phase was confirmed for $Sr_{0.4}Gd_{0.6}Mn_{0.6}Al_{0.4}O_3$ and $Sr_{0.4}Gd_{0.6}Mn_{0.6}Ga_{0.4}O_3$. These XRD patterns were compared to those of $LaAlO_3$ and $La_{0.2}Sr_{0.8}AlO_3$ and are shown in **Figure 7**.

These materials were further testing in the stagnation flow reactors at CU with a 1350°C reduction for 60 minutes under argon flow and a 1000°C oxidation for 30 minutes under 50 mol% steam flow in argon. Four cycles of reduction and oxidation were done and the average productivity was taken for the last three cycles. The average productivity of $Sr_{0.4}Gd_{0.6}Mn_{0.6}Al_{0.4}O_3$ was 173 ± 8.4 µmol H_2/g and the average productivity of $Sr_{0.4}Gd_{0.6}Mn_{0.6}Ga_{0.4}O_3$ was 70.8 ± 4.1 µmol H_2/g. We later evaluated the effect of changing the Gd content on the water splitting performance of both of these compounds.

In addition to the work being performed at CU, we also worked with our collaborators at Sandia National Lab to analyze additional materials. Three perovskite compositions calculated by UCB to be potential water splitting materials were chosen to be synthesized, characterized, and evaluated at SNL. To date, one of these ($Gd_{0.5}La_{0.5}Co_{0.5}Fe_{0.5}O_3$) has been successfully synthesized in nearly phase-pure form, characterized, and its redox capability verified. The synthesis routes for the other two compositions ($Ba_{0.8}K_{0.2}Ce_{0.5}Nb_{0.5}O_3$ and $Ba_{0.5}Sr_{0.5}Ce_{0.5}Zr_{0.5}O_3$) were still being optimized at the time of the completion of the project.

All three compositions were initially prepared by a solid-state synthesis approach wherein stoichiometric quantities of the respective metal oxides, carbonates, or nitrates were thoroughly mixed and then heat-treated. In addition, the two barium-containing compositions were prepared by the Pechini method (solution/combustion route using citric acid). Specific details of all attempted syntheses are given in Table . Phase purity was monitored by XRD.

Table 4. Synthesis routes and reagents used by SNL for synthesizing three new predicted materials

Target Composition	Synthesis route	Reagents				Calcination temperature/ °C
$Gd_{0.5}La_{0.5}Co_{0.5}Fe_{0.5}O_3$	Solid-state	Gd_2O_3	La_2O_3	Co_3O_4	Fe_2O_3	1200, 1300, 1400
$Ba_{0.8}K_{0.2}Ce_{0.5}Nb_{0.5}O_3$	Solid-state	$BaCO_3$	K_2CO_3	CeO_2	Nb_2O_5	1200, 1300, 1400
$Ba_{0.5}Sr_{0.5}Ce_{0.5}Zr_{0.5}O_3$	Solid-state	$BaCO_3$	$Sr(NO_3)_2$	CeO_2	ZrO_2	1200, 1400, 1500
$Ba_{0.8}K_{0.2}Ce_{0.5}Nb_{0.5}O_3$	Pechini	$Ba(NO_3)_2$	KNO_3	$Ce(NO_3)_3 \cdot 6H_2O$	Nb_2O_5	1200, 1300, 1400
$Ba_{0.5}Sr_{0.5}Ce_{0.5}Zr_{0.5}O_3$	Pechini	$Ba(NO_3)_2$	$Sr(NO_3)_2$	$Ce(NO_3)_3 \cdot 6H_2O$	$ZrO(NO_3)_2 \cdot xH_2O$	1400

A phase pure form of $Gd_{0.5}La_{0.5}Co_{0.5}Fe_{0.5}O_3$ was achieved after calcination at 1200 or 1300 °C, however after treatment at 1400 °C some phase segregation appeared to occur. The material calcined at 1300 °C was subjected to further characterization by SEM, TGA, and high-temperature XRD. **Figure 47** shows the room temperature XRD and SEM image of $Gd_{0.5}La_{0.5}Co_{0.5}Fe_{0.5}O_3$.

The $Ba_{0.8}K_{0.2}Ce_{0.5}Nb_{0.5}O_3$ composition contained a consistent impurity phase of CeO_2 that did not change with different calcination temperatures. The impurity phase $BaCeO_3$ was found to decrease as calcination temperature increased. When the calcination temperature was increased to 1400 °C, however, the material melted and bonded to the alumina crucible. The major phase at all calcination temperatures was identified as being similar to $Ba_5(Nb_4O_{15})$.

Attempts to prepare $Ba_{0.5}Sr_{0.5}Ce_{0.5}Zr_{0.5}O_3$ via solid state synthesis resulted in a mixture of $BaCeO_3$ and $SrZrO_3$ after calcination at 1400 °C. Calcination at 1200 °C gave a similar XRD pattern, but with broader peaks and some extra peaks, suggesting incomplete reaction. Increasing the calcination temperature to 1500 °C resulted in further decomposition into a mixture of (tentatively) $BaCeO_3$, $SrZrO_3$, SrO, CeO_2, $Ce_{0.95}Zr_{0.05}O_2$.

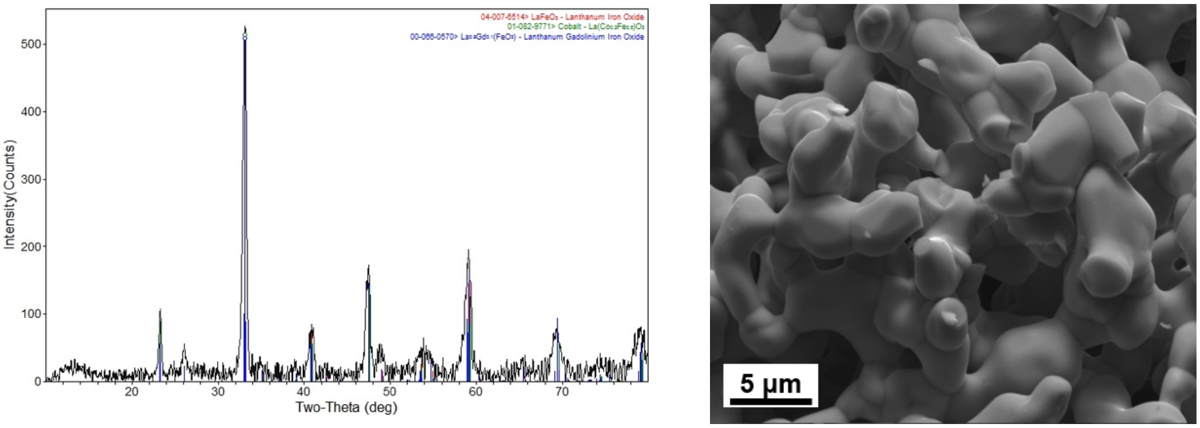

Figure 47: XRD powder pattern of solid-state synthesized $Gd_{0.5}La_{0.5}Co_{0.5}Fe_{0.5}O_3$ after calcination at 1300 °C (A), and SEM image of the same material (B).

Because the solid state syntheses of the two barium-containing compounds was unsuccessful, a solution based (Pechini) method was attempted. A water-soluble niobium salt could not be sourced for the $Ba_{0.8}K_{0.2}Ce_{0.5}Nb_{0.5}O_3$ synthesis, so the Nb_2O_5 powder was emulsified in the citrate solution of the other reagents prior to combustion. After self-combusting and calcining at 800 °C (5 °C/min ramp, 12h dwell), the sample was calcined at 1200 or 1300 °C (10 °C/min ramp, 12h dwell). The major phase obtained was again $Ba_5(Nb_4O_{15})$ which is a (111) plane-type layered perovskite structure, and CeO_2 was still present as a persistent impurity. The Pechini synthesis of $Ba_{0.5}Sr_{0.5}Ce_{0.5}Zr_{0.5}O_3$ produced a single phase $BaZrO_3$ with minor SrO impurity after calcination at 1400 °C. Extended heating at 1400 °C did not reduce the amount of SrO, while the perovskite appeared stable.

The sample of $Gd_{0.5}La_{0.5}Co_{0.5}Fe_{0.5}O_3$ that had been calcined at 1300 °C was subjected to three reduction-oxidation cycles in the TGA to verify its performance, and structural parameters were monitored in operando using high-temperature XRD. Three TGA cycles between reducing (argon) and oxidizing (air) conditions were performed, all recorded on the same specimen of $Gd_{0.5}La_{0.5}Co_{0.5}Fe_{0.5}O_3$. Only minor changes in performance were observed between cycles. A small mass loss step was observed during reduction around 740 °C for all three cycles. The large mass loss step (beginning ~ 1030 °C) shifted to slightly lower temperatures with repeated cycling. Upon initial exposure to air at 400 °C, rapid oxidation occurred, accounting for 36-44% of the total mass increase, followed by more gradual oxidation. Between 890 and 940 °C the material reduced under air and then re-oxidized. Upon cooling under air, a small mass increase was seen that mirrored the small step at low temperature seen during reduction.

Characterization of the phase evolution of $Gd_{0.5}La_{0.5}Co_{0.5}Fe_{0.5}O_3$ via in operando HT-XRD during redox cycling revealed some interesting traits. In the HT-XRD experiments, the specimen, dispersed on an alumina substrate, was cycled first under flowing helium from room temperature to 1250 °C and back down, followed by an identical thermal cycle under flowing air. For a sample that undergoes no reaction, one would see the diffraction peaks shift to the left during heating and to the right during cooling due to thermal expansion and contraction.

Four particular structural changes were observed. At point A during initial heating in inert atmosphere (around 700 °C), there begins a doubling of some of the major diffraction peaks. Considering the peak around 23 °2θ, it is even evident that part of the structure contracts (peak shifts to the right with increasing temperature) in contrast to normal thermal expansion. Referring back to the TGA data we see a small mass loss step just above 700 °C corresponding to the initiation of peak splitting. Once the reduction rate increases above 1000 °C the peaks in the XRD are clearly split. A full structural refinement has yet to be carried out for this data, however the splitting can be tentatively assigned to lower symmetry in the partially reduced perovskite, or structural splitting into two similar perovskite structures with differing oxygen vacancy concentrations (i.e., limited miscibility of the two forms). The peak splitting goes away during the re-oxidation cycle such that the material reverts to the same structure it was before cycling began.

Once the temperature reaches about 1100 °C another phase appears in the HT-XRD plot (**Figure 48**), indicated by box B. These peaks are tentatively assigned to the structure of a substituted Gd_2O_3, e.g., $La_xGd_{2-x}O_3$. Once formed at high temperature, these peaks remain during cooling in inert atmosphere. Once heated under air, however, they do disappear, therefore showing reversible phase segregation in this system. The subtle peaks shown by boxes C and D appear during heating under air, and could be associated with the unexpected mass loss (reduction) seen in the TGA data during re-oxidation between 890 and 940 °C.

Samples for two newly discovered materials were sent to SNL to be tested in the laser heated stagnation flow reactor (LH-SFR): $Sr_{0.4}Gd_{0.6}Mn_{0.6}Al_{0.4}O_3$ (SGMA) and $Gd_{0.5}La_{0.5}Co_{0.5}Fe_{0.5}O_3$

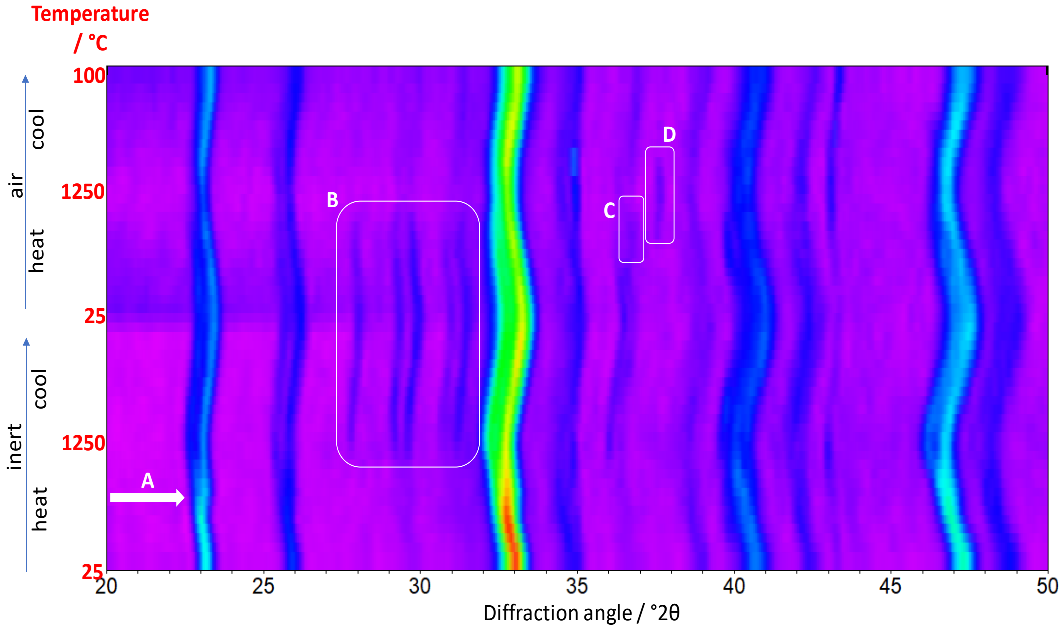

Figure 48: High Temperature XRD (HT-XRD) of $Gd_{0.5}La_{0.5}Co_{0.5}Fe_{0.5}O_3$ during two successive cycles, the first one reducing (helium, lower half of figure) and the second oxidizing (air, upper half). An XRD pattern was recorded every 100 °C between 100 and 1200 °C (up and down) plus two scans at 1250 °C.

(GLCF). SGMA was previously tested at CU and was been shown to split water. GLCF was characterized at SNL-NM, where it showed repeatable redox behavior in their TGA.

The first characterization of each material was an oxygen deficiency test, where 2000 ppm of O_2 in Ar was flowed through the reactor as it cycled between reduction and oxidation temperatures of 1350 and 850 °C, respectively. At higher temperatures, the material is expected to evolve oxygen to form oxygen vacancies and during exposure to H_2O at lower temperatures, the materials would fill those oxygen vacancies. Preliminary kinetic and thermodynamic information can be found from these tests. The results for SGMA and GLCF were compared to well characterized water splitting perovskites $Sr_{0.4}La_{0.6}Mn_{0.6}Al_{0.4}O_3$ (SLMA) and $BaCe_{0.25}Mn_{0.75}O_3$ BCM, respectively. The results show that SGMA has comparable kinetics, as indicated by the peak O_2 production rate, and thermodynamic properties, as indicated by the area under each peak, as SLMA. GLCF has better kinetics and thermodynamics properties as compared to BCM in this test. Both materials are indicated to be good candidates for water splitting.

Next, each material was tested under water splitting conditions. The material was reduced for 330 seconds under Ar flow at 1350 °C and was oxidized for 1200 seconds under 40 mol% steam at 1000 °C. The mass spectrometer signal is shown in **Figure 49**. Both materials show oxygen evolution during reduction and then produce hydrogen when exposed to steam. Over three cycles of oxidation, SGMA produced 158 ± 17 µmol H_2/g and over two cycles of oxidation, GLCF produced 133 µmol H_2/g. For comparison, SLMA and BCM produce 307 and 181 µmol H_2/g under similar testing conditions.

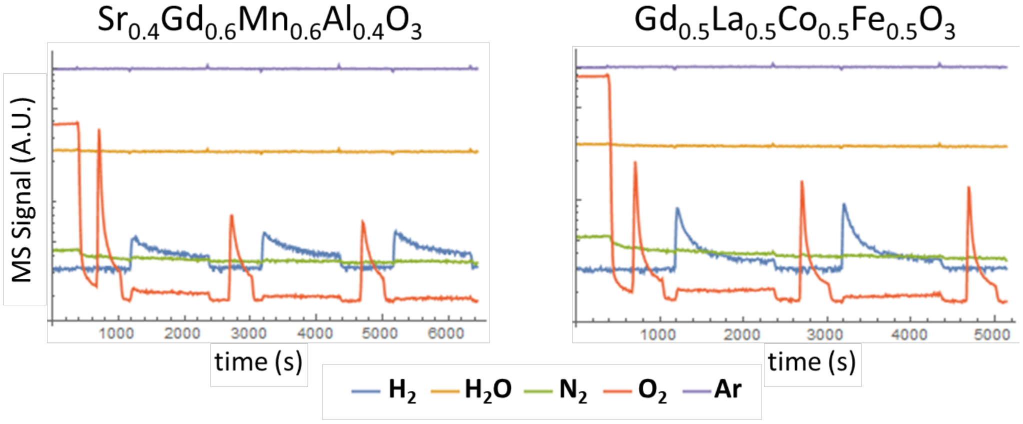

Figure 49: Mass spectrometer signals under water splitting and reduction conditions.

Both materials then underwent high conversion water splitting testing, where a set steam to hydrogen ratio H_2O:H_2 of 1333:1 was flowed during oxidation. This test is important because the process efficiency and commercial viability of STCH are closely related to the process steam requirement. The mass spectrometer signal from high conversion testing is shown in **Figure 50**. SGMA did not produce any hydrogen during the test while GLCF produced 25 µmol H_2/g. For comparison, SLMA and BCM produce 50 and 100 µmol H_2/g in this limit.

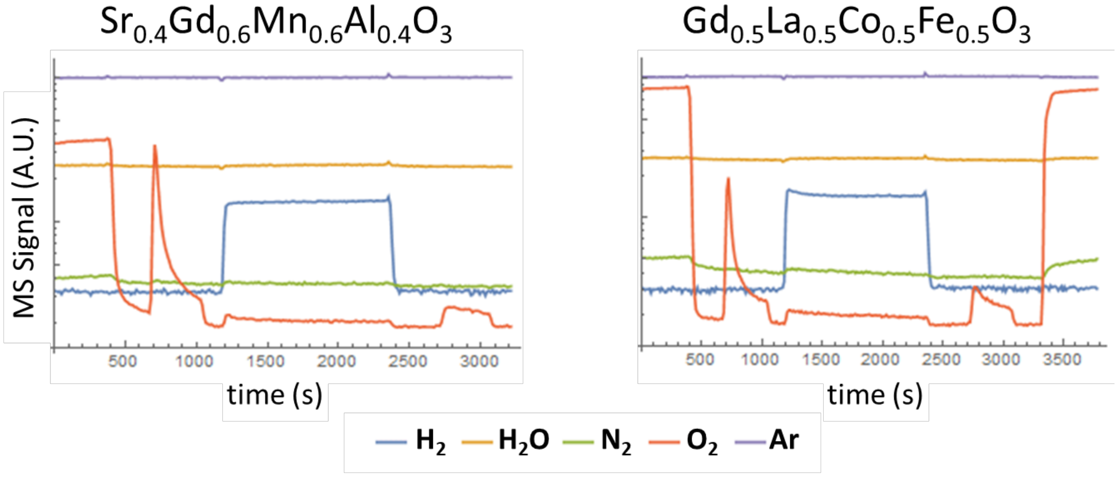

Figure 50: The mass spectrometer signals from high conversion testing.

We attempted to synthesize five computationally discovered materials ($Ba_{0.5}Sr_{0.5}Ce_{0.5}Hf_{0.5}O_3$, $SrCe_{0.5}Hf_{0.5}O_3$, $Ba_{0.5}Ce_{0.5}Hf_{0.5}O_3$, $Ba_{0.5}Sr_{0.5}CeO_3$, and $Ba_{0.5}Ca_{0.5}Ce_{0.5}Hf_{0.5}O_3$) via the modified Pechini method. The synthesis involves dissolving stoichiometric amounts of metal nitrate with citric acid in water. The solution is then mixed, dried, and then undergoes a two-step calcination process. The materials were first calcined at 850°C for 18 hours and then sintered at 1500°C for 6 hours.

Upon analyzing each sample with XRD, we identified the presence of the CeO_2 impurity phase in each of the five samples for four of the materials. Due to these impurities, these materials were not tested and more work must be done to understand why these impurities are present.

Five perovskites that were previously synthesized were tested in the SFR at the CU. Initially, these materials were found to contain ceria impurities. However, upon reexamining the XRD diffractogram, the perovskite phase was found to be present, so further testing was done.

Table 5: Perovskites tested at CU.

formula	FE_atom	bandgap	min_Ovac	max_Ovac	dHd	m_e
BaSrCe2O6	-3.60338	2.363	5.041	5.109	0.01471823441	22.197
Ba2CeHfO6	-3.6817	2.114	5.326	5.326	0.02047083226	19.508
BaSrCeHfO6	-3.64487	2.3584	5.335	5.335	0.07215486739	18.883
BaCaCeHfO6	-3.66347	2.142	3.321	5.657	0.07836764942	16.769
Sr2CeHfO6	-3.67776	2.3506	5.75	5.75	0.04986960605	15.92

All five materials, along with ceria, were tested for seven redox cycles under 1350 °C for reduction for 60 minutes and 1000 °C for oxidation for 30 minutes.

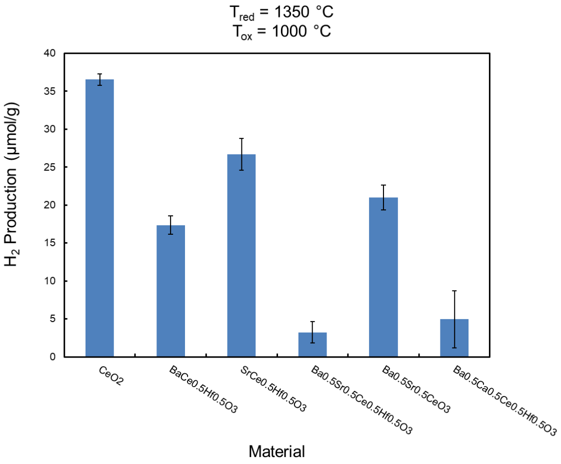

Figure 51: Average hydrogen productivity of perovskites tested at 1350 °C for reduction and 1000 °C for oxidation.

The average hydrogen production and standard deviation over the seven cycles are plotted in **Figure 51**. Ceria, known to need high reduction temperatures to yield high productivity, produced an average of 36 μmol H_2/g. Initial results show that these materials did not outperform ceria under the same reaction conditions.

Eight new computationally discovered materials were forwarded to the Weimer Lab at CU to be synthesized and tested. All materials were synthesized using a modified Pechini method, where metal nitrate salts of the corresponding cations were dissolved in DI water with citric acid. The materials underwent a two-step calcination procedure where they were heated at 850 °C for 24 hours in air and then 1500 °C for 6 hours in air. The perovskite phase was confirmed using powder X-ray diffraction (PXRD), where 5 of the 8 materials were successfully synthesized as perovskites: $CaZrMgMnO_6$, $CaHfMnNiO_6$, $CaHfMgMnO_6$, La_2MnNiO_6, and Nd_2MnNiO_6. PXRD measurements were conducted for these materials, which were then tested in the SFR at CU to verify if they split water.

Five materials were tested for seven redox cycles under 1350 °C for reduction for one hour and 1000 °C for oxidation for 30 minutes. During oxidation, the gas flow was comprised of 40 mol% H_2O.

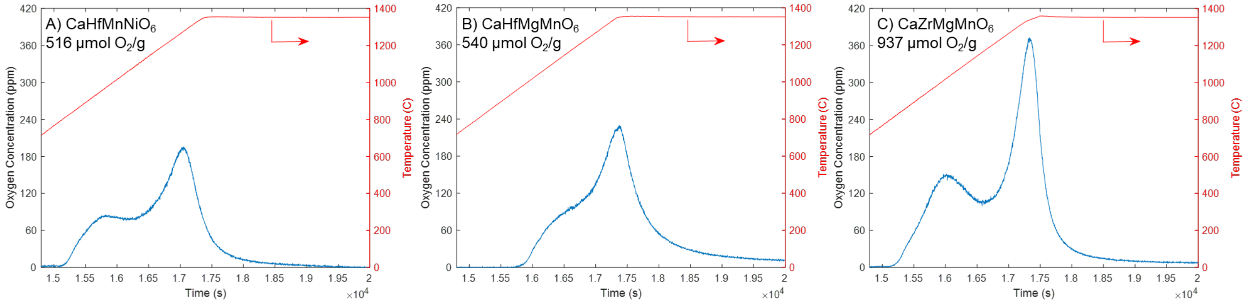

Figure 52: Oxygen evolution observed during the initial ramp up for Ca-Mn perovskites.

The Ca-Mn based perovskites evolved a large amount of oxygen during the initial ramp up, as shown in **Figure 52**. However, no water splitting was observed on the subsequent oxidation step.

The next two materials tested (La_2MnNiO_6 and Nd_2MnNiO_6) exhibited different behavior than the Ca-Mn based perovskites, as shown in **Figure 52**. Both of these materials exhibited water splitting behavior under the conditions tested. When compared to ceria (**Figure 53**), a higher yield and faster peak rate was observed with La_2MnNiO_6. Ceria had an average yield of 60 µmol H_2/g while La_2MnNiO_6 had an average yield of 142 µmol H_2/g, more than twice the average yield of ceria. Although Nd_2MnNiO_6 split water, it had a yield of only 23 µmol H_2/g.

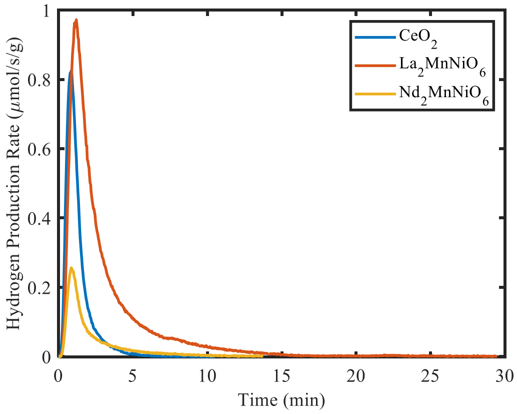

Figure 53: Water splitting behavior of La_2MnNiO_6 and Nd_2MnNiO_6 compared to CeO_2.

Our external experimental collaborators at SNL (Coker and McDaniel) characterized the GLCF perovskite and quantified its H_2 production during redox cycling. The room temperature XRD pattern of the synthesized GLCF was measured. The resulting material is isostructural to $LaFeO_3$, $GdFeO_3$, and $La_{1-x}Gd_xFeO_3$ (x = 0, 0.2, 0.5, 0.8, and 1), which are all orthorhombic perovskites. LeBail profile fitting analysis was performed, confirming the GLCF crystallizes in the Pbnm space group (No. 62) with no additional secondary phases. The lattice parameters for GLCF (a = 5.3973(3) Å, b = 5.4605(3) Å, c = 7.6455(4) Å) are slightly smaller than $LaFeO_3$ (a = 5.5506(6) Å, b = 5.5608(5) Å, c = 7.8464(9) Å). This is likely due to the smaller atomic radii of Gd and Co compared to La and Fe, respectively.

The redox behavior of GLCF was examined through thermogravimetric analysis (TGA), which monitors the mass change with respect to temperature and atmosphere (Ar or air). In the case of these materials, the mass change corresponds to gain/loss of oxygen. The mass change was converted to the extent of reduction (δ), assuming $Gd_{0.5}La_{0.5}Co_{0.5}Fe_{0.5}O_{3-\delta}$ during redox cycling. The as-prepared powder was subjected to redox cycles, comprising a reduction step at 1,250°C under Ar followed by a re-oxidation step at 1,100°C under air, corresponding to 0.16 atm O_2. The redox cycle was repeated twice with the two redox cycles showing similar behavior. The second redox cycle is shown in **Figure 54**. During thermal reduction, a shallow rate of weight loss was observed at ~750°C, followed by a steeper rate of weight loss onset at ~1,030°C. After the isotherm at 1,250°C, the extent of reduction (δ) was ~0.13. During re-oxidation, the mass sharply increased when the gas was switched from Ar to air at 400°C, followed by a more gradual increase as the temperature was raised. The dip in the extent of reduction observed between 900 and 1,100°C is attributed to a phase change in the material, that is, formation of a phase at around 900°C that ejects oxygen to achieve stability. This change in δ is reproducible between cycles. The sample mass returns to the starting mass after the re-oxidation step.

The water splitting capability of GLCF was verified using a stagnation flow reactor (SFR). The water splitting results were obtained with a thermal reduction temperature (T_R) of 1,350°C for 330 s and re-oxidation temperatures (T_O) of 850 and 1,000°C for 1,200 s under 40 vol% H_2O. Water splitting was observed under both sets of conditions, with the amount of H_2 produced increasing with each cycle. For T_O = 850°C (**Figure 54**), the amount of H_2 produced was 67, 90, and 101 μmol/g for each consecutive cycle. Moreover, significantly less O_2 was released in the second reduction cycle compared to the first cycle, likely due to the water splitting step being kinetically limited. This is also evident from the long tails of H_2 gas evolved during the re-oxidation steps. For T_O = 1,000°C (**Figure 54**), the H_2 capacity increased (127 and 141 μmol/g), evident of an improvement in the rate of water splitting at higher temperature. Similarly, more H_2 was produced as cycle-number increased. In an ideal situation, once steady state has been achieved, the amount of H_2 should be twice the amount of O_2 produced. From the SFR experiments with repeated cycles, GLCF is evolving and approaching this ideal steady state, though additional studies are needed to understand this behavior.

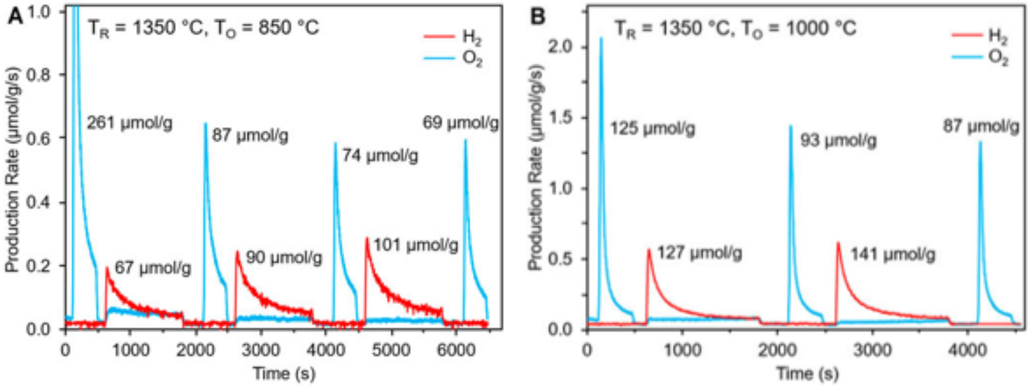

Figure 54. Water splitting experiment on GLCF at T_R = 1,350°C (330 s) and (**A**) T_O = 850°C and (**B**) T_O = 1000°C with 40% vol H_2O (1,200 s).

While $LaFeO_3$ was previously reported to have negligible solar thermochemical H_2O and CO_2 conversion behavior, similar perovskites to GLCF, i.e., $La_{0.6}Sr_{0.4}Co_{0.2}Fe_{0.8}O_3$ and $LaFe_{0.75}Co_{0.25}O_3$, were shown to be active for solar thermochemical CO_2 conversion (STCH activity is unknown), indicating that the mixing of Co and Fe may have contributed to the solar thermochemical conversion activity. For $La_{0.6}Sr_{0.4}Co_{0.2}Fe_{0.8}O_3$ and $LaFe_{0.75}Co_{0.25}O_3$, however, CO production decreased substantially during subsequent cycles. The substitution of Gd for La may have contributed to minimizing performance degradation as predicted by DFT calculations.

In terms of its water splitting ability, at T_R = 1,350°C and T_O = 850°C, GLCF produced more H_2 (101 μmol/g) than CeO_2 (50 μmol/g). However, GLCF produced less H_2 compared to the previously studied perovskite materials $BaCe_{0.25}Mn_{0.75}O_3$ (BCM) and $Sr_{0.4}La_{0.6}Mn_{0.6}Al_{0.4}O_3$ (SLMA4664). BCM and SLMA4664 produced 140 μmol/g (T_R = 1,350°C, T_O = 850°C) and 307 μmol/g (T_R = 1,350°C, T_O = 1,000°C) of H_2, respectively. However, direct comparisons of performance reported for different conditions (temperature, atmosphere, and time) for various materials that have different optimized conditions for STCH can lead to incorrect conclusions about the H_2 production capabilities of candidate materials. In the present case, the water splitting experimental conditions implemented for GLCF have not yet been optimized. Nevertheless, computational screening greatly accelerated the discovery of GLCF as a water splitting material, which would otherwise have been experimentally time consuming due to the vast chemical space of perovskite materials.

To understand the phase stability in GLCF during redox cycling, HT-XRD patterns were collected first from room temperature followed by increase temperature up to 1,250°C and decreased temperature to 50°C under He for thermal reduction, then with an identical temperature profile under air for re-oxidation. The GLCF sample was redox-cycled (T_R = 1,250°C under Ar, T_O = 1,100°C under air) before collecting the HT-XRD patterns. During the HT-XRD experiment, GLCF appears to maintain its perovskite phase as the major phase, but the major peaks broaden and exhibit some peak splitting occurring during reduction. In addition to the changes in the major GLCF phase, during cool down at ~1,200°C under He, additional peaks appear corresponding to the Gd_2O_3 phase. Due to the shift in peaks, it may have different chemistry (i.e., $Gd_{2-x}La_xO_3$). The additional Gd_2O_3 phase remains in the pattern until heated under air at ~700–800°C during re-oxidation. The disappearance of the Gd_2O_3 phase may correspond to the increase in the extent of reduction observed in the TG experiment at ~900°C during reoxidation. Moreover, a spinel phase appears during cool down under air. Overall, during the redox cycle, the perovskite phase persists, agreeing with the stable STCH activity observed in the SFR results and TGA cycling tests.

Our internal experimental collaborator at CU (Weimer) synthesized the GLMN and L2MN perovskites. PXRD confirmed the formation of the perovskite phase. The PXRD measurements for GLMN show that it adopts the monoclinic crystal system, which is the same crystal system exhibited by L2MN following synthesis using the method described, consistent with previous experimental characterization

STCH activity was tested at Sandia National Laboratories in a stagnation flow reactor (SFR, McDaniel) coupled with a laser-based sample heater and a downstream mass spectrometer. All experiments were conducted at sub ambient pressure (75 torr). Sample aliquots of the ~100 mg powdered materials were placed at the SFR stagnation plane in a shallow, loosely packed bed. A furnace was used to maintain the water-splitting temperature (T_{WS}) at 850 °C. Samples were heated from T_{WS} to a reduction temperature T_{TR} = 1350 °C by near-infrared laser irradiation at a rate of 10 °C s^{-1}. Samples were held at T_{TR} for 330 s under a continuous flow of UHP argon (Ar). After thermal reduction, the laser was turned off and the sample allowed to cool naturally to T_{WS} (elapsed time ~190 s) after which a flow of steam (40 mol%) in UHP Ar, or a dilute mixture of hydrogen in steam (40 mol% H_2O, H_2O:H_2 = 1333:1) and Ar, was introduced to the sample for a period of 1200 s. The flow rates of oxygen evolved during reduction, and hydrogen produced during oxidation, were measured using a mass spectrometer at a collection rate ~200 Hz. Representative water splitting cycle data for L2MN and GLMN are shown in **Figure 55**. Both samples were subjected to an initial reduction step from their fully oxidized states, followed by three complete water splitting redox cycles.

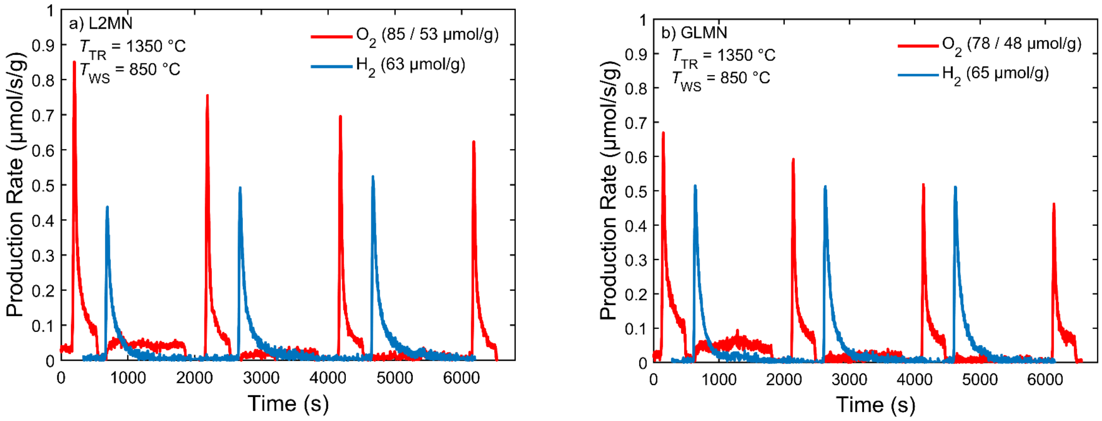

Figure 55. Oxygen and hydrogen production rates normalized by sample mass of a) L2MN and b) GLMN. T_{TR} = 1350 °C for 330 s in UHP Ar and T_{WS} = 850 °C for 1200 s in 40 mol% steam in Ar. The legend lists the integrated total for the first oxygen peaks and the averages of the subsequent oxygen and hydrogen peaks.

L2MN and GLMN exhibited similar hydrogen yields under the conditions tested; L2MN produced 52, 67, and 71 μmol g^{-1} hydrogen for each consecutive cycle, and GLMN produced 64, 65, and 66 μmol g^{-1} hydrogen for each consecutive cycle. These yields are higher than those observed for CeO_2 (50 μmol g^{-1}) and lower than those observed for GLCF (67, 90, and 101 μmol g^{-1} over subsequent cycles) under the same reaction conditions, in agreement with their computed $\overline{\Delta H}_{Ovac}$. Both L2MN and GLMN exhibited similar peak hydrogen production rates of approximately 0.5 μmol g^{-1} s^{-1}. For both samples, more oxygen evolved during the initial reduction step (85 and 78 μmol O_2 g^{-1} for L2MN and GLMN, respectively) than in subsequent reduction steps (57, 52, and 49 and 53, 47, and 44 μmol O_2 g^{-1} for L2MN and GLMN, respectively), suggesting that these materials do not return to their fully oxidized state in the 1200 s allotted for water splitting. This behavior has been observed in other water splitting perovskite oxides and is attributed to kinetically-limited reoxidation of these materials as well as thermodynamic limitations under the milder oxidation conditions of steam relative to oxygen.

Additional STCH material characterization was performed at the “low” steam-to-hydrogen ratio of 1333:1 using controlled mixing of hydrogen and steam. These conditions are used to evaluate a material’s oxidation performance in the presence of the H_2 reaction product to better represent operating conditions of industrial reactors. Small amounts of hydrogen lower the oxygen chemical potential in the gas by orders of magnitude relative to 40 mol% steam, which has a profound effect on a material’s ability to re-oxidize. The thermodynamic driving force to split the water molecule and re-populate lattice oxygen vacancies in the material drops by orders of magnitude under this high conversion condition. Any material deemed commercially viable will have to maintain water-splitting favorability in $H_2O:H_2$ ratios < 10. A water splitting cycle for L2MN, GLMN, and GLCF at the steam-to-hydrogen ratio of 1333:1, and comparison to other materials, is shown in **Figure 56**.

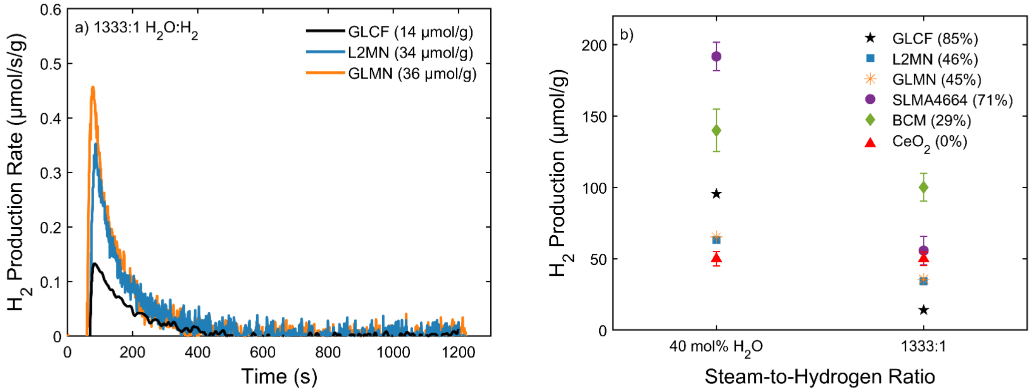

Figure 56: a) Mass-normalized H_2 production rate measured under high conversion water splitting conditions of GLCF, L2MN, and GLMN at a 1333:1 steam-to-hydrogen ratio. T_{TR} = 1350 °C for 330 s in UHP Ar and T_{WS} = 850 °C for 1200 s in a mixture of H_2, H_2O, and Ar as described in the text. b) Comparison of water splitting activity of GLCF, L2MN, and GLMN to SLMA4664, BCM, and ceria under the same conditions for both 40 mol% steam and high conversion conditions. The legend indicates the percent reduction in water splitting activity from 40 mol% steam to a 1333:1 steam-to-hydrogen ratio.

As discussed above, the water splitting behaviors of L2MN and GLMN are similar under conditions that use steam to drive the oxidation to the kinetic limit by flushing away all product H_2. These materials produce less hydrogen than GLCF. This suggests that L2MN and GLMN possess similar water splitting thermodynamics--- as predicted by DFT ΔH_{Ovac} calculations--- and kinetics at these conditions. However, GLMN and L2MN exhibit enhanced water splitting behavior relative to GLCF under high conversion conditions, as these materials produce 36 μmol g^{-1} and 34 μmol g^{-1} hydrogen compared to 14 μmol g^{-1} observed for GLCF. Most known water splitting materials do not produce hydrogen under high conversion conditions due to the low equivalent oxygen partial pressure present during reoxidation (2.5×10^{-12} atm for a steam-to-hydrogen ratio of 1333:1). To date, only a few water-splitting materials, including BCM, SLMA and CeO_2, have been shown to produce hydrogen under these conditions. As discussed above, the addition of gadolinium shifts the ΔH_{TR} of some oxygen vacancies in GLMN closer to the ΔH_{TR} of CeO_2, enabling GLMN to split water at high conversion. At a steam-to-hydrogen ratio of 1333:1, GLMN and L2MN maintain ~56% of their hydrogen yields relative to 40 mol% steam conditions, and therefore exhibit decreasing hydrogen yields with decreasing steam-to-hydrogen ratios. This behavior is similar to that of BCM but dissimilar to that of CeO_2, which exhibits no reduction in hydrogen yield at steam-to-hydrogen ratios of 285:1.

We used our computational screening approach developed in this project to screen Gd containing perovskite oxides as STCH redox mediators. Experimental testing at SNL by Tony McDaniel found that L2MN and GLMN were both competent redox mediators and importantly, maintained their hydrogen splitting ability at high H_2:H_2O ratios. However, G2MN was not active, even at higher reduction temperatures. We focused on determining what gives rise to G2MNs inactivity and justify the experimentally observed STCH activities of L2MN and GLMN, and the STCH inactivity of G2MN, here.

Viable STCH redox mediators should have ΔH_{TR} that approach or are greater than the standard state formation enthalpy of steam, $\Delta H_{H_2O(g)} \approx 2.5$ eV atom^{-1}. Although redox mediators with $\Delta H_{H_2O(g)} < 2.5$ eV atom^{-1} may still split water, they require additional electrical or mechanical work during STCH cycling that lower the overall process efficiency. However, viable STCH redox mediators should also have ΔH_{TR} smaller than that of ceria, which is considered to be the gold-standard STCH perovskite redox mediator, but requires high T_{TR}. While ceria exhibits exceptional STCH hydrogen production for $1500°C \leq T_{TR} \leq 2000°C$, its large ΔH_{TR} leads to insufficient H_2 production at $T_{TR} = 1350°C$, and even at $T_{TR} \leq 1500°C$. To avoid the complexities of engineering ultra-high temperature industrial STCH reactors, a T_{TR} significantly below 1500°C is desired, and as such viable STCH perovskite oxide candidates should have computationally predicted ΔH_{Ovac} less than that of ceria.

The $\Delta \overline{H}_{Ovac}$ of RS ordered L2MN, GLMN and G2MN discussed above are approximately 200 meV atom^{-1} less than the ΔH_{Ovac} of ceria computed using Materials Project compatible parameters in GGA+U DFT by Bare et al. (Ref 11) in our high throughput screening study ($\Delta H_{Ovac} = 3.95$ eV atom^{-1}). However, they are almost identical to the ΔH_{Ovac} of ceria in the 1.5% defect concentration limit computed for this work ($\Delta H_{Ovac} = 3.75$ eV atom^{-1}), which predicts that RS ordered L2MN, GLMN and G2MN should form similarly nonappreciable concentrations of oxygen vacancies at $T_{TR} = 1350°C$. In fact, these systems could generate less hydrogen by STCH than ceria, as they have less positive, electronic entropy than that associated with the Ce^{4+} to Ce^{3+} reduction that makes ceria's oxygen vacancy formation more favorable at STCH conditions. Furthermore, and as confirmed by DFT, G2MN's octahedral tilting magnitude(s) are larger than those of GLMN or

L2MN (32-33° vs. 26-31° or 23-25°) due to Gd's smaller radius. Greater octahedral tilting encourages RS Mn^{4+}/Ni^{2+} ordering, because the B-sites are closer and thus the B-site electrostatic repulsion, as quantified by the Madelung energy, is more significant. G2MN with B-site RS ordering can therefore explain its STCH inactivity at the conditions tested.

Partial B-site ordering with some anti-site defects explains L2MN and GLMN's similar STCH behavior at both the standard and high conversion conditions tested. Partially ordered L2MN and GLMN have essentially the same DFT vacancy energetics ($\Delta\overline{H}_{Ovac}$ = 2.92 eV atom^{-1} vs. $\Delta\overline{H}_{Ovac}$ = 2.93 eV atom^{-1}), which are well below the upper limit defined by ceria's ΔH_{Ovac} = 3.75 eV atom^{-1}. These $\Delta\overline{H}_{Ovac}$ are also above that of GLCF ($\Delta\overline{H}_{Ovac}$ = 2.77 eV atom^{-1}) reported by Bare et al. Larger $\Delta\overline{H}_{Ovac}$ indicate larger ΔH_{TR} with greater *thermodynamic driving force* for H_2O splitting than smaller $\Delta\overline{H}_{Ovac}$, forming fewer, but more potent vacancies that can still generate H_2 despite it already being present in steam at high conversion conditions. Fewer vacancies with larger ΔH_{TR} explains why the $GdLaCoFeO_6$ (GLCF) reported by Park et al. (Ref 8) produces the most H_2 at standard conditions, followed by L2MN and GLMN, and lastly ceria. In contrast, more potent vacancies with larger ΔH_{TR} explains why ceria produces the most H_2 at high conversion conditions, followed by L2MN and GLMN, and lastly GLCF.

Subtask 4.2: Experimental kinetic testing

Work done in this subtask was done in conjunction with Subtask 4.1.

Key Intermediate Accomplishments:

The following list of intermediate accomplishments were reported as key updates to the project in quarterly reports:

- Database of experimentally obtained thermochemical information populated with ~450 compounds.
- User-friendly *Python* module launched that allows for the generation of thousands of meaningful features from electronic structure calculations.
- Bash scripts generated to automate the screening of bulk and oxygen defect perovskite and spinel structures.
- 1,818 bulk perovskite structures calculated using DFT to compute the total energy, formation enthalpy, and band structure.
- 60 spinel structures calculated in the normal and spinel structure using DFT.
- Transition state searches using a lower energy cutoff and k-point grid to save significant computational time (>75%) was benchmarked; Majority of the explicit computational kinetic model calculations were completed using this approach.
- Demonstrated that a constrained optimization of the TS can produce a relatively strict lower bound on the TS in a fraction of the time of a full TS calculation.
- New ML tolerance factor τ for perovskite stability that improves significantly upon all known tolerance factors – *enables the screening of compounds that form perovskites.*
- ML model $G(T)$ developed for the Gibbs energy as a function of temperature of an arbitrary inorganic crystalline solid – 1st such descriptor of its kind – *enables the rapid screening of compounds for stability at T < 1800K.*
- Utilized ML model τ to screen >1.1M perovskites for stability; 27,015 materials predicted to be stable – *enables the practical screening of this materials subset with DFT.*

- 1,380 ternary and double perovskites screened based on oxygen vacancy formation enthalpy – *enables the comparison with experimental O-vacancy formation energy and water splitting ability to test if its accurate prediction and its ability as a criteria for STWS.*
- Calculated large electronic entropy from charged defects and isolated Fermi band may explain hercynite's superior performance over other spinel aluminates (with NREL EMN)
- Enhanced understanding of defect formation in spinels shows that more advanced descriptors are required for accurate thermodynamic screening – may *enable the discovery of an effective descriptor* (with NREL EMN).
- Automated bulk reaction calculations to identify all unique pathways, and intermediate structures with no human input– *enables the rapid kinetic screening of new materials.*
- Applied rapid transition state bounding method to new materials – *enables the rapid screening of thermodynamically screened materials for STCH kinetic ability.*
- Initial algorithms for automated generation of surface reaction pathways developed.
- New tolerance factor τ for perovskite stability shown to generalize extremely well to double perovskites (91% accuracy compared to 92% accuracy for ABX_3 compounds in general).
- Our new ML model $G(T)$ predicts Gibbs energies of arbitrary compounds with near-chemical accuracy (~40 meV/atom).
- Millions of phase diagrams constructed from known materials to quantify the stability and metastability of compounds as a function of temperature and composition.
- 432 defect calculations completed for stable ternary perovskites to calculate the oxygen vacancy formation energy.
- 1,021 bulk calculations completed for double perovskites.
- Charged and neutral defects computed for spinel aluminates.
- A number of scripts and algorithms have been developed to automate and accelerate the generation of transition states.
- The new transition state search and automated workflow of kinetic calculations reduces the number of calculations needed to ensure a global minimum energy pathway.
- Transition states for the H_2 Evolution Reaction, O_2 Evolution reaction, and bulk diffusion reaction calculated and kinetics analyzed for 23 spinels and perovskites.
- Showed bulk oxygen vacancy diffusion as the rate limiting process which thus determines the kinetic viability of water splitting materials.
- A simple approximate potential provides a better initial guess for the transition state of the hydrogen evolution surface reactions than the conventional IDPP method.
- Rationally designed atomic potentials describe complex reaction energetics sufficiently well for rapid TS searches (additional tests are ongoing).
- Accuracy of $G(T)$ ML model predicted Gibbs energy (~40-50 meV/atom) competitive with first-principles quasiharmonic calculations (~30-40 meV/atom) that take many orders of magnitude more CPU time to compute.
- $G(T)$ model allows for rapid screening of stability for STCH materials at STCH-relevant conditions, solving a major challenge in screening materials for high temperature applications.
- Demonstrated the importance of charged antisite+vacancy defect pairs in explaining the water splitting ability of hercynite – this was not previously recognized by the field, and was explored with NREL EMN node Lany.

- Developed complete and useful models for determining material stability of perovskite materials with minimal first principles calculations, which enables a second, highly efficient and necessary screen for perovskite STWS materials.
- Developed method to calculate upper bound on TS using only 50% more CPU than single point calculation but reducing overall error by 60%. TS search would normally require ~100 times more CPU than single point calculation.
- Preliminary ML models predict TS energies with an average error of 0.3 eV to 0.5 eV, which may be sufficient for initial screening of non-viable reaction pathways.
- Kinetic calculations agree with experimental peak rates, once the surface site prevalence is included in the model.
- DFT calculations of the convex-hull phase diagram determine the decomposition reaction and stability of the surviving perovskite compounds in a highly accurate manner.
  Upper and lower bounds on the diffusion barriers for 50 unique materials have been determined.
- Utilized more accurate computational methods, including RPA, HSE, and QHA to understand the deviation in the extent of reduction between DFT calculations and experimental results.
- Applied the new bounded transition state scheme to complete additional TS estimates.
- Determined that the formation of charge defects aids oxygen vacancy diffusion.
- Expanded kinetic screening to include charged defects.
- Initiated conversation with the Materials Project group (Persson) about open source data storage.
- Generalizable workflow written for high-throughput materials design.
- High-throughput screening of existing materials databases developed/deployed.
- Identified 44 candidate materials from screening of 343 ternary perovskites.
- Increased number of bounded TS calculations.
- Developed model to predict bulk kinetics requiring only information available from cheap unit cell calculations.
- Completed ternary perovskite screening based on vacancy formation energy and stability.
- Identified candidate ternary perovskites from an effective mass/stability analysis to be optimized by alloying.
- Utilized structure prediction (SPuDS) to minimize computational expense of DFT geometry optimizations and to screen for stable perovskite polymorphs.
- Demonstrated that SPuDS predicted structures are quantitatively similar to DFT optimized structures.
- Showed that the magnetic state is important for accurate vacancy formation calculations.
- Characterized lanthanum and gadolinium oxide perovskites by effective mass.
- Identified gadolinium oxide perovskites as a potential new space for additional research due to its high effective masses.
- Developed a workflow to generate pseudo-randomized, highly-probable multinary perovskite alloys from computed ternary perovskite structures.
- Performed charged vacancy calculations in kinetic screening.
- Added new materials to improve the machine learned model for kinetic screening.
- Developed a methodology for characterizing the extent of nonstoichiometry for materials using the TGA for thermodynamic testing, with a current focus on $FeAl_2O_4$.

- Generated a database of over 75,000 Tau stable multinary perovskite compositions in over 527,000 SPuDS predicted structures (7 tilting systems per composition).
- Refined over 26,000 multinary SPuDS predicted structures using DFT.
- Computed oxygen vacancy formation enthalpies for 359 stable multinary perovskite structures.
- Demonstrated that the SISSO model for predicting oxygen vacancy diffusion barriers has the highest success rate relative to other machine-learned models with a success rate of 96.7% for materials characterized using our barrier bounding method.
- Synthesized and began testing the water splitting abilities of the gadolinium-based perovskites $GdMnO_3$, $GdAlO_3$, $Sr_{0.4}Gd_{0.6}Mn_{0.6}Al_{0.4}O_3$, $Sr_{0.4}Gd_{0.6}Mn_{0.6}Ga_{0.4}O_3$, $GdGaO_3$.
- Demonstrated $Sr_{0.4}Gd_{0.6}Mn_{0.6}Al_{0.4}O_3$ as a successful water-splitting material.
- Generated a database of over 836,000 multinary perovskites with accurately predicted structures using SPuDS. Optimized >68,000 of these structures with DFT.
- Identified La, Gd, and Ce as promising elements for maximizing the electronic effective mass, m_e^*, including materials beyond the perovskite space.
- Began uploading this multinary perovskite database to Materials Project (MP), who we are now collaborating with to make this data publicly available.
- Demonstrated strong correlation between formation energies and lattice constants rapidly predicted by the bond valence method and DFT predicted values tabulated in MP.
- Utilized both tabulated materials data and our DFT calculations to screen > 50,000 multinary oxide perovskites by: 1) decomposition enthalpy and 2) effective mass.
- Identified 76 promising multinary perovskites for which neutral oxygen vacancy calculations were performed. 40 of these had O-vacancy energies within the STCH active range.
- Demonstrated quantitative agreement between computationally predicted and experimentally observed reduction capacity in hercynite.
- Performed additional calculations to reduce predicted transition state range of candidate materials and utilized these results to develop a machine-learned model for predicting kinetic viability of new materials with < 8% failure rate.
- Successfully synthesized and characterized $Gd_{0.5}La_{0.5}Co_{0.5}Fe_{0.5}O_3$ using XRD, SEM, TGA, and HT-XRD. Material shows reversible redox behavior when oxidized in air.
- Validated the modified bond valence method we developed (BVM_{oo}) as an accurate method for structure predictions and ground state polymorph identification.
- Identified 12 new materials to be experimentally tested at SNL and CU.
- Tested $Sr_{0.4}Gd_{0.6}Mn_{0.6}Al_{0.4}O_3$ and $Gd_{0.5}La_{0.5}Co_{0.5}Fe_{0.5}O_3$ in the laser heated stagnation flow reactor in collaboration with SNL.
- Validated our new scheme (SPuDS-DFT) to use BVM as a step between ML and DFT using the SPuDS program for high-throughput investigation of perovskite oxides; BVM accurately predicts perovskite oxide structures close to their DFT-relaxed structures in benchmarking dataset of 223 experimental perovskite oxides.
- SPuDS-DFT predicts ground state structures/energies tabulated in the MP within 50 meV/atom with essentially no computational cost.

- Pnma polymorph energy is most predictive of a composition's stability as a perovskite and is the ground state for ~90% of the perovskites in our dataset.
- Identification of the ground state is required to accurately predict electronic structure properties such as the band gap; although, our dataset suggests some general trends in terms of relative band gap size amongst the polymorphs, the DFT ground state is necessary to accurately describe E_g.
- Based on our results, we used Pnma for initial perovskite screening.
- Synthesis of five materials were attempted at CU via the modified Pechini method.
- Showed that magnetic sampling is necessary to correctly determine the relative stability and accurately predict the electronic structure properties of perovskite polymorphs.
- Demonstrated linear correlation between GII and DFT computed polymorph energies.
- Performed high-throughput calculations for 20,766 new compositions.
- Validated the use of Pnma (orthorhombic) polymorphs as a surrogate symmetry for the multinary perovskite space.
- Performed high-throughput oxygen vacancy formation energy calculations with magnetic sampling and distortions (symmetry off) for 312 Mn containing compounds.
- Identified 29 promising materials with large m^*_e and oxygen vacancies formation energies within the STCH active range.
- Independently identified newly discovered STCH active material Ca_2TiMnO_6 from our novel screening procedure and using detailed analysis to refine screening procedures.
- Identified a stability cutoff of ~200 meV/atom above the convex hull for experimentally observed ABO_3 compounds.
- Sent a total of 16 multinary manganate materials to Sandia (Coker and McDaniel) and our internal experimental collaborator (Weimer) to perform high-temperature XRD, and redox cycling to test their H_2 generation abilities.
- Tested hafnium containing perovskites in reactors at CU
- Synthesized, characterized and tested five new computationally discovered materials
- La_2MnNiO_6 showed promising results at CU and was sent to SNL for further testing
- Continued development of high-throughput materials screening scheme and its application to discovery of redox mediators for STCH.
- Published an article in collaboration with Sandia Node (McDaniel, Coker, Ambrosini) describing the novel STCH redox mediator $GdLaCoFeO_6$ (GLCF), which exhibits enhanced cyclability relative to known La-Co-Fe CO_2/CO redox mediators ($La_{0.6}Sr_{0.4}Co_{0.2}Fe_{0.8}O_3$ and $LaFe_{0.75}Co_{0.25}O_3$). https://doi.org/10.3389/fenrg.2021.750600
- Continued development of high-throughput materials screening scheme and its application to discovery of redox mediators for STCH.
- Submitted a manuscript reporting the high-throughput DFT investigation of gadolinium perovskites for solar thermo-chemical activity, which resulted in the discovery of 4 new STCH redox mediators, that were confirmed by the Sandia team led by McDaniel.
- Prepared a manuscript that reports the novel Gd-La-Mn-Ni-O (GLMN) perovskite and its STCH activity. Published a paper on the high-throughput DFT investigation of gadolinium perovskites for solar thermo-chemical activity that resulted in the discovery of 4 new

STCH redox mediators, which were confirmed by the Sandia team led by McDaniel. The computational framework reported in this publication is discussed below.

- Published a paper reporting the re-parameterization of bond valence parameters for perovskite oxides that predicts the relative DFT energetics of ABO_3 perovskite oxides. We anticipate that this re-parameterization enables the acceleration of high-throughput DFT investigations of ABO_3 and $AA'BB'O_6$ perovskite spaces.
- We published a collaborative paper[20] with the Sandia team led by McDaniel and our experimental collaborators at CU Boulder led by Weimer that reports the novel Gd-La-Mn-Ni-O (GLMN) perovskite and its experimental STCH activity, as well as the similar STCH activities of the La-Mn-Ni-O (L2MN) and Gd-Mn-Ni-O (G2MN) perovskites.
- We published a paper[17] that reports the large data set of perovskite oxides that we have evaluated using the bond valence method and density functional theory and which we are uploading to the MP Database.
- Gave a presentation at the 2022 *Spring ACS Meeting* on the investigation of gadolinium perovskites for solar thermo-chemical activity that resulted in the discovery of 4 new STCH redox mediators.[18]
- Prepared a collaborative manuscript with the Sutton lab at the University of South Carolina that featurizes perovskite structures for machine learning applications.
- Finalized and uploaded the computational dataset of 69,407 theoretical perovskite oxides, which serves as a source of data to be mined to identify novel compositions for STCH applications.
- Uploaded stable perovskites from this dataset to the Materials Project Database.
- Presented the dataset of theoretical perovskites at the annual COMBI Computational Materials conference in Golden, Colorado.
- Published a collaborative paper with the Sandia team co-led by McDaniel and CU Boulder experimental collaborator Weimer that explains the novel STCH activities of three new, mixed Mn/Ni perovskite oxides (La-Mn-Ni-O, Gd-La-Mn-Ni-O, and Gd-Mn-Ni-O systems).[20]
- 66,516 stable perovskites from the dataset have been uploaded to the Materials Project Database and an MPContribs landing page for this dataset has been created. https://contribs.materialsproject.org/projects/Multinary_Oxides.
- A computational manuscript that reports the stabilities of these 59,407 theoretical perovskite oxides and describes how to expand this dataset was prepared for submission.
- Our report on the DFT computed properties of 66,516 theoretical mixed metal oxides (59,407 perovskite oxides) has been published in *Nature Scientific Data*. The report includes a description of how to expand the dataset.[19]
- The complete dataset has been made publicly available on the MPContribs website at https://contribs.materialsproject.org/projects/Multinary_Oxides.
- We have used DFT to explore several different possible explanations for why Ga_2MnNiO_6 was found to be redox inactive at water splitting temperatures (by A. McDaniel) and determined that it is due to the extent of B-site cation disorder, which is influenced by the synthesis conditions and subsequent STCH cycling. A mixed computational/experimental publication that explains the STCH activities of mixed Mn/Ni perovskite oxides.

Publications and Presentations:

1. Bartel, C.J., S.L. Millican, A.M. Deml, J.R. Rumptz, W. Tumas, A.W. Weimer, S. Lany, V. Stevanovic, C. B. Musgrave, and A.M. Holder, "Machine Learning The Gibbs Energy of Inorganic Crystalline Solids," *Nature Communications*, 9 (2018). DOI: 10.1038/s41467-018-06682-4
2. Bartel, C., J. Rumptz, A. Holder, A. Weimer and C. Musgrave, "High-throughput Equilibrium Analysis of Active Materials for Solar Thermochemical Ammonia Synthesis," *ACS Applied Materials and Interfaces*, 11 (28) 24850-24858 (2019). DOI: 10.1021/acsami.9b01242.
3. Invention Disclosure, 02/01/2019: This invention centers on a newly identified class of all-inorganic halide double perovskites with the general formula $Cs_2BB'Cl_6$ that exhibit promising and tunable optoelectronic properties. Leveraging a statistically learned tolerance factor to screen 903 possible compositions, we identified 311 cesium chloride double perovskites likely to form stable perovskite phases. From these, 261 were predicted to be synthesizable, and 47 were identified as non-toxic compounds with direct or nearly direct band gaps (1–3 eV), ideal for optoelectronic applications. A subclass of these materials, triple-alkali perovskites ($Cs_2[Alk^+][TM^{3+}]Cl_6$), emerged as especially promising, displaying large and tunable exciton binding energies and absorption features highly sensitive to transition metal identity. These materials combine Cl-based alkali and transition-metal sublattices, producing unique electronic structures and long-lived excitonic states that make them suitable for use in light emission, sensing, spintronics, and quantum information applications. The discovery demonstrates a new strategy for realizing optoelectronic materials by exploiting sublattice mixing in double perovskites.
4. Bartel, C., V. Stevanovic, C. Musgrave, A. Holder, "The role of decomposition reactions in assessing first-principles predictions of solid stability," *npj Computational Materials,* 5 (1), 4 (2019). DOI: 10.1038/s41524-018-0143-2
5. Bartel, C.J., C. Sutton, B.R. Goldsmith, R. Ouyang, C.B. Musgrave, L.M. Ghiringhelli, M. Scheffler, "New Tolerance Factor to Predict Perovskite Oxide and Halide Stability," *Science Advances,* 5 (2) eaav0693 (2019). DOI: 10.1126.aav0693
6. Millican, S., I. Androshchuk, R. Trottier, H. Idriss, C.B. Musgrave, and A.W. Weimer, "Oxidation Kinetics of Hercynite Alloys for Solar Thermochemical Fuel Production," *Solar Energy*, 401, 126015 (2020). DOI: 10.1016/j.cej.2020.126015
7. Invention Disclosure, 02/26/2020: This invention describes a high-throughput, thermodynamic screening methodology for discovering and evaluating active materials for chemical looping (CL) processes. The approach leverages a machine-learned Gibbs free energy descriptor, G(T), to predict temperature-dependent formation energies of solid materials, enabling rapid assessment of redox pairs for use in CL systems. The method was validated against known CL combustion (CLC) materials and applied to identify over 1300 previously unstudied redox pairs that are thermodynamically viable for high-yield combustion of methane. Furthermore, the methodology was extended to propose and evaluate a novel chemical looping process for sulfur dioxide (SO_2) production from raw sulfur and air. This new process offers a more energy-efficient and lower-emission alternative to conventional SO_2 generation, with 12 sulfate/sulfide redox pairs identified as viable candidates. Some of these, such as $CuSO_4$/CuS and $NiSO_4$/NiS, were corroborated by existing experimental data. The invention provides a robust, scalable framework for accelerating the discovery and

deployment of materials for diverse CL technologies, with implications for energy efficiency, emission reductions, and sustainable chemical manufacturing

8. Trottier, R., S. Miller, A. Holder and C. Musgrave, "DFT Study of Oxygen Vacancy Diffusion in the Iron Aluminate Spinel Hercynite," *ACS Applied Materials & Interfaces*, 12 (21) 23831-23843 (2020). DOI: 10.1021/acsami.0c02819
9. Singstock, N., C. Bartel, A. Holder, and C. Musgrave, "Accelerated Discovery of Redox Mediating Materials for the Efficient Production of Sulfuric Acid by Chemical Looping," *Advanced Energy Materials*, 2000685 (2020). DOI: 10.1002/aenm.202000685
10. Trottier, R., S. Millican, C. and Musgrave, "Modified Single Iteration Synchronous-Transit Approach to Bound Diffusion Barriers for Solid-State Reactions," *Journal of Chemical Theory and Computation*, 16, 5912 (2020). DOI: 10.1021/acs.jctc.0c00552
11. Clary, J., A. M. Holder and C. B. Musgrave, "Computationally Predicted High-Throughput Free-Energy Phase Diagrams for the Discovery of Solid-State Hydrogen Storage Reactions," *Chemistry of Materials*, 12, 48553 (2020). DOI: 10.1021/acsami.0c13298
12. Millican, S., A. Deml, M. Papac, R. O'Hayre, A. Holder, C. Musgrave and V. Stevanovic, "Predicting Oxygen Off-Stoichiometry and Hydrogen Incorporation in Complex Perovskite Oxides," *Chemistry of Materials*, 34 (2) 510-518 (2022). DOI: 10.1021/acs.chemmater.0c04765
13. Millican, S., J. Clary, A. Holder, C. Musgrave, S. Lany, "Redox Defect Thermochemistry of $FeAl_2O_4$ Hercynite in Water-splitting from First Principles Methods," *Chemistry of Materials*, 34 (2) 519-528 (2022). DOI: 10.1021/acs.chemmater.1c01049
14. S. Millican, I. Androschuk, J. Tran, R. Trottier, A. Bayon, Y. Al-Salik, H. Idriss, C. Musgrave, A. Weimer, "Oxidation Kinetics of Hercynite Alloys for Solar Thermochemical Fuel Production" *American Institute of Chemical Engineers*. November 2020.
15. Park, J. E., Bare, Z. B., Morelock, R. J., Rodriguez, M. A., Ambrosini, A., Musgrave, C. B., McDaniel, A. H., and Coker, E. N. "Computationally Accelerated Discovery and Experimental Demonstration of $Gd_{0.5}La_{0.5}Co_{0.5}Fe_{0.5}O_3$ for Solar Thermochemical Hydrogen Production," *Frontiers in Energy Research*, (2021). DOI: 10.33 89/fenrg.2021.750600
16. Bare, Z., R. Morelock, C. Sutton, C. Musgrave, "Structural and Stability Trends in Single (ABO_3) Perovskite Oxides from DFT-Optimized Bond Valence Structures," *American Chemical Society National Meeting*, Boston, MA, August 2021.
17. Bare, Z., R. Morelock, C. Sutton, C. Musgrave, "Structural and Stability Trends in Single (ABO_3) Perovskite Oxides from DFT-Optimized Bond Valence Structures," *American Institute of Chemical Engineers Annual Meeting*, Boston, MA, November 2021.
18. Bare, Z.J.L, R. Morelock, C.B. Musgrave, "A Computational Framework to Accelerate the Discovery of Perovskites for Solar Thermochemical Hydrogen Production; Identification of Gd Perovskite Oxide Redox Mediators," *Advanced Functional Materials*, (2022). DOI: 10.1002/adfm.202200201
19. Morelock, R., Z. J. L. Bare and C. B. Musgrave, "Bond-Valence Parameterization for the Accurate Description of DFT Energetics in ABO_3 Perovskite Oxides," *Journal of Chemical Theory and Computation*, (2022). DOI: 10.1021/acs.jctc.1c01113
20. Morelock, R., Z. J. L. Bare and C. B. Musgrave, "Computational Identification of Gd Perovskite Oxide Redox Mediators," *American Chemical Society*, San Diego, CA, March 2022.

21. Bare, Z. J. L., R. J. Morelock, and C. Musgrave, "Dataset of theoretical multinary perovskite oxides," *Sci Data,* 10, 244 (2023). https://doi.org/10.1038/s41597-023-02127-w
22. Morelock, R.J., J. Tran, Z. J. L. Bare, J. A. Trindell, A. H. McDaniel, A. W. Weimer, and C. B. Musgrave, "Computationally Guided Discovery of Mixed Mn/Ni Perovskites for Solar Thermochemical Hydrogen Production at High H_2 Conversion," *Chemistry of Materials*, 36 (11) 5331 (2024). DOI: 10.1021/acs.chemmater.3c02807
23. Yew, S., R. J. Morelock, and C. B. Musgrave, "Orthorhombic Structures as Inorganic Halide Perovskite Models for High-Throughput DFT Investigations," J. *Phys. Chem. C*, 129, 4010 (2025). https://doi.org/10.1021/acs.jpcc.4c08125